Summer 8-12-2011

Lipid and Protein Sorting by, and Generation of, Membrane Curvature in Model Systems

Michael C. Heinrich

University of Pennsylvania, heinric@sas.upenn.edu

Lipid and Protein Sorting by, and Generation of, Membrane Curvature in Model Systems

Abstract

The potential physiological relevance of liquid-liquid phase separation in lipid membranes to the formation and stability of "lipid rafts" in cellular plasma membranes has prompted extensive investigation of the physical chemistry underlying these phenomena. Furthermore, the concept of lipid rafts – 10-200 nm regions of cellular membrane enriched in specific lipids and proteins to enable complex processes – has led naturally to questions concerning the sorting of both lipids and proteins between membranes of different organelles within the cell, each with distinct lipid and protein composition. The shapes and, more specifically, the curvatures of membrane transport intermediates have been invoked to play a role in both lipid and protein sorting. In addition, lipid and protein composition may directly affect the membrane curvature. In this contribution, the line tension and dipole density differences between demixed fluid phases of monolayers comprised of dimyristoylphosphatidylcholine and dihydrocholesterol were investigated by measuring the two-dimensional thermal fluctuations of domain boundaries. These parameters are essential determinants of domain stability, and their quantification will yield an increased understanding of the physical processes responsible for aspects of lateral phase separation. Furthermore, phase-separated giant unilamellar vesicles from which are pulled thin cylindrical tubes are employed to understand domain nucleation in curvature gradients, complemented by measurements of the biophysical force required to pull such tubes. These results indicate that strong lipid-lipid interactions can lead to lipid sorting by curvature, as well as present diffusion barriers to enable selective sorting of lipids and proteins. Finally, the curvature generation of *Drosophila* amphiphysin N-BAR domain is quantitatively assessed through the tube-pulling assay as before but performed using homogenous lipid membranes. Fluorescently-labeled protein preferentially sorted into the high (positive) curvature of the tubes from the essentially flat vesicle. Furthermore, the measured tube force decreased to lower equilibrium values in a protein concentration-dependent manner. Future measurements on other BAR domains will improve upon previous qualitative comparisons of curvature generation ability. Collectively, the results provide quantitative assessment of several biophysical parameters underlying the lateral sorting of lipids and proteins.

Subject Categories
Biological and Chemical Physics | Physical Chemistry

LIPID AND PROTEIN SORTING BY, AND GENERATION OF, MEMBRANE CURVATURE IN MODEL SYSTEMS

Michael C. Heinrich

A DISSERTATION

in

CHEMISTRY

Presented to the Faculties of the University of Pennsylvania

in

Partial fulfillment of the requirements for the

Degree of Doctor of Philosophy

2011

_____

Professor Tobias Baumgart
Supervisor of Dissertation

_____

Professor Gary Molander
Graduate Group Chair

Committee Members:

Dr. Feng Gai, Professor of Chemistry
Dr. Jeffery Saven, Associate Professor of Chemistry
Dr. Ivan Dmochowski, Associate Professor of Chemistry

Dedication

To Laura, who was with me every step of the way.

Acknowledgement

This thesis was only possible with the help of many others. First, I thank my advisor Professor Tobias Baumgart, who has supported me these past four years. Joining a new research group allowed me to work on a wide range of topics and learn new chemical, physical, biological, engineering, and programming techniques, and I am a more capable scientist because of it. I am constantly in awe of his work ethic and the depth and breadth of his knowledge, and he has had the most profound effect on my career path. I appreciate his demand for solid results, whose advice reflected my previous mentor's not to fool others, and perhaps more importantly, not to fool oneself. I am grateful for his positive outlook and apparently unwavering belief that most anything could be solved, without which the many (many) failures I experienced would have precluded this thesis.

Furthermore, I am indebted to Professors Feng Gai, Jeffery Saven, and Ivan Dmochowski, who, as members of my committee, challenged me to substantiate and evaluate my work such that it would stand up to scrutiny. I thank them for both their time and guidance.

This thesis contains the results of collaborative work with many others. Aiwei Tian and Cinzia Esposito were instrumental in teaching me to work with GUVs. Ilya Levental trained me on the monolayer system, resulting in my first success as a graduate student. Ben Capraro has improved my biochemistry knowledge and worked with me on the amphiphysin protein project. Chih-Jung Hsu was my partner in crime; I thank him for not complaining when I monopolized our microscope. I also wish to thank the other members of the Baumgart lab, including fellow graduate students Wan-Ting Hsieh, Chen Zhu, and Tingting Wu. All were good-humored colleagues who were unfailingly generous with their time and help; I am fortunate to have worked with such a group.

Finally, my thanks go out to my parents who supported me and enabled me to get an education, my brothers who have taught me to work hard and to laugh all the while, and to Laura, who scoffed at my self-doubt.

ABSTRACT

LIPID AND PROTEIN SORTING BY, AND GENERATION OF, MEMBRANE

CURVATURE IN MODEL SYSTEMS

Michael C. Heinrich

Dr. Tobias Baumgart

The potential physiological relevance of liquid-liquid phase separation in lipid membranes to the formation and stability of "lipid rafts" in cellular plasma membranes has prompted extensive investigation of the physical chemistry underlying these phenomena. Furthermore, the concept of lipid rafts – 10-200 nm regions of cellular membrane enriched in specific lipids and proteins to enable complex processes – has led naturally to questions concerning the sorting of both lipids and proteins between membranes of different organelles within the cell, each with distinct lipid and protein composition. The shapes and, more specifically, the curvatures of membrane transport intermediates have been invoked to play a role in both lipid and protein sorting. In addition, lipid and protein composition may directly affect the membrane curvature. In this contribution, the line tension and dipole density differences between demixed fluid phases of monolayers comprised of dimyristoylphosphatidylcholine and dihydrocholesterol were investigated by measuring the two-dimensional thermal fluctuations of domain boundaries. These parameters are essential determinants of domain stability, and their quantification will yield an increased understanding of the physical processes responsible for aspects of lateral phase separation. Furthermore, phase-separated giant unilamellar vesicles from which are pulled thin cylindrical tubes

are employed to understand domain nucleation in curvature gradients, complemented by measurements of the biophysical force required to pull such tubes. These results indicate that strong lipid-lipid interactions can lead to lipid sorting by curvature, as well as present diffusion barriers to enable selective sorting of lipids and proteins. Finally, the curvature generation of *Drosophila* amphiphysin N-BAR domain is quantitatively assessed through the tube-pulling assay as before but performed using homogenous lipid membranes. Fluorescently-labeled protein preferentially sorted into the high (positive) curvature of the tubes from the essentially flat vesicle. Furthermore, the measured tube force decreased to lower equilibrium values in a protein concentration-dependent manner. Future measurements on other BAR domains will improve upon previous qualitative comparisons of curvature generation ability. Collectively, the results provide quantitative assessment of several biophysical parameters underlying the lateral sorting of lipids and proteins.

Table of Contents

List of Tables

List of Figures

Chapter 1: Introduction

Critical Phase Separation in Lipid Monolayers[a]

In recent years, lateral compositional heterogeneities in lipid membranes have received significant interest because of speculation about their involvement in signaling and trafficking complexes in cellular membranes. In particular, the "membrane/lipid raft" hypothesis[1] (see below) has stimulated in-depth studies of liquid-liquid phase separation in multicomponent lipid membranes. Microscopically visible phase separation has been demonstrated in both mixed bilayer[2-5] and monolayer systems[6-7], and the equilibrium physical chemistry of phase separation in both bilayers[8] and monolayers[9-10] has been investigated extensively. Fluid phase coexistence in lipid bilayer membranes is characterized by the formation of a liquid ordered (Lo) phase, associated with a higher degree of lateral ordering/packing than the liquid disordered (Lα or Ld) phase observed in pure phospholipid membranes and was first demonstrated by Dietrich et al.[2] and Samsonov et al[3]. Fluid phase coexistence in lipid monolayers was first observed by Subramaniam et al[11].

Much effort has been dedicated to the characterization of transitions from two observable immiscible phases to a single homogeneous phase. These mixing/demixing transitions have been shown to be functions of lipid composition[12], temperature[13-15], surface pressure[11, 16], and degree of cross-linking[17], while compositional fluctuations on length scales below optical resolution are also beginning to be addressed[18-22]. Recent observation of qualitatively similar liquid-liquid phase

1

separation in plasma membrane-derived giant vesicles (GPMVs) has further underlined the potential biological relevance of these model membrane findings(*23*).

Of particular interest is the question of how domain size is regulated(*24*). In lipid bilayer membranes, the only known driving force for domain coarsening is line tension at the phase boundary. Line tension is the interfacial energy per unit length that arises at the boundary of two immiscible phases, and is the one-dimensional analogue of surface tension. Its magnitude depends on the dissimilarity of the two phases, and naturally decreases to zero as the critical point of the phase transition boundary is approached. Quantification of this parameter is helpful not only for understanding domain coarsening kinetics and thermodynamics, but also to elucidate three-dimensional modulation of membrane shape, both in model membranes(*13, 25-26*) and possibly extended to biologically relevant membrane shape transitions related to membrane trafficking(*27*). Additionally, variation of the interfacial line tension by membrane minority components would suggest line active species that function as domain stabilizers or disruptors in model systems, and possibly as "lipid raft" regulators in plasma membranes of living cells.

Line tension at liquid domain boundaries has previously been examined both theoretically and experimentally in monolayers(*28-31*) and in bilayers(*13, 26, 32-33*). Esposito et al. recently obtained extremely small line tensions in lipid bilayer domains (with fluctuating boundaries) of giant unilamellar vesicles (GUVs)(*32*). Giant vesicles, typically in the size range of a few dozen micrometers in diameter, pose challenges to the accurate analysis of experimental domain undulations due to the spherical geometry that is imaged in the planar focal plane(*32*). Lipid monolayers, however, are not limited

in lateral dimensions, and their optically flat surface is advantageous for extended flicker spectroscopy studies. In monolayers of 30% cholesterol and 70% dimyristoylphosphatidylcholine (DMPC), line tension was estimated by Benvegnu and McConnell through the relaxation rate following mechanical deformation of bola-shaped domains to the energy minimizing circular domain shape(*28*) (also see Refs(*34-36*)). This study demonstrated monolayer domain line tension varied by 2 orders of magnitude (from ~0.1 pN to more than 10 pN) depending on the monolayer surface pressure. A potential limitation of this early work was the need for several secondary parameters and simplifying assumptions in order to analyze the experimental data to yield line tensions(*28*). In particular, the dipole density difference between coexisting phases could only be determined in experiments separate from line tension studies via measurements of the diffusional mobility of electrostatically trapped domains(*37*), or through field gradient electrophoresis(*38*). The small line tension regime (found near the phase transition boundary, e.g. at high monolayer surface pressures) is of greater biological relevance, as recent results with GPMVs suggest that membranes of living cells are maintained near a similar critical phase transition boundary(*39*). In this regime, however, the dipole density difference plays a more substantial role in reducing the effective line tension measured in earlier monolayer studies(*28*); it is therefore imperative that both parameters be characterized simultaneously to enable accurate determination of the biologically important line tension.

Fourier power spectra of thermal domain boundary fluctuations, readily observable at relatively small line tension, had first been published by Seul and Sammon(*40*). Goldstein and Jackson (GJ) then adapted a theory previously

developed for magnetic films with phase coexistence(*41*) to the ultrathin film limit of lipid monolayers with dipolar interactions(*29*). The GJ theory relates the competing effects of interfacial line tension and dipolar repulsion to thermal domain boundary in-plane undulations and allowed analysis of the data of Ref (*40*) to yield line tension γ and dipolar density difference μ close to the critical pressure, though only for a single pressure and composition(*29*). Stottrup et al. recently extended these early measurements(*31*); their analysis, however, neglected the potentially important dipolar interaction which can modulate the power spectra of domain edge fluctuations. Esposito et al. recently experimentally demonstrated that, in fluctuating lipid bilayer domains, dipolar contributions to the fluctuation spectra are not discernible, as expected from the screening effect due to the existence of an additional aqueous half-space(*32*). However, the data presented in Chapter 4(*42*), in combination with the GJ analysis, not only show that, in monolayers, dipolar interactions significantly modify fluctuation spectra, but also demonstrate that dipolar interactions can be accurately quantified by flicker spectroscopy.

In Chapter 4, these findings are extended by applying the GJ theory to the analysis of a large data set of time-lapse images of demixed monolayers to accurately quantify both the line tension and the dipole density difference between the two coexisting liquid phases as a function of surface pressure without external perturbation. Using this approach, we find excellent agreement with published values for γ and μ for the critical composition of 30% DChol and 70% DMPC; we also determine these parameters in mixtures with 35% and 40% DChol. We furthermore obtain critical exponents for γ and μ as the surface pressure approaches the critical pressure (where phase coexistence disappears) and again find good agreement with predicted values.

To our knowledge, this is the first concurrent quantification of both the line tension and dipole density differences in coexisting fluid phases in lipid monolayers as a function of surface pressure.

In addition, preliminary results are presented and discussed (Chapter 4) on the topic of line-active components (so-called "linactants"(*43*)), the one-dimensional analogue of a surfactant. Such a molecular species is posited to be preferentially sorted to the interface of a phase boundary, thereby reducing the line tension(*43-44*). Importantly, this reduction might occur despite a minority presence (by mol fraction) of the linactant in the lipid system, as the number of molecules present at the boundaries of micron-sized (or larger) domains is also a small percentage of the total lipid monolayer. In a binary monolayer composed of hydrocarbon-rich and fluorocarbon-rich phases, a minority addition of a partially-fluorinated hydrocarbon molecule reduced the line tension, and a single-tailed variant was found to be more effective than the double-tailed molecule, reducing line tension 20% at a mol fraction of 0.08%(*43*). In Chapter 4, results are presented on measurements of line tension in phase-separated monolayers (at the critical composition, 30% DChol and 70% DMPC) following the inclusion of 0.1% of the single-tailed lysoPC (1-myristoyl-2-hydroxy-*sn*-glycero-3-phosphocholine). Significant reductions in line tension are observed over a range of surface pressures below the transition pressure.

Lipid Sorting in Phase Separated Bilayers[b]

Phase separation into liquid ordered (Lo) and liquid disordered (Ld) domains in lipid bilayer membranes has received wide-spread interest, in part due to the lipid raft (also termed membrane raft) hypothesis put forward by Simons and Ikonen(*1*) who suggested that cellular membranes might not only act as a solvent for membrane proteins, but also could dynamically segregate their constituent lipids into "rafts" (or domains). These domains could then act as transiently-stable platforms, bringing together the protein machinery necessary for signal transduction across the membrane(*45-46*). Furthermore, they could be involved in the formation of transport intermediates, thereby enabling selective sorting of lipids and proteins to achieve the steady-state heterogeneity of the multitude of membranes within a single cell. Lipid rafts are defined by their enrichment in sterols and sphingolipids, which serves as the basis for the expectation that they are physically similar (in terms of lipid diffusion, bending stiffness, etc) to the micron-scale Lo phases observed in model systems(*47*). Though the existence of lipid rafts is still controversial due to a small size and short lifetime (thus frustrating simple methods of observation; note that caveolae and other microstructures represent a special case of lipid and protein heterogeneity that is readily visualized(*48*)), a large body of evidence has accumulated implicating their presence in cells (see (*49-50*)). Importantly, this includes the observation that giant plasma membrane vesicles (GPMVs), which were derived from chemically-induced "blebbing" of intact cells, will phase separate into two liquid phases in a temperature-dependent manner despite the significant complexity in

---

[b] Parts of this chapter are reproduced from previously published work: Heinrich, M. C., Tian, A., Esposito, C., and Baumgart, T. (2010) Dynamic sorting of lipids and proteins in membrane tubes with a moving phase boundary, *Proc. Natl. Acad. Sci. U.S.A. 107*, 7208.

6

both lipid and membrane protein composition(*23*), apparently mirroring the phase separation observed in bilayers with simpler composition(*15*).

Giant unilamellar vesicles (GUVs) of ternary (and higher) compositions have been used as model systems for cellular membranes because they readily separate into Lo and Ld phases that are large enough to be studied with a range of fluorescence microscopy techniques, and are furthermore amenable to biophysical manipulation of their mechanical properties (namely membrane tension, bending stiffness, and size/shape). In addition to the line tension arising at the interface between coexisting domains (described above and in Chapter 4), the Lo and Ld phases are distinguished by a smaller resistance towards bending in the latter(*25, 51-52*). This bending stiffness difference is made manifest when both phases are present in a curvature gradient: the Lo phase partitions preferentially into flatter regions(*13, 51, 53*). This connection between membrane composition and shape observed in model systems is a likely sorting principle in cellular membranes(*1, 54*).

To investigate the coupling of lipid and protein sorting to membrane curvature, one approach has been to utilize a pipette-aspirated GUV from which can be pulled a cylindrical tube with tunable diameters on the order of 10-100nm (see Chapter 3)(*55*). This enables a thermodynamically equilibrated system connecting regions of high and low (relative to the molecular scale) curvature in which the sorting of membrane components can be investigated. The weak segregation limit, in which membranes do not exhibit sharp phase coexistence boundaries but instead display composition gradients that depend on the underlying curvature, have been investigated previously(*56-57*). This nonideal mixing required global compositions which were close to the critical point

composition; tubes pulled from vesicles with composition far from a phase boundary were not observed to induce lipid sorting on the basis of lipid shape(*58*). In Chapter 5, the strong segregation limit – in which vesicles have clearly resolved microscopic phase boundaries – is examined for its potential to actively sort lipids and protein by curvature: Most model membrane curvature research involving lipid and lipid/protein mixtures has focused on thermodynamic equilibrium conditions(*56-58*). However, since the situation in biological cells is one of steady state and regulated mass transport with continuous recycling of membrane components, Chapter 5 presents results on the dynamic aspects of membrane sorting(*59*). Furthermore, lipid sorting is achieved exclusively through the controlled membrane curvature, in contrast to previous studies that have induced phase separation via photoactivation(*51, 60*) to exploit the sensitivity of membrane phase behavior to fluorophore-mediated lipid breakdown(*51*).

Analysis of intracellular cargo movement has demonstrated that many transport carriers consist of tubes rather than vesicles(*61-62*). Furthermore, parts of several cellular organelles, including the endoplasmic reticulum, the trans-Golgi network, and various endosomal compartments consist of tubular networks(*62*). Numerous mechanisms are known that lead to tube formation *in vivo*. These include exertion of pulling forces by molecular motors, membrane/cytoskeletal interactions, and the action of curvature-generating peripherally binding and transmembrane proteins. Clearly, lipid sorting during the formation of such high-curvature transport carriers could partly explain how lipid heterogeneity between different organelle membranes is maintained. A recent paper from Bassereau has noted that retrograde transport (from the Golgi to the endoplasmic reticulum (ER)) could be facilitated by such sorting, where minimal transport of

8

sphingomeyelin and cholesterol would aid in keeping those lipid levels low in the ER(*63*). The same work noted, however, that the anterograde pathway should require higher levels of these (membrane-raft enriched) lipids, and that protein-lipid interactions might account for their enrichment in transport carriers. In Chapter 5, we present evidence of a similar (but role-reversed) situation, where lipid sorting in the form of domain formation generates a diffusion barrier that acts to confine a low-curvature preferring protein (Cholera toxin) on a high-curvature tube.

Protein Sorting and Curvature Generation in Lipid Bilayers[c]

Aspects of lipid membrane curvature regulation have recently emerged as a forefront in physical chemistry(*64-66*). The importance of membrane curvature is underscored by the fact that cellular organelles demonstrate a large variety of membrane shapes. Local curvatures range from essentially flat regions of the plasma membrane to highly bent spherical transport vesicles and tubular transport intermediates with cylindrical curvature. Importantly, the local curvature of a single continuous membrane can vary over all of this range, as in the case of the network of transverse (T-) tubules found in cardiac and skeletal muscle cells. T-tubules are invaginations of the plasma membrane surrounding muscle fiber units that, along with the sarcoplasmic reticulum, allow for the control of coordinated force generation by the muscle(*67*). In *Drosophila*, the peripheral membrane-binding protein amphiphysin is known to localize on T-tubules, playing a critical role in enabling the excitation-contraction coupling they perform: null mutations in the *Drosophila* amphiphysin gene have been shown to result in viable but

flightless flies(*68-70*). Importantly, these studies distinguished the role played by the single form of amphiphysin in non-vertebrates from the two known mammalian forms: amphiphysin I, which aids in endocytosis(*71*), and amphiphysin II, which also localizes on T-tubules(*72*).

All identified isoforms of amphiphysin contain a highly conserved Bin/Amphiphysin/Rvs (BAR) domain. Crystal structures obtained for BAR domain dimers exhibit a characteristic banana-shaped form along their charged membrane-binding surfaces(*73-74*), in agreement with MD simulations. This structure motivated use of the scaffolding mechanism, whereby a zero spontaneous curvature membrane adopts the locally bent shape of the curvature-generating protein(*73, 75*), to explain the tubulation of liposomes incubated with amphiphysin(*76-77*). Support for the scaffolding mechanism originally came from the observation that BAR domains with smaller curvatures (such as F-BAR) tended to produce wider tubules(*78*). Importantly, these tubules were reported to have curvatures similar to those of the BAR domains used, which implies that the membrane bending energy is smaller than that required to deform the dimer or to orient the concave lipid-binding surface away from the membrane. The ability of such a protein to effectively act as a scaffold depends vitally on the interaction strength with the underlying membrane, which for a single unit is on the order of or lower than the corresponding bending energy(*79*). Therefore, effective scaffolding likely requires cooperativity among adjacent BAR proteins, where the sum interaction energy may dominate. Such a lattice network of domains was observed through cryo-electron microscopy reconstructions that indicated lateral and tip-to-tip interactions between neighboring dimers(*80*). Various types of lattice arrangements (with differing

10

degrees of membrane-bending ability) for N-BAR domains have been explored through all-atom and coarse-grained simulations(*76, 81*).

Mutational studies have also been performed to elucidate the bending mechanism of amphiphysin, which contains an N-terminal amphipathic helix that is thought to aid in curvature generation via asymmetric insertion into the bilayer(*73, 82-83*). Deletion of the helix H0 was found to reduce but not eliminate the resulting tubulating ability(*73*). In agreement are recent simulations which predicted that, while both the N-BAR and BAR domains could lead to membrane bending, the H0 helix alone would not(*84*). This last prediction was in disagreement with recent theoretical work on the curvature generation efficiency by asymmetric leaflet insertion at the densities relevant to the H0 density for an amphiphysin lattice(*85*). Still, the insertion mechanism is recognized as a viable mechanism to achieve membrane bending and likely contributes to the action of the N-BAR domain(*86*).

Chapter 6 reports efforts to quantify the ability of the N-BAR domain to stabilize curved membrane tubules(*87*). Giant unilamellar vesicles (GUVs) were incubated with Drosophila amphiphysin N-BAR domains (DA-N-BAR) and pipet-aspirated to control membrane tension(*55*). A tube could then be pulled with an optical trap(*59, 88*) to enable measurements of the force necessary to pull and then maintain a tube at equilibrium. For single-component lipid vesicles, it is well-established(*89*) that the tube force is related to vesicle membrane tension and bending stiffness (see also Chapter 3). Molecules that act as curvature generators effectively lower the membrane bending energy(*57, 90*). Tube bending energy can also be lowered in the case of lipid sorting both near(*56, 91*) and inside of(*59*) a critical demixing boundary; the lipid compositions used here do not

reflect such conditions. An effective spontaneous curvature may then be observed through measurements of the static (equilibrium) tube force needed to maintain the protein-bound tube at fixed length.

References

1. Simons, K., and Ikonen, E. (1997) Functional rafts in cell membranes, *Nature 387*, 569.
2. Dietrich, C., Bagatolli, L. A., Volovyk, Z. N., Thompson, N. L., Levi, M., Jacobson, K., and Gratton, E. (2001) Lipid rafts reconstituted in model membranes, *Biophys. J. 80*, 1417.
3. Samsonov, A. V., Mihalyov, I., and Cohen, F. S. (2001) Characterization of cholesterol-sphingomyelin domains and their dynamics in bilayer membranes, *Biophys. J. 81*, 1486.
4. Korlach, J., Schwille, P., Webb, W. W., and Feigenson, G. W. (1999) Characterization of lipid bilayer phases by confocal microscopy and fluorescence correlation spectroscopy, *Proc. Natl. Acad. Sci. U.S.A. 96*, 8461.
5. Bagatolli, L. A., and Gratton, E. (2000) Two photon fluorescence microscopy of coexisting lipid domains in giant unilamellar vesicles of binary phospholipid mixtures, *Biophys. J. 78*, 290.
6. Von Tscharner, V., and McConnell, H. M. (1981) An alternative view of phospholipid phase behavior at the air-water interface, *Biophys. J. 36*, 409.
7. Losche, M., Sackmann, E., and Mohwald, H. (1983) A fluorescence microscopic study concerning the phase-diagram of phospholipids, *Phys. Chem. Chem. Phys. 87*, 848.
8. Veatch, S. L., and Keller, S. L. (2005) Seeing spots: complex phase behavior in simple membranes, *Biochim. Biophys. Acta. 1746*, 172.
9. McConnell, H. M. (1991) Structures and transitions in lipid monolayers at the air-water interface, *Annu. Rev. Phys. Chem 42*, 171.
10. Okonogi, T. M., and McConnell, H. M. (2004) Contrast inversion in the epifluorescence of cholesterol-phospholipid monolayers, *Biophys. J. 86*, 880.
11. Subramaniam, S., and McConnell, H. M. (1987) Critical mixing in monolayer mixtures of phospholipid and cholesterol, *J. Phys. Chem. 91*, 1715.
12. Keller, S. L., Anderson, T. G., and McConnell, H. M. (2000) Miscibility critical pressures in monolayers of ternary lipid mixtures, *Biophys. J. 79*, 2033.
13. Baumgart, T., Hess, S. T., and Webb, W. W. (2003) Imaging coexisting fluid domains in biomembrane models coupling curvature and line tension, *Nature 425*, 821.
14. Veatch, S. L., and Keller, S. L. (2002) Organization in lipid membranes containing cholesterol, *Phys. Rev. Lett. 89*, 268101.
15. Veatch, S. L., and Keller, S. L. (2003) Separation of liquid phases in giant vesicles of ternary mixtures of phospholipids and cholesterol, *Biophys. J.*

85, 3074.

16. Hirshfeld, C. L., and Seul, M. J. (1990) Critical mixing in monomolecular films: pressure-composition phase-diagram of a 2-dimensional binary mixture, *J. Phys. 51*, 1537.

17. Hammond, A. T., Heberle, F. A., Baumgart, T., Holowka, D., Baird, B., and Feigenson, G. W. (2005) Crosslinking a lipid raft component triggers liquid ordered-liquid disordered phase separation in model plasma membranes, *Proc. Natl. Acad. Sci. U.S.A. 102*, 6320.

18. Veatch, S. L., Soubias, O., Keller, S. L., and Gawrisch, K. (2007) Critical fluctuations in domain-forming lipid mixtures, *Proc. Natl. Acad. Sci. U.S.A. 104*, 17650.

19. Heberle, F. A., Buboltz, J. T., Stringer, D., and Feigenson, G. W. (2005) Fluorescence methods to detect phase boundaries in lipid bilayer mixtures, *Biochim. Biophys. Acta. - Molec. Cell Res. 1746*, 186.

20. Silvius, J. R. (2003) Fluorescence energy transfer reveals microdomain formation at physiological temperatures in lipid mixtures modeling the outer leaflet of the plasma membrane, *Biophys. J. 85*, 1034.

21. Nielsen, L. K., Bjornholm, T., and Mouritsen, O. G. (2000) Critical phenomena - fluctuations caught in the act, *Nature 404*, 352.

22. Radhakrishnan, A., and McConnell, H. M. (2007) Composition fluctuations, chemical exchange, and nuclear relaxation in membranes containing cholesterol, *J. Phys. Chem. 126*, 185101.

23. Baumgart, T., Hammond, A. T., Sengupta, P., Hess, S. T., Holowka, D., Baird, B., and Webb, W. W. (2007) Large-scale fluid/fluid phase separation of proteins and lipids in giant plasma membrane vesicles, *Proc. Natl. Acad. Sci. U.S.A. 104*, 3165.

24. Frolov, V. A. J., Chizmadzhev, Y. A., Cohen, F. S., and Zimmerberg, J. (2006) "Entropic traps" in the kinetics of phase separation in multicomponent membranes stabilize nanodomains, *Biophys. J. 91*, 189.

25. Baumgart, T., Das, S., Webb, W. W., and Jenkins, J. T. (2005) Membrane elasticity in giant vesicles with fluid phase coexistence, *Biophys. J. 89*, 1067.

26. Tian, A., Johnson, C., Wang, W., and Baumgart, T. (2007) Line Tension at Fluid Membrane Domain Boundaries Measured by Micropipette Aspiration, *Phys. Rev. Lett. 98*, 208102.

27. Liu, J., Kaksonen, M., Druvin, D. G., and Oster, G. (2006) Endocytic vesicle scission by lipid phase boundary forces, *Proc. Natl. Acad. Sci. U.S.A. 103*, 10277.

28. Benvegnu, D. J., and McConnell, H. M. (1992) Line tension between liquid domains in lipid monolayers, *J. Phys. Chem. 96*, 6820.

29. Goldstein, R. E., and Jackson, D. P. (1994) Domain shape relaxation and the spectrum of thermal fluctuations in Langmuir monolayers, *J. Phys. Chem. 98*, 9626.

30. Wurlitzer, S., Steffen, P., and Fischer, T. M. (2000) Line tension of Langmuir monolayer phase boundaries determined with optical tweezers, *J. Chem. Phys. 112*, 5915.

31. Stottrup, B. L., Heussler, A. M., and Bibelnieks, T. A. (2007) Determination of line tension in lipid monolayers by Fourier analysis of capillary waves, *J.*

Phys. Chem. B 111, 11091.

32. Esposito, C., Tian, A., Melamed, S., Johnson, C., Tee, S. Y., and Baumgart, T. (2007) Flicker spectroscopy of thermal lipid bilayer domain boundary fluctuations, *Biophys. J. 93*, 3169.

33. Blanchette, C. D., Lin, W. C., Orme, C. A., Ratto, T. V., and Longo, M. L. (2007) Using nucleation rates to determine the interfacial line tension of symmetric and asymmetric lipid bilayer domains, *Langmuir 23*, 5875.

34. Zou, L., Wang, J., Basnet, P., and Mann, E. K. (2007) Line tension and structure of smectic liquid-crystal multilayers at the air-water interface, *Phys. Rev. E 76*, 031602.

35. Wintersmith, J. R., Zou, L., Bernoff, A. J., Alexander, J. C., Mann, J. A., Kooijman, E. E., and Mann, E. K. (2007) Determination of interphase line tension in Langmuir films, *Phys. Rev. E 75*, 061605.

36. Alexander, J. C., Bernoff, A. J., Mann, E. K., Mann, J. A., Wintersmith, J. R., and Zou, L. (2007) Domain relaxation in Langmuir films, *J. Fluid. Mech. 571*, 191.

37. McConnell, H. M., Rice, P. A., and Benvegnu, D. J. (1990) Brownian motion of lipid domains in electrostatic traps in monolayers, *J. Phys. Chem. 94*, 8965.

38. Klinger, J. F., and McConnell, H. M. (1993) Field gradient electrophoresis of lipid domains, *J. Phys. Chem. 97*, 2962.

39. Veatch, S. L., Cicuta, P., Sengupta, P., Honerkam-Smith, A., Holowka, D., and Baird, B. (2008) Critical fluctuations in plasma membrane vesicles, *ACS Chem. Biol. 3*, 287.

40. Seul, M., and Sammon, M. J. (1990) Competing interactions and domain-shape instabilities in a monomolecular film at an air-water interface, *J. Phys. Rev. Lett. 64*, 4728.

41. Langer, S. A., Goldstein, R. E., and Jackson, D. P. (1992) Dynamics of labyrinthine pattern formation in magnetic fluids, *Phys. Rev. A 46*, 4894.

42. Heinrich, M. C., Levental, I., Gelman, H., Janmey, P. A., and Baumgart, T. (2008) Critical exponents for line tension and dipole density difference from lipid monolayer domain boundary fluctuations, *J. Phys. Chem. B 112*, 8063.

43. Trabelsi, S., Zhang, S., Lee, T. R., and Schwartz, D. K. (2008) Linactants: Surfactant analogues in two dimensions, *Phys. Rev. Lett. 100*, 037802.

44. Trabelsi, S., Zhang, Z., Zhang, S., Lee, T. R., and Schwartz, D. K. (2009) Correlating linactant efficiency and self-assembly: Structural basis of line activity in molecular monolayers, *Langmuir 25*, 8056.

45. Simons, K., and Toomre, D. (2000) Lipid rafts and signal transduction, *Nat. Rev. Mol. Cell Bio. 1*, 31.

46. Allen, J. A., Halverson-Tamboli, R. A., and Rasenick, M. M. (2007) Lipid raft microdomains and neurotransmitter signalling, *Nat. Rev. Neurosci. 8*, 128.

47. Brown, D. A., and London, E. (1998) Structure and origin of ordered liquid domains in biological membranes, *J. Membr. Biol. 164*, 103.

48. Lajoie, P., and Nabi, I. R. (2010) Lipid rafts, caveolae, and their endocytosis, in *International Review of Cell and Molecular Biology* (Jeon, K. W., Ed.), Academic Press, Amsterdam.

49. Laude, A. J., and Prior, I. A. (2004) Plasma membrane microdomains: Organization, function and trafficking, *Mol. Membr. Biol. 21*, 193.

50. McIntosh, T. J., (Ed.) (2007) *Lipid Rafts*, Humana Press Inc., Totowa, NJ.

51. Roux, A., Cuvelier, D., Nassoy, P., Prost, J., Bassereau, P., and Goud, B. (2005) Role of curvature and phase transition in lipid sorting and fission of membrane tubules, *EMBO J. 24*, 1537.

52. Semrau, S., Idema, T., Holtzer, L., Schmidt, T., and Storm, C. (2008) Accurate determination of elastic parameters for multicomponent membranes, *Phys. Rev. Lett. 100*, 088101.

53. Parthasarathy, R., Cheng-han, Y., and Groves, J. T. (2006) Curvature-modulated phase separation in lipid bilayer membranes, *Langmuir 22*, 5095.

54. Mukherjee, S., and Maxfield, F. R. (2000) Role of membrane organization and membrane domains in endocytic lipid trafficking, *Traffic 1*, 203.

55. Hochmuth, R. M., Wiles, H. C., Evans, E. A., and McCown, J. T. (1982) Extensional flow of erythrocyte membrane from cell body to elastic tether. II. Experiment, *Biophys. J. 39*, 83.

56. Tian, A., Capraro, B. R., Esposito, C., and Baumgart, T. (2009) Bending Stiffness Depends on Curvature of Ternary Lipid Mixture Tubular Membranes, *Biophys .J. 97*, 1636.

57. Sorre, B., Callan-Jones, A., Manneville, J. B., Nassoy, P., Joanny, J. F., Prost, J., Goud, B., and Bassereau, P. (2009) Curvature-driven lipid sorting needs proximity to a demixing point and is aided by proteins, *Proc. Natl. Acad. Sci. U.S.A. 106*, 5622.

58. Tian, A., and Baumgart, T. (2009) Sorting of Lipids and Proteins in Membrane Curvature Gradients, *Biophys .J. 96*, 2676.

59. Heinrich, M. C., Tian, A., Esposito, C., and Baumgart, T. (2010) Dynamic sorting of lipids and proteins in membrane tubes with a moving phase boundary, *Proc. Natl. Acad. Sci. U.S.A. 107*, 7208.

60. Yuan, J., Hira, S. M., Strouse, G. F., and Hirst, L. S. (2008) Lipid bilayer discs and banded tubules: Photoinduced lipid sorting in ternary mixtures, *J. Am. Chem. Soc. 130*, 2067.

61. Bonifacino, J. S., and Rojas, R. (2006) Retrograde transport from endosomes to the trans-Golgi network, *Nat. Rev. Mol. Cell Bio. 7*, 568.

62. Derby, M. C., and Gleeson, P. A. (2007) New insights into membrane trafficking and protein sorting, *Int. Rev. Cytol. 261*, 47.

63. Safouane, M., Berland, L., Callan-Jones, A., Sorre, B., Romer, W., Johannes, L., Toombes, G. E. S., and Bassereau, P. (2010) Lipid cosorting mediated by Shiga toxin induced tubulation, *Traffic 11*, 1519.

64. Zemel, A., Ben-Shaul, A., and May, S. (2008) Modulation of the spontaneous curvature and bending rigidity of lipid membranes by interfacially adsorbed amphipathic peptides, *J. Phys. Chem. B 112*, 6988.

65. Groves, J. T. (2007) Bending mechanics and molecular organization in biological membranes, *Ann. Rev. Phys. Chem. 58*, 697.

66. Noid, W. G., Chu, J. W., Ayton, G. S., Krishna, V., Izekov, S., Voth, G. A., Das, A., and Anderson, H. C. (2008) The multiscale coarse-graining method. I. A rigorous bridge between atomistic and coarse-grained models, *J. Chem. Phys. 128*, 244114.

67. Flucher, B. (1992) Structural Analysis of Muscle Development: Transverse

Tubules, Sarcoplasmic Reticulum, and the Triad, *Dev. Biol. 154*, 245.

68. Leventis, P. A., Chow, B. M., Stewart, B. A., Iyengar, B., Campos, A. R., and Boulianne, G. L. (2001) Drosophila Amphiphysin is a Post-Synaptic Protein Required for Normal Locomotion but Not Endocytosis, *Traffic 2*, 839.

69. Razzaq, A., Robinson, I. M., McMahon, H. T., Skepper, J. N., Su, Y., Zelhof, A. C., Jackson, A. P., Gay, N. J., and O'Kane, C. J. (2001) Amphiphysin is necessary for organization of the excitation-contraction coupling machinery of muscles, but not for synaptic vesicle endocytosis in Drosophila, *Genes Dev. 15*.

70. Zelhof, A. C., Bao, H., Hardy, R. W., Razzaq, A., Zhang, B., and Doe, C. Q. (2001) Drosophila Amphiphysin is implicated in protein localization and membrane morphogenesis but not in synaptic vesicle endocytosis, *Development 128*, 5005.

71. Zhang, B., and Zelhof, A. C. (2002) Amphiphysins: Raising the BAR for Synaptic Vesicle Recycling and Membrane Dynamics, *Traffic 3*, 452.

72. Lee, E., Marcucci, M., Daniell, L., Pypaert, M., Weisz, O. A., Ochoa, G.-C., Farsad, K., Wenk, M. R., and De Camilli, P. (2002) Amphiphysin 2 (Bin1) and T-Tubule Biogenesis in Muscle, *Science 297*, 1193.

73. Peter, B. J., Kent, H. M., Mills, I. G., Vallis, Y., Butler, P. J. G., Evans, P. R., and McMahon, H. T. (2004) BAR domains as sensors of membrane curvature: The amphiphysin BAR structure, *Science 303*, 495.

74. Casal, E., Federici, L., Zhang, W., Fernandez-Recio, J., Priego, E.-M., Miguel, R. N., DuHadaway, J. B., Prendergast, G. C., Luisi, B. F., and Laue, E. D. (2006) The crystal structure of the BAR domain from human Bin1/Amphiphysin II and its implications for molecular recognition, *Biochemistry 45*, 12917.

75. McMahon, H. T., and Gallop, J. L. (2005) Membrane curvature and mechanisms of dynamic cell membrane remodelling, *Nature 438*, 590.

76. Blood, P. D., and Voth, G. A. (2006) Direct observation of Bin/amphiphysin/Rvs (BAR) domain-induced membrane curvature by means of molecular dynamics simulations, *Proc. Natl. Acad. Sci. U.S.A. 103*, 15068.

77. Takei, K., Slepnev, V. I., Haucke, V., and De Camilli, P. (1999) Functional partnership between amphiphysin and dynamin in clathrin-mediated endocytosis, *Nat. Cell Biol. 1*, 33.

78. Henne, W. M., Kent, H. M., Ford, M. G. J., Hegde, B. G., Daumke, O., Butler, P. J. G., Mittal, R., Langen, R., Evans, P. R., and McMahon, H. T. (2007) Structure and analysis of FCHo2 F-BAR domain: A dimerizing and membrane recruitment module that effects membrane curvature, *Structure 15*, 839.

79. Zimmerberg, J., and Kozlov, M. M. (2006) How proteins produce cellular membrane curvature, *Nat. Rev. Mol. Cell Bio. 7*, 9.

80. Frost, A., De Camilli, P., and Unger, V. M. (2007) F-BAR Proteins Join the BAR Family Fold, *Structure 15*, 751.

81. Yin, Y., Arkhipov, A., and Schulten, K. (2009) Simulations of Membrane Tubulation by Lattices of Amphiphysin N-BAR Domains, *Structure 17*, 882.

82. Gallop, J. L., Jao, C. C., Kent, H. M., Butler, P. J. G., Evans, P. R., Langen, R., and McMahon, H. T. (2006) Mechanism of endophilin N-BAR domain-mediated membrane curvature, *EMBO J. 25*, 2898.

83. Masuda, M., Takeda, S., Sone, M., Ohki, T., Mori, H., Kamioka, Y., and

Mochizuki, N. (2006) Endophilin BAR domain drives membrane curvature by two newly identified structure-based mechanisms, *EMBO J. 25*, 2889.

84. Arkhipov, A., Yin, Y., and Schulten, K. (2009) Membrane-Bending Mechanism of Amphiphysin N-BAR Domains, *Biophys. J. 97*, 2727.

85. Campelo, F., McMahon, H. T., and Kozlov, M. M. (2008) The Hydrophobic Insertion Mechanism of Membrane Curvature Generation by Proteins, *Biophys. J. 95*, 2325.

86. Blood, P. D., Swenson, R. D., and Voth, G. A. (2008) Factors Influencing Local Membrane Curvature Induction by N-BAR Domains as Revealed by Molecular Dynamics Simulations, *Biophys. J. 95*, 1866.

87. Heinrich, M. C., Capraro, B. R., Tian, A., Isas, J. M., Langen, R., and Baumgart, T. (2010) Quantifying membrane curvature generation of *Drosophila* amphiphysin N-BAR domains, *J. Phys. Chem. Lett. 1*, 3401.

88. Cuvelier, D., Derenyi, I., Bassereau, P., and Nassoy, P. (2005) Coalescence of membrane tethers: Experiments, theory, and applications, *Biophys. J. 88*, 2714.

89. Derenyi, I., Julicher, F., and Prost, J. (2002) Formation and Interaction of Membrane Tubes, *Phys. Rev. Lett. 23*, 238101.

90. Leibler, S. (1986) Curvature instability in membranes, *J. Phys. 47*, 507.

91. Sorre, B., Callan-Jones, A., Manneville, J.-B., Nassoy, P., Joanny, J.-F., Prost, J., Goud, B., and Bassereau, P. (2009) Curvature-driven lipid sorting needs proximity to a demixing point and is aided by proteins, *PNAS 106*, 5622.

Chapter 2: Optical Trapping Background and Techniques

Principles and Theory of an Optical Trap

Optical traps (optical tweezers) are used in the application of small forces (on the order of piconewtons) to, frequently, micron-sized dielectric particles by focusing an intense laser onto the particle and taking advantage of the resultant "radiation pressures" which act on the particle. The forces are mainly derived from considerations of the scattering of incident light rays and are readily calculated for particles both in the Mie-scattering (with radii much larger than the laser wavelength) and Rayleigh-scattering (with radii much smaller than the laser wavelength) regimes. The technique was first developed by Arthur Ashkin at AT&T Bell Laboratory, where he observed that small latex spheres could be pushed along a surface using only a focused CW laser(*1*). A trap was devised by the inclusion of a second similar but counter-propagating laser, fixing the position of the particle to an equilibrium location defined by the balancing of the forces exerted by each laser. A simpler design for an optical trap was later published which required only a single laser with a very steep intensity gradient near the focal point(*2*). The single-beam gradient trap relies on the balance of two components of the force exerted on the particle from the interactions (namely, reflection, refraction, dipole fluctuation induction) with the laser. The forces generated by the laser can be controlled such that the particle's position itself is held fixed with nanometer resolution(*3*), or the particle can be allowed to move but while applying a specified force with piconewton accuracy(*4*). Stable traps can only be generated when the index of refraction of the particle is higher than that of the surrounding medium, as will be discussed in greater detail later. For this reason, only systems which satisfy this condition will be

considered. The refractive index condition is not particularly limiting for biophysical applications, as many inorganic and biological particles have significantly higher indices of refraction than water or air, the mediums typically used in force and displacement measurements.

Within the Mie-scattering regime, a ray-optics approach yields an intuitive understanding of the optical trapping forces at work(*5*). The beam is considered to be a collection of individual photons with a common focus that is here approximated as a point, which is reasonable when the particle diameter is much larger than the beam waist (which scales with the laser wavelength). Figure 2.1 considers a bead at three different positions with respect to the focal point: above, below, and to the side. By assuming that the photons which are incident upon the bead are both transmitted and refracted (due to the change of medium), it is apparent that the same photons, upon exiting the bead, will have changed directions and thus momenta. Conservation of momentum dictates that the bead will have an equal and opposite change in momentum for each transmitted photon. In this manner, the momentum change of the bead is always directed towards the focal point of the laser. This force component is frequently termed the gradient force, and it is critical to the formation of a stable optical trap. Not shown in Figure 2.1 are the photons which are reflected off of the bead surface, "pushing" the bead in the direction of the photons. These photons lead to a second component termed the scattering force that causes the stable position of a trapped bead to be somewhat "downstream" (in the direction of the laser) of the focal plane.

Σp_{photon} : ↑ Σp_{photon} : ↓ Σp_{photon} : ←

Σp_{bead} : ↓ Σp_{bead} : ↑ Σp_{bead} : →
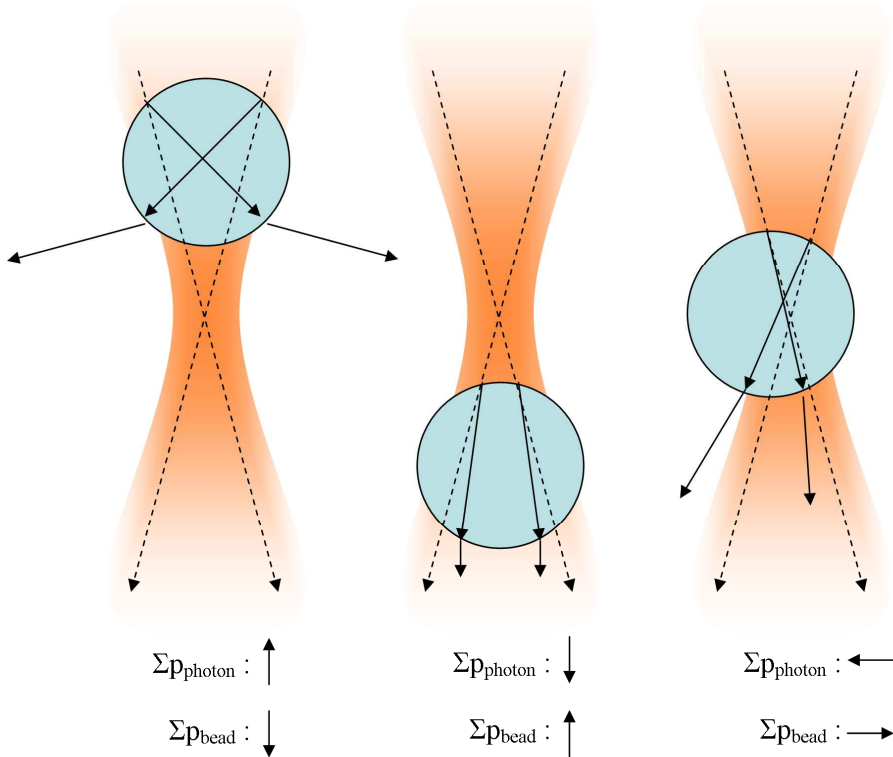
Figure 2.1: Simple ray-optics illustration of gradient force developing from consideration of photon momenta changes. Conservation of momentum dictates that, in each case, the bead experiences a change in momentum towards the focal point. Scattering forces arising from reflection are not shown, but will displace the bead "downstream" of the focal plane.

Particles whose radii are much less than the laser wavelength, ie, atoms and small molecules, can not be treated using the ray optics approach and instead the scattering and gradient forces must be considered using a quantum mechanical approach(*6*). The electric dipole approximation can be made because, for radiation in the visible or near-infrared, the wavelength is much larger than the particle radius. Under this approximation, the Lorentz law of force can be used to calculate the force on the dipole

in the field by(7),

$$F_{grad} = \frac{\alpha}{2}\nabla < E^2 >$$
(2.1)

where E is the electric field. The polarizability of the particle, α, is given by,

$$\alpha = n_m^2 r^3 \left[\frac{(n_p / n_m)^2 - 1}{(n_p / n_m)^2 + 2} \right]$$
(2.2)

where n_m and n_p are the indices of refraction of the medium and the particle, respectively, and r is the radius of the particle. Note that the gradient force is only attractive for particles with an index of refraction greater than that of the surrounding medium. The magnitude of the force increases with the gradient of the electric field, and so is amplified when a higher numerical aperture (NA) objective is used to focus the laser to a small focal volume. The scattering force, meanwhile, is given by,

$$F_{scattering} = \frac{n_m \sigma < S >}{c}$$
(2.3)

where σ is the scattering cross section of the particle, c is the speed of light, and $<S>$ is the time-averaged Poynting vector. As in the Mie regime, the scattering force acts along the direction of the laser and will displace the particle downstream of the focal plane until the gradient force (acting in the opposite direction) matches it.

Most particles used in optical traps fall into a size range which is not appropriate for the assumptions of either the Mie or Rayleigh regimes discussed above, but instead have diameters which are of the order of the laser wavelength. While there have been efforts to develop theoretical frameworks for this intermediate regime (see Neuman and Block(8) for a review), it is unlikely that a simple formalism will be developed which will prove useful for experimentalists in characterizing an optical trapping

instrument. Fortunately, the typical experiment is concerned only with the trap stiffness which enables measurements of forces on the order of 1-100 pN. For a well-aligned instrument, the gradient force will dominate the scattering force for particles which are close to the focal point; over a small range of displacements around this focal point, the gradient force increases linearly. A typical optical trap can then be modeled as a simple spring with a harmonic potential energy well. An externally applied force f will displace a bead from its resting position by,

$$\Delta x = \frac{f}{k} \tag{2.4}$$

where k is the trap stiffness, analogous to a spring constant. To measure an unknown external force requires knowledge of the displacement of the bead (see Chapter 2-D) and of the trap stiffness.

The stiffness of an optical trap can be calibrated by several methods (for recent reviews, see (*7-8*)), but here will be discussed the equipartition and drag-force methods. The equipartition method utilizes the Brownian motion of the trapped particle and the classical prediction that each translational degree of freedom of the bead will have, on average, energy of ½ k_BT. The variance in the bead position in the lateral plane (perpendicular to the laser), therefore, will be governed as

$$\text{var}(x) = \frac{k_B T}{k} \tag{2.5}$$

Measurements of the bead position can thus be used to directly determine the trap stiffness. This method has the advantage that nothing needs to be known about the system aside from the temperature, but it does require a detector with sufficient bandwidth to detect the larger (and shorter-lived) fluctuations, without which the

variance will be underestimated. Conversely, uncertainty caused by noise in the positional fits will lead to overestimation of the variance with a square dependence. This method is better suited to calibration of low-trap stiffness, where bead motion becomes more readily measurable (see Chapter 2-D).

An alternative is to use the drag-force method, which involves exerting a laminar flow against the bead at a known velocity. The flow will exert a drag force on a spherical particle as

$$f_{drag} = 2\pi\eta vr \tag{2.6}$$

where r is the bead radius, v is the flow velocity, and η is the viscosity of the medium. A constant flow velocity will create a constant drag force, displacing the bead from its zero-force position according to Eq. 4: at equilibrium, the drag force will be equal and opposite that of the trap force. The trap stiffness can then be calculated by measuring the displacement at a given flow velocity (see Chapter 2-D), though this requires accurate knowledge of the viscosity of the solution and the radius of the bead. It does not, however, depend on the bandwidth of the position detector nor does random fitting noise cause a significant problem, as positional data can be averaged to a precision given by the standard error of the mean. However, the drag-force method is typically better suited to calibrate high-stiffness traps for which larger and more reliable flow velocities (typically hundreds of μm/s) can be utilized. Thus, the drag-force and equipartition methods are complementary.

The ultimate stiffness of an optical trap depends on numerous factors. Alignment is critical, as is discussed in Section 3. Furthermore, both the predictions of Mie and Rayleigh regimes indicate that the steeper the convergence of photons at the focal,

the stronger the gradient force will be. High NA microscope objectives routinely serve double-duty as both imaging and trapping objective due in part to their ability to generate a large intensity gradient at the laser focal plane. The intensity gradient will also depend on the laser mode, beam shape, and polarization; special purpose optical traps (such as line optical traps(9-10) and Bessel traps(11-13)) will deviate from the more common TEM_{00}, spherical non-polarized beam. Laser power also impacts the trap stiffness; at the back aperture of the trapping objective, laser powers frequently used range in the hundreds of mW. Increasing the power can increase the stiffness by increasing the gradient force, but this is not a monotonic relation: at some high enough power, the scattering force becomes dominant. Of greater concern is the potential that stiffness can vary significantly depending on the trap position within the sample chamber, where weaker traps are formed deeper within the sample. Lastly, the trap stiffness will decrease if particles and media are chosen with similar indices of refraction, or for which the transmission of the laser wavelength is low.

Optical Trap Design Considerations

The schematic of the home-built optical trap used for all (force-based) experiments in this thesis is shown in Figure 2.2. The trap was designed around an inverted epifluorescence microscope (IX71; Olympus) and contains several elements common to all optical trap designs: a laser with sufficient power and stability (see Chapter 2-A and E), a high NA objective to focus the laser into a sample holder, a set of lenses to alter the beam waist to be slightly larger than the back-aperture of the trapping objective, mirrors to enable critical alignment of the beam through the optical train

24

(see Chapter 2-C), and a detection method to monitor the position of the force transducer (i.e., the trapped particle; see Chapter 2-A and D). In considering the design of an optical trap, there are a multitude of published trap layouts each with specific advantages and disadvantages as relates to measurement capability, complexity, and cost. Therefore, it is important to outline which capabilities are essential to the experiments which are to be performed.
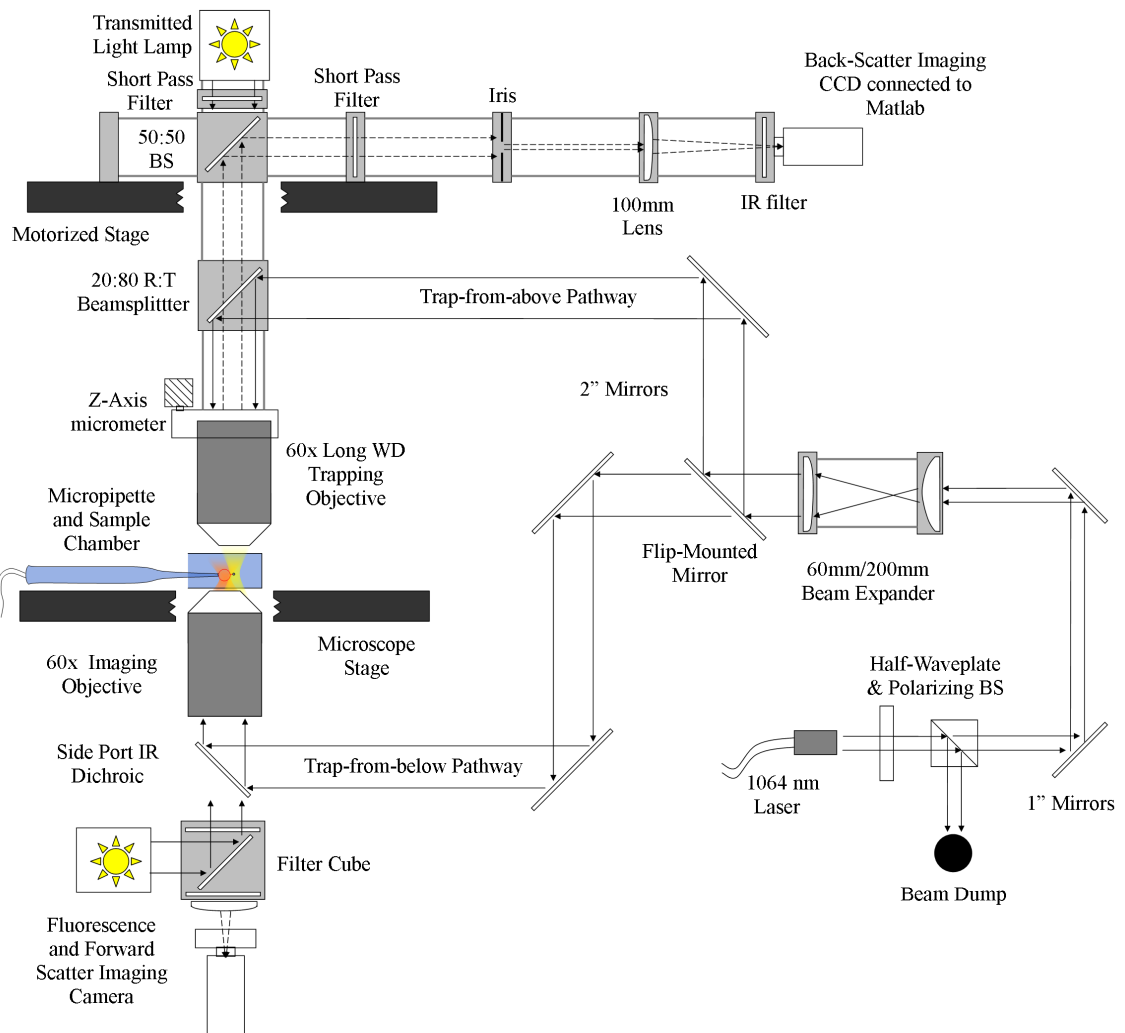
Figure 2.2: Design of an optical trap constructed around an inverted epifluorescence microscope. Laser power is stably modified through a half-wave plate and polarizing beamsplitter, utilizing only one of the resulting outputs. Beam expansion is accomplished with a 3.3x Keplerian telescope. One of two laser pathways is chosen via a flip-mounted 2" mirror, enabling selection between trapping-from-above or –below. The microscope-mounted imaging objective also serves as a trapping objective in the "below" pathway, while a second objective is used exclusively for trapping in the "above" pathway. In the latter, light from the transmitted light lamp of the microscope is focused onto the trapped bead and the resulting back-scattered light is collected for imaging by a CCD. The backscattered light is filtered to remove light from the laser (IR) as well as the fluorescence excitation light (green); an iris further reduces light from background (non-bead) sources.

For the purpose of the works reported in this thesis, the biophysical experiment consisted of using the trap to maneuver a streptavidin-coated microsphere into contact with an aspirated giant unilamellar vesicle (GUV), then, by retracting the bead, form a largely-cylindrical lipid bilayer tube from the connected vesicle. Positional freedom of the bead over a distance of several hundred micrometers (in one lateral direction) while maintaining a constant trap stiffness would be important; this requirement precluded the use of a single objective for both microscopic imaging and trapping, in which the positional freedom of the trap is limited to, at most, the field of view, and in practice as low as 100 μm. Since the positional freedom needed to extend in one direction over a macroscopic (mm) length scale, an optical trick was utilized. By mechanically

attaching the trapping objective and a mirror placed behind its back aperture at a 45°
angle, the connected optical system could be moved along a single direction over large
distances while maintaining the coaxial alignment between the laser and objective,
thereby ensuring constant laser power and beam profile at the trap focus. This is because
the laser beam, prior to entering the objective, was carefully collimated.

By mounting the objective and the 45° mirror onto a motorized xy-stage, we
gained the ability to reposition the bead a specifiable distance at a controlled velocity
through the use of computer commands (see Appendix: stage control with Labview and
Matlab code). This information is scientifically important for measurements of the
vesicle-tube behavior in both dynamic, nonequilibrium and equilibrium processes;
examples include the tube-length dependence of the force required to maintain the tube
and measurements of interlayer drag between monolayers of a lipid bilayer. It is also
useful to mechanically attach the bead position detector to the trapping objective, as the
important parameter in measuring force is not the bead's position in lab space, but rather,
its position relative to the center of the optical trap. In this design, bead detection is
accomplished through the use of a camera which records back-scattered incoherent light
from the bead. A camera provides a readily interpretable signal which is easily calibrated
through the use of commercially available calibration microscope slides that are etched
with a micrometer ruler. Additional optics are positioned between the 45° mirror and the
camera to enable the bead to be illuminated while still capturing a sufficient amount of
back-scattered light. The back-scattered light collected by the trapping objective is
collimated because the objective is infinity-corrected, so to form an image another lens
must be placed in front of the camera. A pinhole placed prior to this lens enables

much of the background light (originating from other glass surfaces for example) to be eliminated and a higher contrast (signal-to-noise) image to be obtained.

Additional components (laser power control, beam steering, beam shaping, illumination short pass filters, trapping-from-below, forming two simultaneous optical traps)

Aligning Methods

A laser beam can be aligned to any particular trajectory from any previous trajectory through the use of, at a minimum, two mirrors. The use of more than two mirrors may be preferable when space constraints dictate the beam follow a certain intermediate pathway, or when the final beam trajectory is perpendicular to the initial beam trajectory; when the final beam trajectory is roughly parallel or anti-parallel to the initial beam trajectory, two mirrors are readily sufficient. It is important to note that mirrors are typically characterized for reflection and transmission of light impinging the surface of the mirror along the normal (90°) axis or at a 45° angle to this axis; these values may depend significantly on the angle of incidence. For this reason, it may be worthwhile to use a third mirror in order to maintain reflection angles which are closer to that intended in the design of the mirror. We must keep in mind, however, that each additional optic in the system typically leads to greater complexity and cost, as well as loss of laser power and the introduction of more sources for aberrations such as ghost images (reflection off of the secondary surface(s) of each optic) and wavefront distortion.

In order to reposition a beam to its final trajectory, the "two-pinhole method" provides a systematic algorithm for the user. Consider the case of two mirrors which have been coarsely positioned to locate the beam near the desired final trajectory,

which is exactly marked by two consecutive irises (adjustable pinholes) (Figure 2.3). The mirrors in this example are mounted in kinematic mounts which provide (partially-decoupled) fine adjustment in two axes perpendicular to the beam propagation [note that gimbal mounts can provide fully-decoupled fine adjustments in two axes, but are not typically required in most situations]. The system therefore involves four degrees of freedom which are needed to achieve alignment of the beam through both irises. To start, the user adjusts the first mirror (M1) to pass the beam through the center of the first iris (I1), gradually closing the iris down to the beam waist to improve visualization of centration. I1 is then reopened fully, and the beam position is checked at I2. M2 is adjusted to pass the beam through the center of I2 in similar manner as in the first step. The adjustments to M2 will necessarily cause the beam to deviate at I1. The centration of the beam through I1 must be re-corrected using M1, and then re-corrected for I2 using M2. After each pass, the subsequent corrections needed will become progressively smaller. These steps can be repeated until the beam is observed to pass through both irises even after closing both down to the beam waist. Advanced users will note that the algorithm will converge to alignment faster if, instead of repositioning the beam with M1 only to the center of I1 in each step, the beam is instead positioned a little past the center (on the opposite end of where it started); by overshooting the center, the next iteration will require a smaller change of M1.
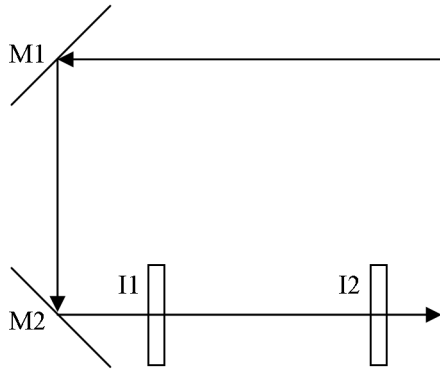
Figure 2.3: Beam alignment using the two-pinhole method. The original beam trajectory is changed to the final trajectory through the use of (at a minimum) two mirrors (M1 and M2). The mirror positions are adjusted to enable to the beam to pass through both irises (I1 and I2).

By its very nature, alignment is more qualitative than quantitative; systems will rarely (if ever) achieve "perfect" alignment, but fortunately the vast majority of cases will only require "good" alignment. Improvement in alignment can be attained with improvements in the sensitivity of the method against which alignment is checked. In the algorithm outlined above, the sensitivity can be readily improved by increasing the separation distance between the irises (Figure 2.3). It is worth noting that alignment sensitivity is also higher for beams with narrower waists due to the sharper appearance of the beam edge after passing through the (smaller) iris, but this may not be practical to adjust.

Beam alignment is critical when the laser is to be passed through lenses, as in the case of a beam expander. A beam expander may be as simple as a Keplerian telescope, where two lenses are placed at a separation distance equal to the sum of their focal

lengths. The beam waist of the laser after passing through the two lenses will be changed by the ratio of the lenses' focal lengths *f2/f1*; the waist is thereby enlarged when the first lens has the smaller focal length, and is decreased when the reverse is true. To minimize longitudinal aberrations, the more highly curved side of the lens should face the collimated beam. Centration of the beam with respect to the principle axis of the lenses will minimize lateral aberration, and can be achieved with the method described above where the irises are first used in place of the lenses. After inserting the two lenses, the beam profile should be checked for circularity, uniform brightness, and any noticeable clipping. Clipping occurs when the beam waist approaches or exceeds the diameter of the optic and will introduce significant wavefront distortion. Note that an optic placed at an angle to the beam will present an effectively smaller surface than the same optic oriented along the normal axis; a 1" mirror placed at a 45° angle will clip a circular beam with waist larger than 0.7".

Careful alignment of the beam must also be ensured with respect to the trapping objective. Following centration through the use of the two-iris method and after mounting the trapping objective, a camera can be used to image the laser beam profile near the focal plane. A well-aligned beam with minimal aberrations will generate a series of concentric bright and dark circles known as Airy disks which follow from the diffraction-limited nature of light. Any distortions introduced by the optical train will be observed in the pattern of the Airy disks, so these rings enable further improvements of alignment. Figure 2.4 shows several images of diffraction patterns to illustrate the results of common misalignment.
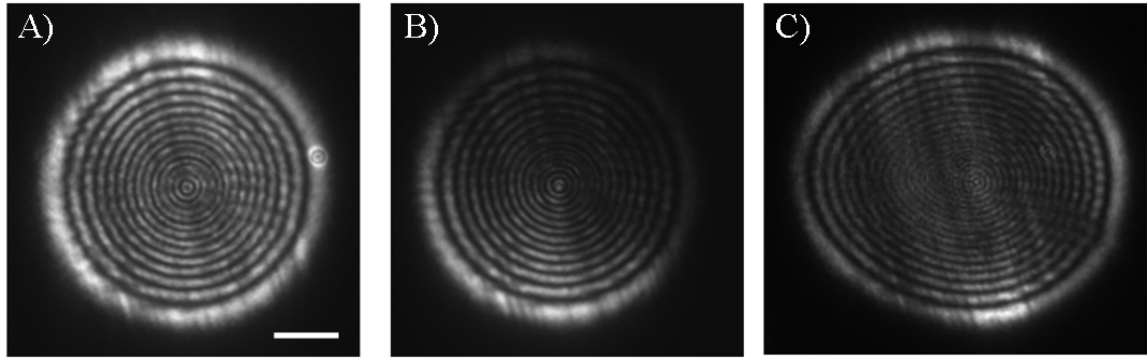
Figure 2.4: Airy disks observed near the focal plane of the laser can reveal alignment issues. A) A well-aligned beam with little distortion. A "ghost" reflection is evident on the right hand side of the outermost ring. Scale bar: 10 μm. B) The beam is passing parallel but off-axis through the trapping objective, leading to an uneven profile known as coma aberration. C) Wavefront distortion caused by slightly stressing (with a 3-point optic mount) the beamsplitter immediately prior to the trapping objective in the optical train.

Measuring Force

The most important reason for the widespread interest in optical traps is that forces on the order of 1-100 pN can be applied and measured for a range of physical and biological systems. These forces are frequently applied to the system of interest (e.g., a tubule pulled from a GUV) through a transducer (e.g., an optically-trapped microsphere). In order to measure a force with an optical trap, the trap must first be calibrated (see Chapter 2-A) to establish the trap stiffness. Trap calibration involves exerting known forces (typically drag or Brownian) and monitoring the position of the force transducer as it responds to these forces. Positional data can be collected by directly imaging the particle either with forward- or back-scattered light with the aid of a camera. The

images are then fit with appropriate algorithms (see below) to determine the center-of-mass position. If the position of the particle at any given time is compared to the position of the particle observed under zero external (non-trap) force, a force can be measured by presuming the trap acts as a simple spring: $f=k\Delta x$. This assumption is frequently valid over the majority of the range of force accessible as limited by the maximum or escape force. As the pertinent information is contained in the position of the particle relative to the trap center, it is necessary that the camera field-of-view remain centered on the trap's focal point. In the optical trap design outlined in Section 2, this is achieved by mechanically attaching the back-scatter camera to the trapping objective mount, ensuring that any change in the position of the trap within the sample chamber will relocate the camera field-of-view by the same amount.

The back-scatter imaging approach requires a very bright illumination source to yield a sufficiently high signal-to-noise image of an optically trapped bead. Figure 2.5A shows several images collected of an optically trapped 6 μm polystyrene bead under different illumination conditions. Illumination settings are chosen such that a high-contrast, bright ring is observed around the bead, leading to an image which can more readily be fit with a theoretical shape (here, a Gaussian ring). In general, the intensity of the light source should be maximized first before beginning to open the field diaphragm in attempting to achieve a properly exposed, high-contrast image. The use of a bright illumination source for back-scatter imaging can cause difficulties in simultaneously obtaining properly exposed forward-scatter (ie, transmitted light) or fluorescence images; Section 2 discusses the use filters to enable both back-scatter and fluorescence imaging.
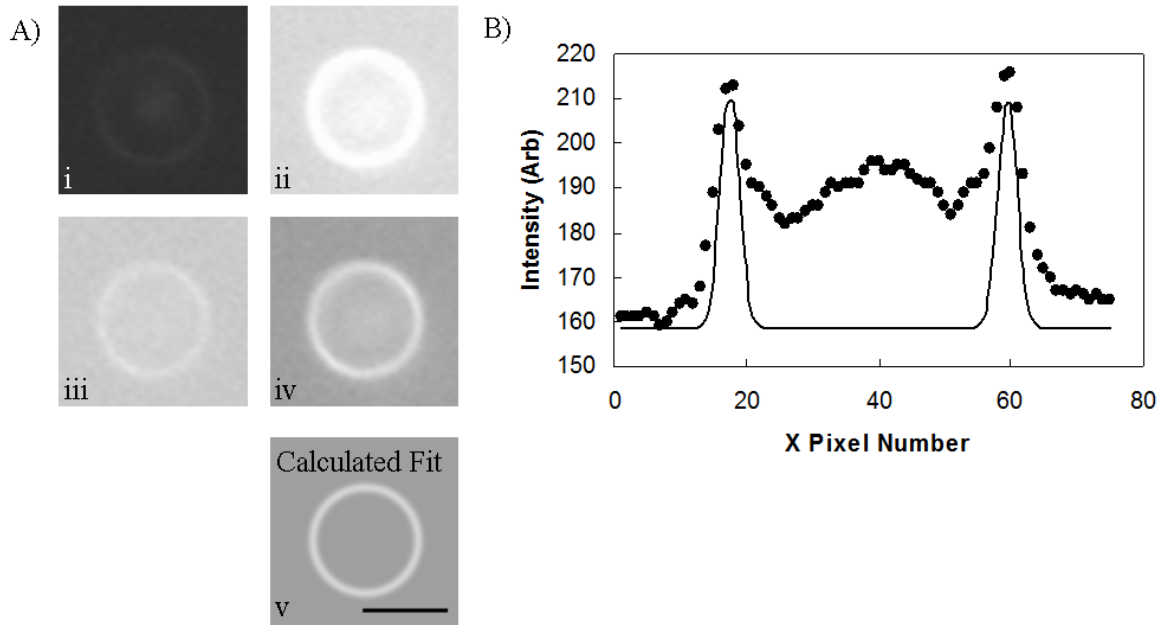
Figure 2.5: Sample of 6 µm polystyrene bead back-reflection images. A) Contrast of the halo surrounding the bead is dependent on illumination intensity and cone angles (as set by the field diaphragm). Images i and ii are under- and over-exposed, respectively, while iii is low in contrast due to the field diaphragm having been opened instead of maximizing the light intensity. Image iv is optimized for contrast, and v is the calculated image of the resulting Gaussian ring fit to iv. Scale bar: 5 µm. B) Line scan through the center of images iv and v. Ring center (X_0, Y_0) and radius (R_0) were used as fit parameters, while the parameters a, b and σ were automatically estimated from the experimental image.

The back-reflected light from a spherical bead generates an image of a halo which has a Gaussian intensity profile across its edge. This image is readily modeled by a Gaussian ring function of the form:

$$\overline{\overline{Gaussian\_Ring}} = a \cdot \exp\left(\frac{-(\overline{\overline{R}} - R_0)^2}{\sigma}\right) + b$$

$$\overline{\overline{R}} = \sqrt{\left(\overline{\overline{X}} - X_0\right)^2 + \left(\overline{\overline{Y}} - Y_0\right)^2}$$

where a double overline indicates the quantity is a matrix. The matrices X and Y are of the same size as the image dimensions (N_Y by N_X) and are used to describe pixel positions, taking the form:

$$\overline{\overline{X}} = \begin{matrix} 1 & 2 & 3 & ... & N_X \\ 1 & 2 & 3 & ... & N_X \\ 1 & 2 & 3 & ... & N_X \\ ... & ... & ... & ... & ... \\ 1 & 2 & 3 & ... & N_X \end{matrix} \qquad \overline{\overline{Y}} = \begin{matrix} 1 & 1 & 1 & ... & 1 \\ 2 & 2 & 2 & ... & 2 \\ 3 & 3 & 3 & ... & 3 \\ ... & ... & ... & ... & ... \\ N_Y & N_Y & N_Y & ... & N_Y \end{matrix}$$

The Gaussian ring function contains the center-of-mass bead position as coordinates (X_0, Y_0), as well as the bead radius R_0, an important parameter when considering drag forces (see Chapter 2-A). The remaining fit parameters do not contain critical information relevant to force measurement. Background intensity is accounted for with b, while the ring brightness and width are fit with a and σ. By determining sufficiently good guesses, these parameters can be held fixed during image fitting in order to decrease fit computation time and improve force measurement rate. Code written for Matlab (see Appendix: Matlab code) handles image acquisition and bead position fitting, displaying force measurements in real-time at a rate of ~15-20 Hz. The code utilizes the built-in Matlab function *fminsearch* – an unconstrained nonlinear optimization algorithm – to minimize the sum of the squared errors (SSE) calculated between the actual and the calculated ring images (Figure 2.5B). Error tolerances can be set fairly high at 1E-2 in order to decrease the number of fit iterations per image, thereby improving the force

measurement rate for real-time applications. While a Gaussian ring clearly does not perfectly mimic the experimental images obtained (compare line scans shown in Figure 2.5B), it yields fairly high positional accuracy (see below). More complex mathematical functions might increase accuracy slightly, but would also engender a higher computational cost and a potentially lower real-time force measurement rate.

Typical lateral uncertainties for the algorithm in practice are on the order of 4 nm; Figure 2.6A shows the distribution of positional fits obtained for a bead fixed to a glass coverslip. For a trap with stiffness of 0.05 pN/nm, this translates into a force uncertainty of 0.2 pN resulting purely from fitting error. It is observed through the distribution of positional fits for a trapped bead with stiffness of 0.05 pN/nm (Figure 2.6B) that including the Brownian motion of a bead leads to a larger (compound) uncertainty of 10 nm in the position and 0.5 pN in the force. It is evident then that the majority of uncertainty in a measurement of any external force is due to the Brownian positional fluctuations, with a smaller contribution from instrument limitations. This is further made clear by the alternative equipartition method of determining optical trap stiffness, which predicts a stiffness for this particle of 0.06 pN/nm, in good agreement with the drag-force determined value of 0.05 pN/nm. It is expected that the equipartition method will become less reliable as the Brownian fluctuations approach the fitting error uncertainty.
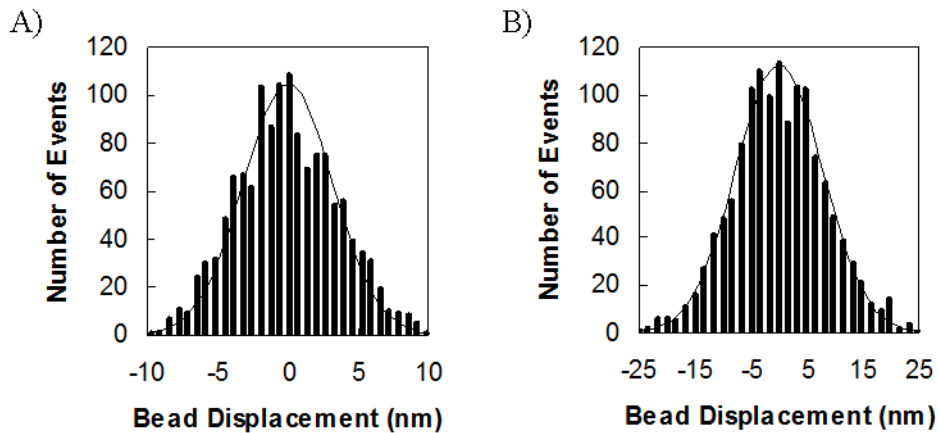
Figure 2.6: Histograms of bead positions from fitting back-reflection images with a Gaussian ring function. A) A bead dried onto a coverslip is used to determine the instrumentational limit of positional uncertainty of ~4 nm, here the standard deviation of the Gaussian distribution. B) An optically trapped bead in DI water displays a larger range of displacements from the mean due to the Brownian motion. The standard deviation is ~10 nm, which leads to a force uncertainty of 0.5 pN at a trap stiffness of 0.05 pN/nm.

Calibration of the optical trap is typically performed using the drag-force method (see Chapter 2-A), where a hydrodynamic flow exerts a constant force on the bead, resulting in the bead being displaced somewhat from the trap center (i.e. the zero net-external force position); sample data is provided in Figure 2.7A where a 6.01 µm bead is periodically dragged at ±378 µm/s in deionized water. Resulting positional fits are themselves fit with a step function to determine the net bead displacement, and the process may be repeated for a range of velocities (Figure 2.7B). In treating the optical trap as a simple spring, the displacements are expected to follow a linear dependence on

the drag velocity, with slope inversely proportional to the trap stiffness:

$$\frac{\Delta x}{v} = 2\pi \frac{r\eta}{k}$$
(2.7)

from which the stiffness of the trap measured in Figure 2.7B is determined as 0.06 pN/nm. Equation 2.7 is valid over most of the force range dictated by the maximal force capable of being generated at a given trap stiffness, but deviations may be observed as the escape velocity is approached.
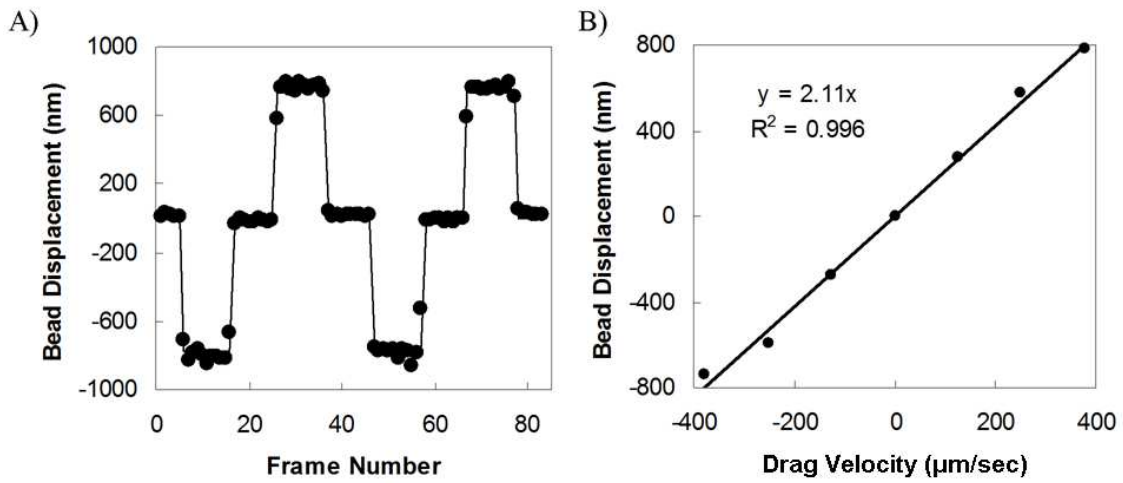
Figure 2.7: Drag force calibration of trap stiffness. A) A trapped bead was dragged periodically at ±378 μm/s, generating roughly constant hydrodynamic forces to displace the bead at fixed distances from the trap center. Circles indicate bead displacements determined from image fitting, while the solid line represents a step function fit to the data. B) The bead displacements determined from step function fits (as in A) plotted against the drag velocities utilized in a typical calibration. Solid line indicates a single-parameter linear fit with slope proportional to the trap stiffness (e.g. spring constant).

Characterization of the Instrument Performance

The performance of a well-aligned optical trap can be characterized in terms of the maximum and minimum stiffness obtainable, as well as the behavior of the trap over long time-scales. Figure 2.8 demonstrates two key aspects over a time period of several minutes. First, an ideal trap position (i.e. zero force position) would not be subject to slow drift (see Figure 2.6B for short-term fluctuations unrelated to beam performance). The trapped bead in Figure 2.8 is largely maintained within ±20 nm of the average (zero force) position over the period of 500 seconds. Second, the stiffness of the ideal trap would also not suffer any long-term variation. In Figure 2.8, the variance in position over any subset region of ~100 seconds is roughly constant; since positional fluctuations are proportional to the trap stiffness (Equation 2.5), this indicates that the trap stiffness can also be maintained over at least a 500 second interval.
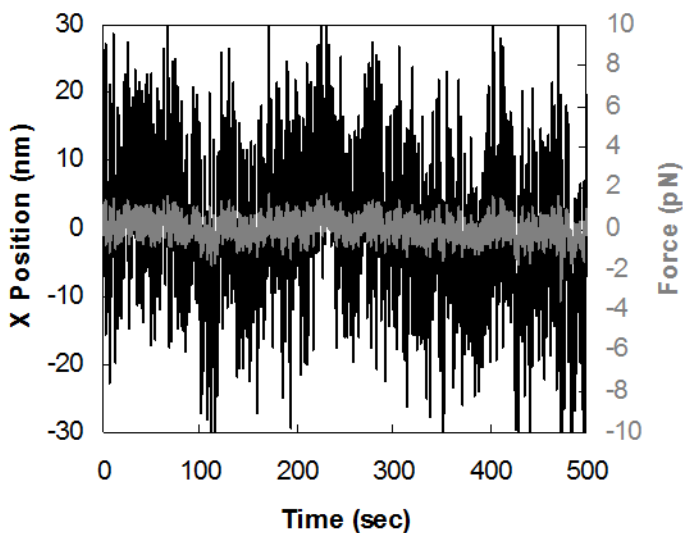
Figure 2.8: The long-term positional stability of a trapped 6 μm bead in 1M sucrose

is observed to remain within 20 nm of any short-term average of the 500 second interval here measured. The slow oscillation likely corresponds to laser pointing drift. The variance in position over any short-term (~100 s) region remains roughly constant, indicating that the trap stiffness remained stable and within initial uncertainty over the long term.

References

1.   Ashkin, A. (1970) Acceleration and Trapping of Particles by Radiation Pressure, *Phys. Rev. Lett. 24*, 156.
2.   Ashkin, A. (1978) Trapping of Atoms by Resonance Radiation Pressure, *Phys. Rev. Lett. 40*, 729.
3.   Visscher, K., Gross, S. P., and Block, S. M. (1996) Construction of multiple-beam optical traps with nanometer-resolution position sensing, *IEEE Journal of Selected Topics in Quantum Electronics 2*, 1066.
4.   Visscher, K., Scnitzer, M. J., and Block, S. M. (1999) Single kinesin molecules studied with a molecular force clamp, *Nature 400*, 184.
5.   Ashkin, A. (1992) Forces of a single-beam gradient laser trap on a dielectric sphere in the ray optics regime, *Biophys .J. 61*, 569.
6.   Gordon, J. P., and Ashkin, A. (1980) Motion of atoms in a radiation trap, *Phys. Rev. A: At., Mol., Opt. Phys. 21*, 1606.
7.   Svoboda, K., and Block, S. M. (1994) Biological applications of optical forces, *Annu. Rev. Biophys. Biomol. Struct. 23*, 247.
8.   Neuman, K. C., and Block, S. M. (2004) Optical trapping, *Rev. Sci. Instrum. 75*, 2787.
9.   Biancaniello, P. L., and Crocker, J. C. (2006) Line optical tweezers instrument for measuring nanoscale interactions and kinetics, *Rev. Sci. Instrum. 77*, 113702.
10.   Dasgupta, R., Mohanty, S., and Gupta, P. (2003) Controlled rotation of biological microscopic objects using optical line tweezers, *Biotech. Lett. 25*, 1625.
11.   Garces-Chavez, V., McGloin, D., Melville, H., Sibbett, W., and Dholakia, K. (2002) Simultaneous micromanipulation in multiple planes using a self-reconstructing light beam, *Nature 419*, 145.
12.   Dholakia, K., and Lee, W. M. (2008) Optical trapping takes shape: The use of structured light fields, *Adv. At., Mol., Opt. Phys. 56*, 261.
13.   Arlt, J., Garces-Chavez, V., Sibbett, W., and Dholakia, K. (2001) Optical micromanipulation using a Bessel light beam, *Opt. Commun. 197*, 239.

Chapter 3: Experimental Systems: Methods and Theory

Monolayer[d]

Materials and Experimental Methods

Monolayers were formed of mixtures of dimyristoylphosphatidylcholine (DMPC) and dihydrocholesterol (DChol), with a trace amount (0.5 mol%) of rhodamine-labeled dioleoylphosphatidylethanolamine (rhoPE) used as a fluorescent dye. This dye is known to preferentially partition into the liquid-disordered phase, leading to those domains appearing brighter in fluorescence images and (importantly) enabling visualization of domain boundaries. Individual lipid stock concentrations were determined via phosphate analysis(*1*) following acid digestion of organic compounds. Mixtures of lipids were prepared immediately prior to use in forming monolayers over a subphase of phosphate buffered saline (PBS: 7.5 mM phosphate, 140 mM NaCl) at pH7.4 with 5 mM dithiothreitol (DTT). DTT was used to reduce oxidation of lipids, as the intense illumination required for fluorescence imaging can potentially cause photo-induced oxidation of both fluorophores and adjacent lipids. Attempts were also made to reduce photo-oxidation by replacing the air above the monolayer (contained within a cover) with argon gas, but no significant reduction in the bleaching times of the fluorophore were observed, so this technique was not typically employed.

A Langmuir trough (MicroTroughX; Kibron Inc., Helsinki, Finland) was filled with ~25 mL of PBS to ensure complete wetting of the hydrophilic area (and especially of the edge formed by the surrounding hydrophobic Teflon coating) of the trough prior to depositing 10 nmol of lipid solution onto the air-subphase interface with a glass syringe.

---

[d] Parts of this chapter are reproduced from previously published work: Heinrich, M. C., Levental, I., Gelman, H., Janmey, P. A., and Baumgart, T. (2008) Critical exponents for line tension and dipole density difference from lipid monolayer domain boundary fluctuations, *J. Phys. Chem. B 112*, 8063.

Monolayer barriers were initially set such that the lipid film was contained within ~2/3 of the total interfacial area. The clear viewing window of the trough was centered over a long-working distance (LWD), 60x, 1.1 numerical aperture, water-immersion microscope objective with coverslip correction mounted on an inverted epifluorescence microscope (IX81; Olympus, Center Valley PA). The height of the monolayer was then lowered to within reach of the working distance of the microscope objective by slowly removing the excess subphase from the outside of the monolayer barriers.

The newly-prepared monolayer was first compressed quickly (25 Å^2/molecule/min) through the transition pressure while the surface pressure was monitored using the Wilhelmy method(1) and the FilmWare software package (Kibron). The transition pressure was recorded as the last pressure at which heterogeneity could still be observed in fluorescence images. The single-phase monolayer was allowed to thermodynamically equilibrate for several minutes before slowly (5 Å^2/molecule/min) lowering the surface pressure below the transition pressure until stable domains could be observed. In the intermediate range between the transition and this lower pressure, domains would form, fragment, and coalesce with neighbors on a time scale of seconds, reflecting a variety of shape instabilities that have been explored by other works(2-4). Below this shape instability regime, domains will persist on the time-scale of an experiment, typically tens of minutes.

Fluorescence images were recorded with a back-illuminated electron multiplying charge-coupled device (EM-CCD) camera (ImagEM; Hamamatsu, Bridgewater, NJ) with a pixel edge size of 264nm, close to the optical point spread function width of the microscope. The frame rate was increased to 60 fps by utilizing a smaller region of

the chip (256x256 pixels, compared to the full frame of 512x512), enabling a shorter exposure time of 0.016 s/frame. Note that the frame rate depends both on the exposure time and a per-frame finite readout time. A higher fps was important to increase the achievable number of frames of a given domain given that the constant illumination used in epifluorescence led to significant photobleaching on a time scale of tens of seconds. It was furthermore important to minimize frame exposure time for the domain shape analyses discussed in both the capillary wave and hydrodynamic decay theories discussed below: longer exposure time leads to the "averaging out" of small, short-lived fluctuations in domain boundaries.

Monolayers were maintained at constant surface pressures during imaging. Several >2000 frame movies were collected at each pressure such that 10 domains would be accessible for statistically-significant shape analysis as described below. A slow flow was frequently observed at the monolayer which was compensated through manual microscope stage translation to maintain a roughly-constant field of view with respect to particular domains.

Capillary Wave Theory

In order to accurately measure the line tension of phase-separated monolayers, we examine two different theoretical approaches that explain the fluctuations of the boundary line between a small region of one liquid phase (a domain) and the surrounding second liquid phase. These fluctuations are shown to depend on the line tension at the domain boundary, which in turn depends on the proximity to the critical surface pressure/composition at which the thermodynamic properties of the two phases

become equivalent. At the critical pressure, the line tension becomes vanishingly small(*5*)

and domains of all sizes become unstable, fragmenting and reforming rapidly. Above the

critical pressure, the monolayer coalesces into a single supercritical liquid phase.

It has been shown by several authors(*2, 6-7*) that a Fourier ansatz for the shape of

a fluctuating domain parameterized in terms of radius R and polar angle ϑ:

$$R(\vartheta) = R_0 + \zeta_n \sum_n \cos n\vartheta$$

(3.1)

yields the excess energy (relative to a non-fluctuating domain) of a fluctuation mode with

number n, where $n=\{2,3,...\}$; modes $n=0$ and $n=1$ refer to uniform expansion and

translation of the domain, respectively, and are here unimportant. This mode-dependent

excess energy is given to second order in mode amplitudes ζ_n as

$$E_n = \frac{1}{2}\Omega_n \zeta_n^2$$

(3.2)

Here, Ω_n is a restoring force constant for the mode n. In the case of lipid monolayers, it

includes contributions from line tension γ at the phase boundary, and the dipole density

difference between coexisting phases, μ. Stone and McConnell(*8*) express the force

constant as

$$\Omega_n = \frac{\pi\mu^2(n^2-1)}{R_0}\ln\frac{R_n}{R_0}$$

(3.3)

Here, the equivalent radius R_0 is related to the domain area A by $R_0 = (A/\pi)^{1/2}$ and R_n is

the radius above which a domain will distort into non-circular fluctuation modes with n-

fold symmetry(*9-11*). In Equation 3.3, this is observed as a negative force constant for a

domain with radius $R_0>R_n$, resulting in an energetic instability and loss of area

conservation due to frequent fragmentation and merger of adjacent domains. R_n is a

44

function of γ, as well as a microscopic cut-off in terms of the separation distance, δ, of adjacent lipid molecules(*9-11*):

$$R_n = \left(\frac{\delta}{4}\right) \exp(Z_n) \exp\left(\frac{\gamma}{\mu^2}\right)$$

(3.4)

where Z_n is the mode-dependent shape transition exponent. The unknown distance δ presents a challenge in using this approach to analyze fluctuations of domains in determining the line tension.

An alternative expression for the force constant results from the thin film limit of a theory developed for magnetic layers with phase coexistence(*12-13*):

$$\Omega_n = \frac{\pi\gamma}{R_0} \beta_n$$

(3.5)

where β_n is a function of γ and μ and also depends on a "smooth cutoff" in terms of the film thickness h(*13*):

$$\beta_n = \left[1 - \frac{1}{2} N_B \ln\left(\frac{8R_0}{eh}\right)\right](n^2 - 1) - \frac{1}{4} N_B (1 - 4n^2) \sum_{j=2}^{n} \frac{1}{2j-1}$$

(3.6)

Note that the form of β_n in Refs (*13-14*) contains a sign error (R. Goldstein, personal communication). In Equation 3.6, the so-called Bond number is defined as $N_B = 2\mu^2/\gamma$. More generally, the Bond number is a dimensionless number in the theory of fluid mechanics expressed as the ratio between one quantity proportional to fluid density (here dipole density) difference, and a second quantity proportional to interfacial tension (here line tension), and is therefore frequently used to describe shapes of three-dimensional systems such as bubbles or droplets in another fluid. Many properties, including domain shape stability, depend sensitively on the value of N_B(*11*).

Both Equations 4 and 5 can be used to determine line tension γ, and dipole density difference, μ. Hence, values of these parameters from Fourier analysis of fluctuating domains are model dependent. In the present study, we will focus on using the second approach (Equation 3.5). This allows comparison with the results in Ref. (*13*), and enables us to benefit from the fact that the dependence of fit results on the "smooth cutoff", i.e. the film thickness h, has been discussed and found to be small(*13*). In all subsequent analysis below, we assume $h = 1$ nm(*13*).

Systems that do not have a significant dipole density difference (such as a phase-separated monolayer far from the critical point, or a bilayer where the additional aqueous half-space provides additional screening(*15*)) can be approximated by the simplified force constant $\Omega_n = \pi\gamma(n^2 - 1)/R_0$ as obtained from either Equation 3.4 or 3.5 by taking the limit $\mu = 0$. In this case, $N_B = 0$ and the mode energy is $E_n = \dfrac{\pi\gamma}{2R_0}(n^2 - 1)\zeta_n^2$. By assuming equipartition of fluctuation energy between all modes (see also below), it is convenient to consider the average energy of any given mode relative to the lowest fluctuating mode number $n=2$: $\dfrac{\langle E_2 \rangle}{\langle E_n \rangle} = \dfrac{3}{(n^2 - 1)} \dfrac{\langle \zeta_2^2 \rangle}{\langle \zeta_n^2 \rangle} = 1$. This relation is rearranged to give:

$$\frac{\langle \zeta_2^2 \rangle}{\langle \zeta_n^2 \rangle} = \frac{(n^2 - 1)}{3} \tag{3.7}$$

which indicates that a plot of the ratio of the average mode amplitudes $\langle \zeta_2^2 \rangle / \langle \zeta_n^2 \rangle$ vs. $(n^2 - 1)$ will follow a straight line with zero intercept and a slope of 1/3 for any system in which the dipole density difference is zero (or sufficiently small). A deviation from

46

this trend (see Figure 3.1) is evidence that, in the lipid monolayer system studied, the dipole density difference makes a significant contribution to the effective line tension considered in simpler models(16). For this system, the ratio β_n / β_2 as defined by Equation 3.6 will be utilized to determine the experimental Bond number N_B.
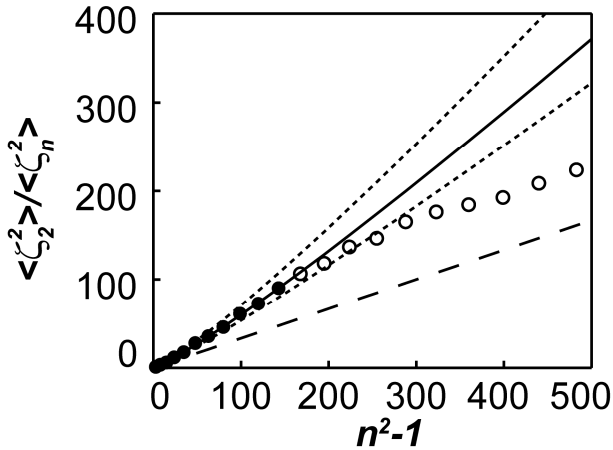
Figure 3.1: FFT-determined mode power ratios $\langle \zeta_2^2 \rangle / \langle \zeta_n^2 \rangle$ for a single domain of radius 7.8 μm at a pressure of 8.25 mN/m at the critical composition. Closed circles are modes which are able to be accurately resolved (see Image Analysis below), while open circles are higher modes that are not fully resolved. The solid line is a fit of the function β_n / β_2 to the experimentally-resolved modes via the single fit-parameter N_B; dotted lines indicate sensitivity of the fit to changes in N_B of ± 5%. Both the mode powers and the fit indicate a significant deviation from the zero-dipole density difference case for which N_B=0 and the slope of this plot would be 1/3 (dashed line).

Equation 3.5 (and Equation 3.3) assume that domain area is conserved, which is valid for small fluctuations below pressures leading to branching instabilities. We

47

can use Equation 3.5 to define the conditions for the stability of the circular ground state shape towards transitions to ground states of different symmetry(9-11, 13). With increasing Bond number, the first instable mode is found for $n = 2$, and from Equation 3.6, the critical Bond number below which the circular shape is stable is obtained(13) by setting $\beta_2 = 0$:

$$N_B^*(2) = \frac{2}{\ln(8R_0/h) - 11/6}$$

(3.8)

Note that this critical Bond number is dependent on domain radius, whereas N_B is not. Alternatively, for fixed Bond number, Equation 3.8 can be used to define a critical radius above which circular domains are instable(9-11, 13). All fluctuation spectra examined in the present contribution were obtained from domains with N_B values below the critical Bond number defined by Equation 3.8 (Figure 3.2).
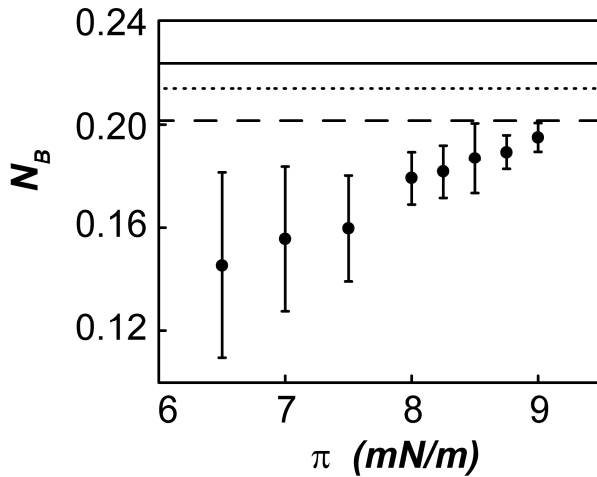
Figure 3.2: Range and average values of N_B as a function of surface pressure for the critical composition. Horizontal lines indicate the 2nd-mode critical Bond numbers $N_B^*(2)$ for domains of radii equal to 16 (dashed line), 9 (dotted line), and 6 μm (solid line),

corresponding to the largest, average, and smallest domain size, respectively, used in this study. Although N_B increases monotonically with pressure, it remains below the critical Bond number for all domains included; larger domains would have Bond numbers greater than the critical lines indicated and were therefore not included in determination of line tension and dipole density difference.

For the condition $N_B < N_B^*(2)$, the assumption of thermal equipartitioning, i.e. an energy of 1/2 $k_B T$ per fluctuation mode, yields the following expression for the mode amplitudes(*13*):

$$\left\langle \varsigma_n^2 \right\rangle = \frac{k_B T R_0}{\pi \gamma \beta_n}$$

(3.9)

where k_B is Boltzmann's constant. Note that thermal energy equipartitioning requires the experimental realization of quadratic degrees of freedom (Equation 3.2), which will lead to a Gaussian probability distribution of mode amplitudes. This condition was recently confirmed in the case of fluctuating bilayer domains(*17*). After determining the Bond number (and, therefore, β_n) as shown in Figure 3.1, Equation 3.9 can be used to determine the line tension γ for a given domain. Finally, the dipole density difference is ascertained from the definition of the Bond number $N_B = 2\mu^2/\gamma$.

Hydrodynamic Mode-Amplitude Time Decay Theory

The preceding discussion of capillary wave theory utilizes statistical averages of mode powers for a fluctuating domain to determine both line tension and dipole density difference. An alternative approach was used by Stone and McConnell to relate the

energy dissipation, D, of an excited mode n over time due to viscous drag within the monolayer subphase:

$$D = \pi^2 \eta R_0 \dot{\zeta}_n^2 \frac{(2n+1)(2n-1)}{4n^2}$$ (3.10)

where η is the subphase viscosity. Note that the time-derivative of the squared mode amplitude is used in Equation 3.10. By equating the energy dissipation to the rate of electrostatic-line tension energy loss (eg, the time-derivative of Equation 3.2), we obtain after integration an exponential relation $\zeta_n(t) \propto \exp(-t/\tau_n)$ with characteristic decay constant τ_n:

$$\tau_n = \frac{\pi \eta R_0^2}{\gamma} \frac{(2n+1)(2n-1)}{4\beta_n n^2}$$ (3.11)

In similar manner as in the capillary wave theory approach, we consider the ratio τ_2/τ_n:

$$\frac{\tau_2}{\tau_n} = \frac{15}{16} \frac{4n^2}{(2n+1)(2n-1)} \frac{\beta_n}{\beta_2}$$ (3.12)

from which we note that a plot of experimental time decay constant ratios can be fit with Equation 3.6 (Figure 3.3), again using the Bond number as the single fit parameter. Note that the ratio $\beta_n / \beta_2 = (n^2 - 1)/3$ when $N_B=0$, so the plot in Figure 3.3 is expected to be linear only in the absence of dipolar effects. Comparisons can then be made between Bond numbers determined via the static (capillary wave theory) and dynamic (mode-amplitude decay theory) models.
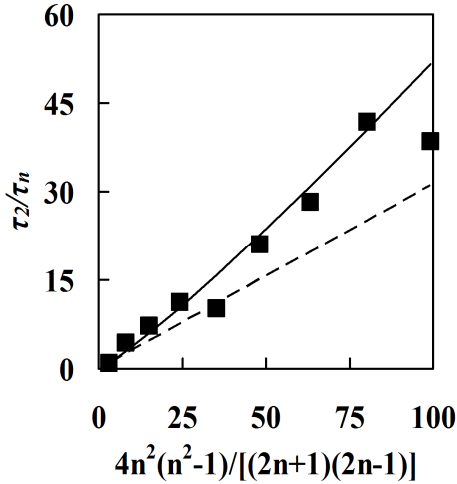
Figure 3.3: Time-autocorrelation-determined decay constant ratios τ_2/τ_n for a single domain of radius 11.3 μm at a pressure of 8.0 mN/m at the critical composition. The solid line is a fit of the function β_n/β_2 to the experimentally-resolved modes via the single fit-parameter N_B; dotted lines indicate sensitivity of the fit to changes in N_B of ± 5%. Both the mode powers and the fit indicate a significant deviation from the zero-dipole density difference case for which $N_B=0$ and the slope of this plot would be 1/3 (dashed line).

Image Analysis

All image processing was performed using MATLAB (The Mathworks, Natick, MA). Our code allowed user-selection of individual domains in multi-domain frames; the tracing routine automatically centered and cropped to the neighborhood around the same identified domain in all subsequent frames, thus allowing tracking and localization frame by frame. The original gray-scale images were converted to binary via thresholding, and the domain boundary for each image was determined from the binary frames and parameterized as the radius function $R(\theta)$, where θ is the polar angle (Figure

51

3.4A). Image frames where the area of the domain changed by more than 3% were discarded. Area changes of those magnitudes were attributed to motion blur, departure of the domain from the field-of-view due to flow or diffusion, or other imaging artifacts. From the domain area, A, the equivalent radius $R_0 = (A/\pi)^{1/2}$ was obtained. R_0 therefore refers to the radius of a non-fluctuating domain with equal area.
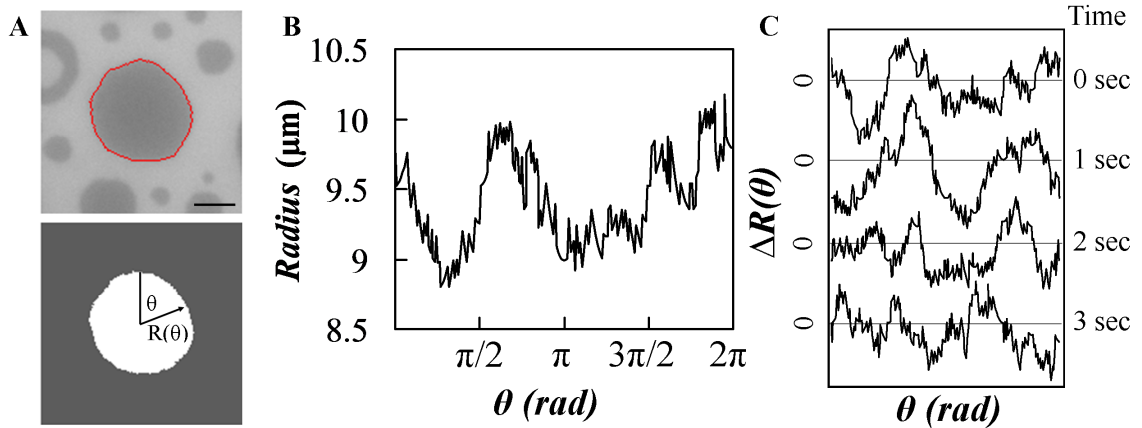
Figure 3.4: A) Fluorescence image (top) following thresholding and binarization (bottom) to determine domain boundary. Scale bar: 10 μm. B) Radius as a function of angle for the domain shown in A). C) Multiple boundary traces for the same domain as in A) at four separate times, illustrating fluctuating nature of domain boundary. Radius shown is a deviation from the average.

Spectral analysis of the resulting trace was performed as previously described(*2, 13, 17-19*). The mode powers ζ_n^2 (in units of μm^2) were determined through fast Fourier transform (FFT) of the individual traces on a frame-by-frame basis and then frame-averaged for each domain. Specifically, the radial deviation $\Delta R(\theta) = R(\theta) - <R(\theta)>$

(see Figure 3.4C), where $<R(\theta)>$ is the average radius, was Fourier transformed. Note that this average radius is not the same as the equivalent radius R_0 if the domain is fluctuating(*17*). Esposito et al. have previously discussed the influence of total frame number included in subsequent analysis for the example of phase-separated bilayers, in which there was no measurable dipole density difference(*17*). The accurate determination of non-zero dipolar effects in the monolayer system here under study requires us to obtain average mode powers with high statistical significance. We therefore determined mode powers from averaging FFT data for 1000 frames per domain. An example of averaged mode powers as a function of mode number is given in Figure 3.1. Note that, contrary to bilayer spectra, a significant upward deviation from the 1/3 slope discussed above is observed, confirming the findings of Goldstein and Jackson(*13*).

The set of unitless ratios β_n / β_2 was then fit to the experimentally determined mode power ratios $\langle \zeta_2^2 \rangle / \langle \zeta_n^2 \rangle$ by varying the single fit parameter N_B (Figure 3.1). This procedure was repeated for all potentially resolvable mode sets $[n] = [2,...,n_{max}]$, where n_{max} ranged from 3 to 25, resulting in 23 different values of N_B. These N_B values were plotted as a function of n_{max}, (see Figure 3.5) and the largest mode set prior to a drop-off in the magnitude of N_B was taken to include only the well-resolved modes for that domain (Figure 3.1B). This mode set $[n]^* = [2,...,n_{max}^*]$ and its corresponding N_B value were used in all subsequent analyses. The range of modes included for analysis is indicated by filled symbols in Figure 3.1, as opposed to open ones that indicate excluded data points, and is further indicated by an arrow in Figure 3.5. The rationale for this analysis procedure is the fact that mode powers associated with higher mode numbers $n >$

n^*_{max} will be increasingly distorted through the effects of image pixelization, optical resolution limit, and averaging of domain motion due to finite frame acquisition times(*17*). Additionally, mode sets that are too small do not contain enough data points to yield sufficiently accurate N_B values (Figure 3.1B, open symbols on the lefthand side). The maximum number of resolvable modes depends on the size of fluctuation amplitudes: larger domains at higher pressures have larger amplitudes.
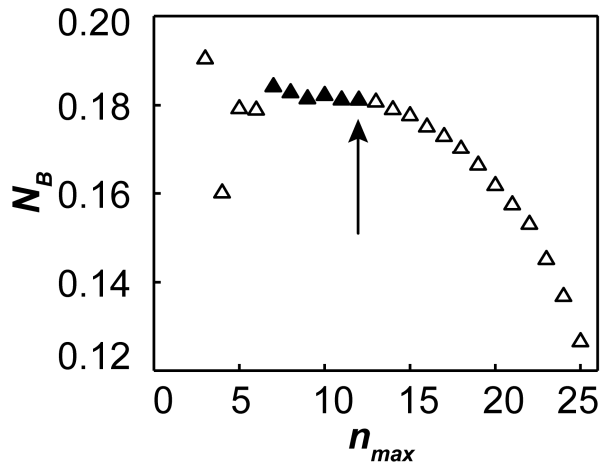
Figure 3.5: Fit parameter N_B for the domain analyzed in Figure 3.1 as a function of mode set $[n] = [2,...,n_{max}]$ considered. The largest set $[n]^* = [2,...,n^*_{max}]$ is indicated with an arrow. Closed triangles indicate sets that include sufficient modes to minimize variational noise, but still exclude the higher modes which are more strongly distorted by aliasing and imaging noise.

With both $[n]^*$ and N_B determined for each individual domain, the mode powers $\langle \varsigma_n^2 \rangle$ were plotted against $1/\beta_n$ (Figure 3.6) and a least-squares linear fit to the form

$y = mx$, with a slope, m, equal to $k_B T R_0 / \pi \gamma$ (Equation 3.9), yielded the line tension. Small values of $1/\beta_n$, referring to large mode numbers ($n > n^*_{max}$) showed a progressive upward deviation from the expected linear relation (see open symbols in the inset of Figure 3.6) and were not included in the analysis.
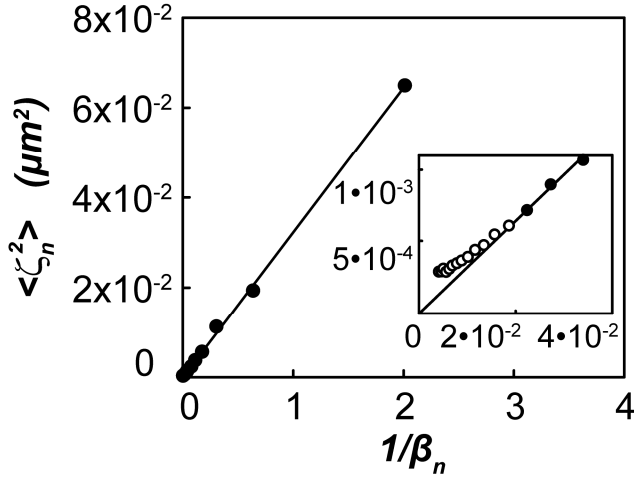
Figure 3.6: Mode powers $\langle \zeta_n^2 \rangle$ plotted vs $\langle \zeta_n^2 \rangle$ for the same domain shown in Figure 3.1. All well-resolved modes (closed circles) follow the linear prediction of Equation 3.9, while the higher numbered, less-resolved modes (open circles, inset) deviate and are excluded from analysis. The slope of the fit line is used to determine the line tension.

Finally, the dipole density difference μ was obtained from the Bond number N_B via $N_B = 2\mu^2 / \gamma$. Approximately 10 domains at each pressure and composition were analyzed to obtain average values of γ and μ^2 (typically for mode power analysis of the first 1000 frames in an image sequence only, except in discussion of photobleaching effects).

For the alternative hydrodynamic mode-amplitude decay theory, the images collected of a single domain needed to be continuously collected at a regular time interval. The images were spectrally analyzed as before to obtain (now time-dependent) sequences of mode amplitudes. Time autocorrelating each mode sequence resulted in the functions $g_n(t) = \left\langle \Delta|\zeta_n(t)|^2 \times \Delta|\zeta_n(0)|^2 \right\rangle$, where $\Delta|\zeta_n(t)|^2 = |\zeta_n(t)|^2 - \left\langle |\zeta_n|^2 \right\rangle$ is the difference in the squared amplitude at time t from the mean (time-averaged) squared amplitude. Each time autocorrelation function was fitted with an exponential decay to determine the decay constant τ_n for each mode n. The ratios β_n/β_2 were then fitted to the experimental decay time ratios τ_2/τ_n using the single fit parameter N_B as in Equation 3.12. In principle, following determination of N_B and, therefore, β_n, both the line tension γ and the dipole density difference μ can be calculated, though in practice the approach has proven less reliable (see Chapter 4) than the statistical, time-independent approach outlined above.

Bilayer[e]

Preparation of Giant Unilamellar Vesicles

The bilayers used in this study were all formed as giant unilamellar vesicles (GUVs) using the now-common technique of electroformation, first described by Angelova and Dimitrov(*20*). Lipid mixtures of a desired composition are prepared in chloroform at a total concentration of ~10 mg/mL. Between 50 and 100 uL of solution are spread uniformly over the electrically conductive sides of two indium-tin-oxide-

---

[e] Parts of this chapter are reproduced from previously published work: Heinrich, M. C., Tian, A., Esposito, C., and Baumgart, T. (2010) Dynamic sorting of lipids and proteins in membrane tubes with a moving phase boundary, *Proc. Natl. Acad. Sci. U.S.A. 107*, 7208.

coated glass slides (Delta Technologies Ltd., Stillwater, MN) at a temperature at 60 °C, above the lipid melting temperature. Solvent was further removed by placing the slides under low vacuum for at least 2 hours but frequently more than 12 hours. The slides were then combined with lipid-coated sides facing each other but separated by an electrically-nonconducting silicone spacer (O-ring) filled with sucrose solution of a desired concentration between 100 mM and 1 M. The slides were electrically connected to an AC field (2 V/mm, 5 Hz) and inserted into a heating block at 60 °C for 2 hours. Following electroformation, the resulting vesicle dispersion could be kept at room temperature in the dark for several days without noticeable degradation.

Preparation and Use of Micropipettes

Micropipettes were fashioned from glass capillaries (World Precision Instruments, Inc., Sarasota, FL) that were stretched using a pipette puller (Model P-77, Sutter Instrument Co., San Francisco, CA). For the experimental chamber used in the present microscopy studies, pipettes were pulled such that the taper length was ~ X mm; shorter tapers frequently would be unable to be brought into the microscope field of view, while the lower mechanical rigidity of longer tapers made positioning of the pipette within the chamber more cumbersome. Pipette tips were cut using a microforge at a desired inner diameter in the range of 1-8 μm. Smaller tip diameters were advantageous for aspiration of smaller GUVs or when the vesicle bending stiffness was higher, in which case a smaller projection length could be expected (see Single Component Vesicle Theory below).

Prior to use, a micropipette tip was filled using a MicroFil needle (WPI)

with 0.5 mg/mL bovine serum albumin (BSA) in 1X PBS, which is known to provide a "protein buffer" between the glass pipette and an aspirated vesicle that minimizes irreversible adhesion. The pipette was then filled with solution matching that used in electroformation of the vesicles to be aspirated, thereby lowering any osmotic mismatch. The filled pipette could then be connected to a water reservoir of variable height and (therefore) hydrostatic pressure, monitored by a pressure transducer (Validyne Engineering, Los Angeles, CA); the pipette was always connected to a large positive reservoir pressure, as zero or negative pressure would pull air into the tip, leading to crystallization and clogging. The pipette was mounted on a three-axis motorized micromanipulator system (Luigs and Neumann, Ratingen, Germany) to achieve micrometer-precision control of the pipette within the experimental chamber. Inserting the pipette at a small angle with respect to the lab-frame (and microscope) z-axis (eg, at ~100° when positioning the pipette near the bottom of the chamber, or ~80° when positioning near the top of the chamber) facilitated bringing the pipette tip into the microscope field of view. Once the pipette tip could be visualized, the height of the connected reservoir was lowered until zero pressure across the tip was attained, as determined by watching the flow of small fluorescent particles within the tip. Negative (suction) pressure could then be used to aspirate a vesicle and fix its lateral tension at a desired value (see Single Component Vesicle Theory below).

Single Component Vesicle Theory

A vesicle composed of a single component is the idealized but useful limit of many vesicles typically used in the current literature, and can be applied to vesicles

composed of a mixture of lipids so long as the vesicle is not within or near a miscibility region or critical point on a phase diagram of those lipids. Such a vesicle can be described by several mechanical properties: the lateral membrane tension σ; the area compression/expansivity modulus K_a; the local bending stiffness κ; the Gaussian bending stiffness κ_G; and the non-local bending stiffness $\bar{\kappa}$. With the exception of the membrane tension, these properties are all intrinsic to the membrane and will vary with composition. The tension, however, can be externally regulated through application of either an osmotic or suction pressure difference ΔP, the latter of which is herein employed. Specifically, the vesicle membrane tension is governed by(*21*):

$$\sigma = \frac{\Delta P \cdot R_p}{2(1 - R_p / R_v)} \qquad (3.13)$$

where R_p and R_v are the pipette and vesicle radii, respectively.

In general, increasing the aspiration pressure in the low tension regime would lead to a longer projection length due to the "smoothing out" of the naturally abundant thermal fluctuations on the vesicle surface, often interpreted as an excess area(*22-23*). The degree to which some of the excess area is pulled into the pipette projection is related to the vesicle expansivity modulus via $\sigma = K_a \alpha$, where the excess area $\alpha = (A - A_p)/A$. Measurements of projection length over a range of applied membrane tensions have been used to determine, for example, changes to the excess area by activated transmembrane proteins(*23-24*).

The energy of a bent membrane is given as $F_{bend} = \kappa/2 \int [(C^i - C_s^i) + (C^j - C_s^j)]^2 dA$ where C^i and C^j are the principal curvatures

and C_s^i and C_s^j are the spontaneous curvatures of the membrane. This energy becomes significant at high curvature as in the case of tubular membranes with radii on the order of 10-100 nm. Classical "tether-pulling" experiments have enabled measurements of the bending stiffness by chemically connecting an aspirated GUV to a microsphere (or another handle) and applying an external force to separate the two, typically resulting in the formation of a thin tube of membrane maintaining the connection between them(*25-28*). In general, a relation is established between the controlled radius of such a tube (R_t) and the force necessary to maintain it at a constant length and area: $f_{tube} = 2\pi\kappa / R_t$. The tube radius, in turn, can be adjusted via the aspiration pressure (and, therefore, the membrane tension) of the vesicle: $R_t = \sqrt{\kappa / 2\sigma}$. The combination of these relations gives us(*29*):

$$f_t = 2\pi\sqrt{2\kappa\sigma} \qquad\qquad (3.14)$$

which shows that, when the force on the tube and the membrane tension can be measured, the bending stiffness is readily determined (Figure 3.7C).
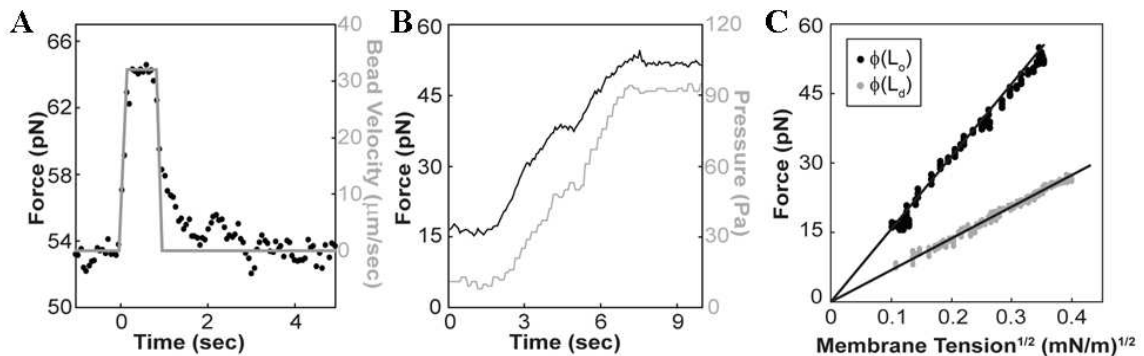
Figure 3.7: *A*) Force response (filled circles) of a homogeneous single-phase aspirated vesicle with a tube that was quickly elongated from 30 to 60 μm at velocity of 31.5

µm/sec. The time-dependent velocity of the trap center is shown as a gray line. Tube force relaxes near to the initial value within two seconds after lateral displacement of the pulling bead was stopped. The vesicle was held at an aspiration pressure of 91 Pa (membrane tension of 0.11 mN/m). Vesicle had a nominal composition of Lo3 as listed in Table 5.1 and Figure 5.1C. Equivalent time dependence was observed for Ld phase membranes (compositions listed in Table 5.1), as well as pure POPC vesicles. *B*) Force response (black line) of the same vesicle and tube as in panel *A*) to rapid changes in aspiration pressure (gray line). Tube force equilibrates after membrane tension changes within < 100 ms for homogeneous vesicles. Similar behavior was observed for homogeneous Ld phase and pure POPC vesicles. *C*) Tube force increases linearly with the square-root of membrane tension in accordance with Equation 3.14, where the slope of a linear fit is used to measure the membrane bending stiffness. Black (gray) circles are measurements on a homogenous vesicle and tube of composition just beyond the Lo (Ld) end of the tie-line shown in Figure 5.1C.

Equation 3.14 is derived from the free energy for a tube of length L and radius R_t which has zero spontaneous curvature. Allowing for nonzero C_s leads to:

$$F = 2\pi RL\left[\frac{1}{2}\kappa\left(\frac{1}{R} - C_s\right)^2 + \sigma\right] - f_{tube}L \qquad (3.15)$$

and, after minimizing the energy with respect to both the radius and length, we obtain a tube force:

$$f_t = 2\pi\sqrt{2\sigma\kappa + \kappa^2 C_s^2} - 2\pi\kappa C_s \qquad (3.16)$$

The free energy (Equation 3.15) can be further modified to include a contribution

61

from the so-called nonlocal bending stiffness $\bar{\kappa}$, which arises from recognition that, were a spherical vesicle transformed entirely into a cylinder, the outer leaflet of the bilayer will have increased in area, while the inner leaflet will have decreased in area. Therefore, a tube pulled from an aspirated vesicle will gradually increase the energy due to expansion/compression of the outer/inner monolayers by an amount proportional to the length of the tube and the intrinsic nonlocal bending stiffness, resulting in a tube force of:

$$f_t = 2\pi\sqrt{2\sigma\kappa + \kappa^2 C_s^{\,2}} - 2\pi\kappa C_s + \frac{\pi\bar{\kappa}}{R_v}L_t \tag{3.17}$$

Values for $\bar{\kappa}$ are typically small enough(*30-31*) that, for tubes shorter than 100 μm, the third term in Equation 3.17 can often be ignored.

Phase-Separated Vesicle Theory

Analytical Mass Transport Model

In Chapter 4, experimental evidence for curvature-driven sorting of lipids in a phase-separated bilayer is presented. A tube pulled from the liquid-ordered (Lo) phase region of the vesicle is observed (via confocal fluorescence microscopy) to nucleate a liquid-disordered (Ld) phase domain at the tube-vesicle neck (Figure 5.1). The nucleated domain proceeds to grow in length (and area) towards the end of the tube, gradually replacing the Lo phase with Ld phase until the entirety of the tube was taken up by the Ld domain. Furthermore, the domain's growth rate as measured by the intra-tube phase boundary velocity was found to decrease with domain elongation. These observations suggest that the non-equilibrium process can be described as a Stefan problem, wherein the Ld phase in the tube presents a (length-dependent) mass transport resistance. Such

systems display parabolic moving boundary behavior (Figure 5.2), frequently encountered in classical physicochemical phenomena involving both heat and mass transfer(*32-33*).

We derived a simple thermodynamic transport model that enables us to explain these dynamic aspects of the findings shown in Figures 4.7 and 4.8. The key features of the model are depicted in Figure 3.8. The vesicle and the Lo phase portion of the tube are assumed to act as thermodynamic reservoirs, thereby fixing the chemical potential of each region to be independent of the (growing) Ld phase tube domain. Note that the chemical potential is presumed to be curvature dependent; this accounts for the energy penalty due to the non-zero bending stiffness of the membrane (see Equation 3.15). It is assumed that a linear chemical potential gradient across the thermodynamic system (here the Ld phase tube) connects both reservoirs(*33*), and that the ternary mixture can be reduced to a quasi-binary mixture; the implications of these assumptions are discussed below. The diffusion potential is defined as the difference in the chemical potentials of the two components α and β in the quasi-binary mixture: $\overline{\mu} = \mu_\alpha - \mu_\beta$ (*34*). In our model, transport is driven by a curvature-dependent diffusion potential difference $\delta\overline{\mu} = \overline{\mu}(\phi_0, C_t) - \overline{\mu}(\phi_0, C_{ves} = 0)$ between both reservoirs (see Fig. 3.7B). Note that the assumption that the Lo phase region of the tube acts as a reservoir leads to a time-independent $\delta\overline{\mu}$.
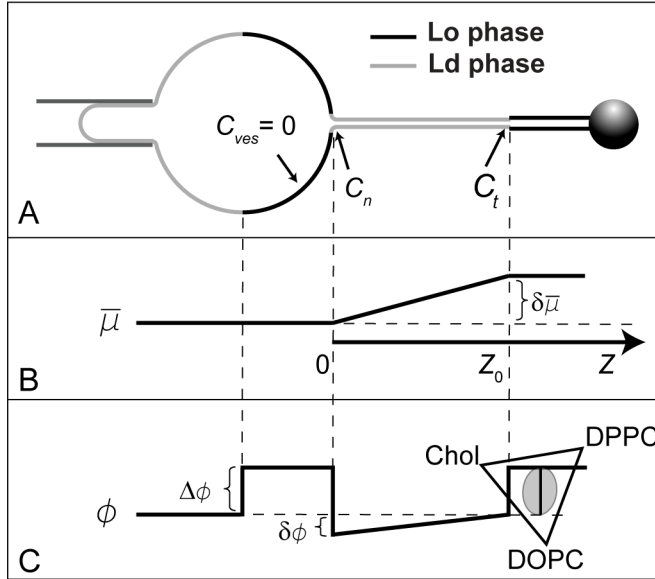
Figure 3.8: Schematic of linear irreversible thermodynamics model. *A*) Vesicle (left-hand side) and Lo phase tube domain (right-hand side) are considered thermodynamic reservoirs with fixed chemical exchange potential $\bar{\mu}$ (B) – where the difference between reservoirs is $\delta\bar{\mu}$ – and fixed composition ϕ (C) – where the maximal composition difference in Ld tube due to curvature is $\delta\phi$. Here, ϕ is defined as the mole fraction of Lo phase lipid in a quasibinary mixture; the width of the phase coexistence region is $\Delta\phi$. Due to membrane curvature, the chemical potential in the right-hand side reservoir is larger compared to the left-hand side reservoir, whereas the composition of the Lo phase in both reservoirs is the same. Linear chemical potential and composition gradients are assumed in the Ld phase connecting both reservoirs. At the intra-tube phase boundary (where the axial coordinate $Z = Z_0$), the curvature is C_t. At the vesicle/tube phase boundary (where $Z = 0$), the curvature is C_n. The vesicle has negligible curvature.

More completely, the diffusion equation for mass transport in the Ld phase tube is

$D_{\alpha\beta}^{L_d} \nabla^2 \overline{\mu} = \partial \overline{\mu} / \partial t$, where $D_{\alpha\beta}^{L_d}$ is a binary inter-diffusion coefficient in the Ld phase. At steady state this relation simplifies to a Laplace equation: $\nabla^2 \overline{\mu} = 0$ (*35*). This steady state relation is integrated along a local spatial coordinate Z of the Ld domain (see Figure 3.8), using two chemical equilibrium boundary conditions (at each end of the Ld phase tube). At the tube neck, $\overline{\mu}^{Ld}\big|_{Z=0} = \overline{\mu}_{eq}^{Lo}$, where $\overline{\mu}_{eq}^{Lo} = \overline{\mu}_{eq}^{Ld}$ is the value of $\overline{\mu}$ in the equilibrated flat reservoir (i.e. within the vesicle where $\overline{\mu} = \overline{\mu}(\phi_0, C_{ves} = 0)$; C_i is the curvature in membrane region i and ϕ_0 indicates the composition (mole fraction) of the vesicle reservoir; see Figure 3.8C). It is thus assumed that the value of $\overline{\mu}$ at the tube neck with curvature C_n is equal to the value in the flat reservoir(*34*). The second boundary condition is $\overline{\mu}^{Ld}\big|_{Z=Z_0} = \overline{\mu}^{Lo}(\phi_0, C_t)$, where C_t is the curvature at the intra-tube phase boundary at position Z_0 (Figure 3.8A). Here, composition is fixed at ϕ_0 because we assume that the tube phase transition occurs at the composition defined by the binodal line of the phase diagram, see Figure 3.7C. This simplifying assumption implies that the Ld / Lo phase diagram is not modified by membrane curvature (see below for further discussion of this aspect).

After integration, $\overline{\mu}(Z) = \delta\overline{\mu} \cdot Z / Z_0 + \overline{\mu}_{eq}$ for $0 < Z < Z0$, where $\delta\overline{\mu} = \overline{\mu}(\phi_0, C_t)$. We evaluate the quantity $\delta\overline{\mu}$ from a Taylor expansion(*34*), considering absence of an intrinsic membrane curvature preference (i.e. spontaneous curvature, causing the first order term in an expansion in curvature to disappear(*34*)):

$$\delta\overline{\mu}\big|_{Z_0} = \frac{1}{2}\left(\frac{\partial^2 \overline{\mu}}{\partial C^2}\right)_0 C_t^2 = \frac{1}{2\rho}\left(\frac{\partial \kappa}{\partial \phi_\alpha}\right)_0 C_t^2 \qquad (3.18)$$

where the index "0" of the partial differentials indicates evaluation of the partial derivatives for the flat state of the membrane(*34*). The domain growth in our problem therefore is assumed to be caused by a thermodynamic driving force to lipid sorting due to the composition dependence of the bending stiffness in Equation 3.19(*34*). Assuming the composition variation along the Ld phase tube to be small, and accordingly the curvature change along the Ld phase tube to be small, we have an approximately constant lateral (mean-) tension σ_{Ld} in the Ld phase domain of the tube: $\sigma_{Ld} = \kappa_0^{Ld} C^2 / 2$.

Meanwhile, the domain boundary velocity $\upsilon = dZ_0 / dt$ is related to mass transport via the continuity relation $\upsilon \rho \Delta \phi_\varepsilon = M_{Ld} \nabla \overline{\mu}$ (*35*), where ρ is an area density (which for simplicity we assume to be equal in all phases), M is a mobility (an Onsager transport coefficient) in the Ld phase, and $\Delta \phi_\varepsilon = \phi_{Lo} R_{Lo} / R_{Ld} - \phi_{Ld}$; $\phi_{Lo} - \phi_{Ld}$ is the width of the miscibility gap (Figure 3.8C), and R_i is the tube radius of phase *i*. Note that the ratio of tube radii is related to bending stiffnesses through $R_{Lo} / R_{Ld} = \kappa_{Lo} / \kappa_{Ld} \equiv \varepsilon$; the bending stiffness ratio ε is a material property of a phase-separated tube and does not depend on curvature.

Integration of the continuity equation above (assuming a time-independent curvature C_t at the intra-tube phase boundary to approximately be equivalent to the inverse Ld tube radius C) leads to:

$$Z_0^2 = t \frac{M_{Ld}}{\rho^2 \Delta \phi_\varepsilon} \left(\frac{\partial \kappa_{Ld}^0}{\partial \phi_\alpha} \right)_0 \frac{\sigma_{Ld}}{\kappa_{Ld}^0} = tAC^2 \qquad (3.19)$$

Note that Equation 3.19 predicts that the domain length will grow at a rate proportional to the square-root of time *t*, matching our parabolic expectation for a Stefan problem.

Furthermore, the growth rate is also predicted to increase with the (Ld phase) tube curvature, and therefore the membrane tension. Both of these predictions are examined and verified in Chapter 4.

The quantity A summarizes the time- and curvature-independent parameters on the left-hand side of Equation 3.19. It contains the composition dependence of the Ld phase bending stiffness, assumed here to underlie curvature-mediated sorting(*34, 36*). We note that accounting for nonlinear concentration gradients affects the numerical value of A, but does not otherwise influence the time dependence of Z_0 in this model(*37*). The quantity AC^2 can be interpreted as a curvature-dependent interdiffusion coefficient. It is worthwhile to again mention that Equation 3.19 is based on numerous simplifications required to obtain an analytically tractable model. These include (i) neglect of area density (ρ) difference between Lo and Ld phases, (ii) assumed absence of friction effects contributed by water (and membrane area) transport among tube and vesicle (see Chapter 4 for discussion), (iii) spatially fixed vesicle/tether phase boundary, (iv) assumption of time-independent tube radii of Lo and Ld phases, and (v) absence of concentration gradient in tube Lo phase (see Chapter 4 for discussion). We investigated (iii) and (iv) through numerical simulations of comparable tube shapes, the details of which are discussed in the following section.

We note that the binary description used here to reduce analytical complexity eliminates a variety of phenomena such as reverse osmosis, inverse osmosis, and blocked osmosis, which are common in ternary mixtures(*38*). Because the Onsager reciprocity relations become relevant only for mixtures with three or more components(*38*), any of the above mentioned phenomena are absent in binary mixtures.

Numerical Simulation of Tube Shapes

The formalism described below is adapted from a theoretical scheme developed by Juelicher and Lipowsky(*39-40*). The catenoid shape was parameterized by means of a non-dimensionalized radius r and tangent angle to the shape ψ, as a function of arclength of the shape s, see inset of Figure 5.5A (*41*). The arclength s was measured from the catenoid edge, and the angle ψ was measured relative to the radial coordinate axis. We solved the resulting system of first order differential equations with the boundary value problem (bvp) solver *bvp4c* of Matlab (The Mathworks, Inc., Natick, MA). The bvp solver requires fixed integration intervals. In order to vary the total arclength of the shape, the equations were therefore re-parameterized using the integration variable S $\in [0,\dots,\pi]$ such that $s(S = 0) = s_0 = 0$ at one end of the shape, and $s(S = \pi) = s_{end}$ at the other end(7, 9). For the phase-separated tube the two phase boundaries are localized at $s_1 = s(S_1^*)$ and $s_2 = s(S_2^*)$. In the following, derivatives with respect to s are indicated by an apostrophe, and derivatives with respect to S are indicated by a dot. The choice of $\dot{s} = \sin(S)/r$ fixes the total area of the shape to a value corresponding to the area of a sphere with unit radius(*42*), since:

$$A = 2\pi \int_{s_0}^{s_{end}} r\,ds = 2\pi \int_0^\pi \sin(S)\,dS = 4\pi \tag{3.20}$$

Similarly, fixing values S_1^* and S_2^* while varying the shape ensured constant area fractions of coexisting phases. The free energy of the membrane is given, using indices i for coexisting phases(*40, 43*):

$$F_i = \frac{\kappa_i}{2} \int (C_1 + C_2)^2 \, dA + \sigma_i \int dA + p \int dV + \frac{\gamma}{2\pi} \int (r' - \cos\psi) \, ds$$

$$- f \int dL + 2\pi T r(s_i) \tag{3.21}$$

Here, κ is the bending stiffness, C_1 and C_2 are meridianal and parallel curvatures of the axially symmetric shape, and V and L are volume and length of the shape, respectively. Furthermore, σ, p, and f are Lagrange multipliers fixing area, volume, and length of the shape, respectively. T is an additional Lagrange multiplier corresponding to the line tension at a phase boundary at position s_i. The quantity γ is also a Lagrange multiplier. Its mechanical meaning is the projection of the transverse shear along a direction orthogonal to the symmetry axis(*44*). Geometrically, it ensures the constraint $r' = \cos(\psi)$ (*41*). For axially symmetric shapes, we have $C_1 = \psi'$ and $C_2 = \sin(\psi)/r$. We furthermore have:

$$dA = 2\pi r \, ds \qquad dV = \pi r^2 \sin(\psi) \, ds \qquad dL = \sin(\psi) \, ds \tag{3.22}$$

The variation of the shape free energy in terms of the variables ψ, ψ', r, r', and γ can be expressed in terms of a Lagrangian defined as (mechanical variables are here divided by the bending stiffness)(*43*)

$$L_i = \frac{r}{2} \left(\psi' + \frac{\sin\psi}{r} \right)^2 + \sigma_i r + \frac{p r^2}{2} \sin\psi + \gamma(r' - \cos\psi) - \frac{f}{2\pi} \sin\psi \tag{3.23}$$

such that $F_i = 2\pi \int L_i \, ds + 2\pi T r(s_i)$. Therefore, for stationary shapes:

$$\frac{\delta F_i}{2\pi} = \int \left[\left(\frac{\partial L_i}{\partial \psi} \delta\psi + \frac{\partial L_i}{\partial \psi'} \delta\psi' \right) + \left(\frac{\partial L_i}{\partial r} \delta r + \frac{\partial L_i}{\partial r'} \delta r' \right) + \frac{\partial L_i}{\partial \gamma} \delta\gamma \right] ds + T \delta r(s_i) = 0 \tag{3.24}$$

Integrating the bracketed terms in Eq. S5 by parts yields two Euler-Lagrange equations for each domain i plus two boundary conditions at each phase boundary.

From the Euler-Lagrange equations one obtains three first order ordinary differential equations (DEQs) for the first domain (which is an Lo phase domain), after dividing by the bending stiffness of the Lo phase:

$$\psi' \equiv U \tag{3.25}$$

$$U' = -\frac{\psi \cos\psi}{r} + \frac{\sin\psi \cos\psi}{r^2} + \frac{pr \cos\psi}{2} + \frac{\gamma \sin\psi}{r} - \frac{f \cos\psi}{2\pi r} \tag{3.26}$$

$$\gamma' = \frac{U^2}{2} - \frac{\sin^2\psi}{2r^2} + pr \sin\psi + \sigma_1 \tag{3.27}$$

For the second domain, i.e. the Ld domain with a lower bending stiffness, the equivalents to Equations 3.26 and 3.27 are:

$$U' = -\frac{\psi' \cos\psi}{r} + \frac{\sin\psi \cos\psi}{r^2} + \frac{\varepsilon pr \cos\psi}{2} + \frac{\varepsilon\gamma \sin\psi}{r} - \frac{\varepsilon f \cos\psi}{2\pi r} \tag{3.28}$$

$$\gamma' = \frac{U^2}{2} - \frac{\sin^2\psi}{2r^2\varepsilon} + pr \sin\psi + \sigma_2 \tag{3.29}$$

where $\varepsilon = \kappa_{Lo}/\kappa_{Ld}$ is the ratio of bending stiffness values in Lo and Ld phases. For the third domain, the shape equations are essentially those of Equations 3.25-3.27 but allowing for a (potentially different) membrane tension σ_3. For each domain, we use the following three additional DEQs:

$$r' = \cos\psi \tag{3.30}$$

$$z' = -\sin\psi \tag{3.31}$$

$$\sigma'_i = 0 \tag{3.32}$$

Equation 3.31 is an auxiliary DEQ that is used to find the z-coordinate of a point on the shape, while Equation 3.32 ensures that the lateral tension in each domain is spatially constant. The system of 18 DEQs (six for each domain) is integrated using the fixed

integration variable $S \in [0,...,\pi]$ instead of the arclength s of the deformed shape. This requires that the integration limits be expressed for each domain as a function of S: for the first domain, $S_1 = SS_1^*/\pi$; for the second domain, $S_2 = S_2^* - S(S_2^* - S_1^*)/\pi$; and, for the third domain, $S_3 = \pi - S(\pi - S_2^*)/\pi$. It follows that $ds_1 = dS(S_1^*/\pi)\sin S_1/r$, $ds_2 = -dS((S_2^* - S_1^*)/\pi)\sin S_2/r$, and $ds_3 = -dS((\pi - S_2^*)/\pi)\sin S_3/r$ for the first through third domain, respectively.

The system of 18 DEQs requires 18 boundary conditions. Six of these are defined at the two ends of the shape. At the catenoid edge, where $s = s_0 = 0$, we require:

$$U(s_0) + \frac{\sin \psi(s_0)}{r(s_0)} \tag{3.33}$$

$$\sigma_1 - \sigma_{catenoid} = 0 \tag{3.34}$$

$$z(s_0) = 0 \tag{3.35}$$

Equation 3.33 sets the mean curvature at the catenoid edge to zero (free hinge boundary condition)(45), and Equation 3.34 fixes the lateral tension of the catenoid to a value of choice, as is achievable with aspirated GUVs. At the tip of the tube where $s = s_{end}$, we enforce (neglecting normal pressure difference as appropriate for a thin tube(46)):

$$\frac{1}{2r(s_{end})^2} + \sigma_3 - \frac{f}{2\pi r(s_{end})} = 0 \tag{3.36}$$

$$\psi(s_{end}) - \pi/2 = 0 \tag{3.37}$$

$$\gamma(s_{end}) = 0 \tag{3.38}$$

Equations 3.36-3.38 are a consequence of assuming perfectly cylindrical geometry at the tube tip. Equation 3.36 is the mechanical force balance (mechanical quantities are

71

divided by the bending stiffness), Equation 3.37 orients the tangent angle appropriately for an axially symmetric cylinder, and Equation 3.38 follows from the fact that the transverse shear projected into a direction orthogonal to the symmetry axis must be zero.

The Hamiltonian of the shape, $H_i = -L_i + \psi' \partial L_i / \partial \psi' + r' \partial L_i / \partial r'$, is therefore:

$$H_i = \frac{r}{2}\left(U^2 - \frac{\sin^2 \psi}{r^2}\right) - \frac{pr^2}{2}\sin \psi - \sigma_i r + \gamma \cos \psi + \frac{f \sin \psi}{2\pi} \tag{3.39}$$

Accounting for cylindrical geometry at the membrane edge, neglecting the pressure term, and inserting Equations 3.36 and 3.37 shows that $H = 0$ at the tube tip. The Hamiltonian is furthermore conserved, and therefore $H = 0$ all along the shape.

An additional six boundary conditions connect the shape at each of the two phase boundaries. For each phase boundary, we have three conditions requiring continuity of the shape parameters, i.e. angle ψ, radius r, and coordinate z must have the same values immediately before and after each phase boundary. The remaining three phase boundary conditions mechanical jump conditions. They are obtained from the two boundary terms of the Euler-Lagrange equations and they read (indices indicate value immediately before and after the respective phase boundary):

$$\gamma_1 - \gamma_2 - + T = 0, \qquad \gamma_2 - \gamma_3 - + T = 0 \tag{3.39}$$

as well as

$$U_1 + \frac{\sin \psi}{r} - \frac{1}{\varepsilon}\left(U_2 + \frac{\sin \psi}{r}\right) - \xi \frac{\sin \psi}{r} = 0 \tag{3.40}$$

at the first boundary, whereas

$$\frac{1}{\varepsilon}\left(U_2 + \frac{\sin \psi}{r}\right) - \left(U_3 + \frac{\sin \psi}{r}\right) + \xi \frac{\sin \psi}{r} = 0 \tag{3.41}$$

72

at the second boundary. Here, $\xi = (\kappa_G^{Ld} - \kappa_G^{Lo})/\kappa^{Lo}$ is the Gaussian bending stiffness difference between the Lo and Ld phases, non-dimensionalized by dividing by the Lo phase bending stiffness(*40, 47*). Equation 3.39 requires that the jump across the phase boundary of transverse shear projected along the parallel is equal to the line tension *T*. Equations 3.40 and 3.41 express the fact that the bending moments have to be continuous in passing the phase boundaries.

The remaining set of boundary conditions is obtained from the requirement that the Hamiltonian is continuous across the phase boundaries, leading to:

$$\left(\frac{U_1^2}{2} - \frac{\sin^2 \psi}{2r^2} - \sigma_1 \right) - \left(\frac{U_2^2}{2\varepsilon} - \frac{\sin^2 \psi}{2\varepsilon r^2} - \sigma_2 \right) - \frac{T}{r} \cos\psi = 0 \tag{3.42}$$

$$\left(\frac{U_2^2}{2\varepsilon} - \frac{\sin^2 \psi}{2\varepsilon r^2} - \sigma_2 \right) - \left(\frac{U_3^2}{2} - \frac{\sin^2 \psi}{2r^2} - \sigma_3 \right) - \frac{T}{r} \cos\psi = 0 \tag{3.43}$$

for the first and second phase boundaries, respectively. Equations 3.42 and 3.43 relate the jumps in lateral tension across the phase boundary to the jumps in curvature.

Since both the pressure *p* and Gaussian bending stiffness difference ζ had small effects on our resulting tube shapes, these parameters were set to zero for all simulations performed. By requiring a tube of specified length, we mandate a 19th boundary condition which enables us to determine the pulling force *f* as an eigenvalue.

References

1.   Kates, M. (1986) *Techniques of Lipidology, 2nd ed*, Elsevier Science Publishers, Amsterdam.
2.   Goldstein, R. E., and Jackson, D. P. (1994) Domain shape relaxation and the spectrum of thermal fluctuations in Langmuir monolayers, *J. Phys. Chem. 98*, 9626.
3.   Keller, D., Korb, J. P., and McConnell, H. M. (1987) Theory of shape transitions in two-dimensional phospholipid domains, *J. Phys. Chem. 91*,

6417.

4. Subramaniam, S., and McConnell, H. M. (1987) Critical mixing in monolayer mixtures of phospholipid and cholesterol, *J. Phys. Chem. 91*, 1715.

5. Seul, M., and Sammon, M. J. (1990) Competing interactions and domain-shape instabilities in a monomolecular film at an air-water interface, *J. Phys. Rev. Lett. 64*, 4728.

6. McConnell, H. M. (1990) Harmonic shape transitions in lipid monolayer domains, *J. Phys. Chem. 94*, 4728.

7. Deutch, J. M., and Low, F. E. (1992) Theory of shape transitions of two-dimensional domains, *J. Phys. Chem. 96*, 7097.

8. Stone, H. A., and Mcconnell, H. M. (1995) Hydrodynamics of Quantized Shape Transitions of Lipid Domains, *Proceedings of the Royal Society of London Series a-Mathematical and Physical Sciences 448*, 97.

9. Mcconnell, H. M. (1990) Harmonic Shape Transitions in Lipid Monolayer Domains, *J Phys Chem-Us 94*, 4728.

10. Deutch, J. M., and Low, F. E. (1992) Theory of Shape Transitions of 2-Dimensional Domains, *Journal of Physical Chemistry 96*, 7097.

11. Lee, K. Y. C., and Mcconnell, H. M. (1993) Quantized Symmetry of Liquid Monolayer Domains, *J Phys Chem-Us 97*, 9532.

12. Langer S.A., Goldstein R.E., and Jackson D.P. (1992) Dynamics of labyrinthine pattern formation in magnetic films, *Physical Review A 46*, 4894

13. Goldstein, R. E., and Jackson, D. P. (1994) Domain Shape Relaxation and the Spectrum of Thermal Fluctuations in Langmuir Monolayers, *J Phys Chem-Us 98*, 9626.

14. Lubensky, D. K., and Goldstein, R. E. (1996) Hydrodynamics of monolayer domains at the air-water interface, *Physics of Fluids 8*, 843.

15. Esposito, C., Tian, A., Melamed, S., Johnson, C., Tee, S. Y., and Baumgart, T. (2007) Flicker spectroscopy of thermal lipid bilayer domain boundary fluctuations, *Biophys. J. 93*, 3169.

16. Benvegnu, D. J., and McConnell, H. M. (1992) Line tension between liquid domains in lipid monolayers, *J. Phys. Chem. 96*, 6820.

17. Esposito, C., Tian, A., Melamed, S., Johnson, C., Tee, S. Y., and Baumgart, T. (2007) Flicker spectroscopy of thermal lipid bilayer domain boundary fluctuations, *Biophysical Journal 93*, 3169.

18. Seul, M., and Sammon, M. J. (1990) Competing Interactions and Domain-Shape Instabilities in a Monomolecular Film at an Air-Water Interface, *Physical Review Letters 64*, 1903

19. Seul, M., Sammon, M. J., and Monar, L. R. (1991) Imaging of Fluctuating Domain Shapes - Methods of Image-Analysis and Their Implementation in a Personal Computing Environment, *Rev Sci Instrum 62*, 784.

20. Angelova, M. I., and Dimitrov, D. S. (1986) Liposome electroformation, *Faraday Discuss. Chem. Soc. 81*, 303.

21. Waugh, R. E., and Evans, E. A. (1979) Thermoelasticity of red blood cell membrane, *Biophys .J. 26*, 115.

22. Evans, E. A., and Needham, D. (1987) Physical properties of surfactant bilayer membranes: Thermal transitions, elasticity, rigidity, cohesion, and colloidal

interactions, *J. Phys. Chem. 91*, 4219.

23. Manneville, J. B., Bassereau, P., Ramaswamy, S., and Prost, J. (2001) Active membrane fluctuations studied by micropipet aspiration, *Phys. Rev. E 64*, 021908.

24. Manneville, J. B., Bassereau, P., Levy, D., and Prost, J. (1998) Activity of transmembrane proteins induces magnification of shape fluctuations of lipid membranes, *Phys. Rev. Lett. 82*, 4356.

25. Hochmuth, R. M., Wiles, H. C., Evans, E. A., and McCown, J. T. (1982) Extensional flow of erythrocyte membrane from cell body to elastic tether. II. Experiment, *Biophys. J. 39*, 83.

26. Hochmuth, R. M., and Evans, E. A. (1982) Extensional flow of erythrocyte membrane from cell body to elastic tether. I. Analysis, *Biophys. J. 39*, 71.

27. Bo, L., and Waugh, R. E. (1989) Determination of bilayer membrane bending stiffness by tether formation from giant, thin-walled vesicles, *Biophys .J. 55*, 509.

28. Borghi, N., Rossier, O., and Brochard-Wyart, F. (2003) Hydrodynamic extrusion of tubes from giant vesicles, *Europhys. Lett. 64*, 837.

29. Derenyi, I., Julicher, F., and Prost, J. (2002) Formation and Interaction of Membrane Tubes, *Phys. Rev. Lett. 23*, 238101.

30. Waugh, R. E., Song, J., Svetina, S., and Zeks, B. (1992) Local and nonlocal curvature elasticity in bilayer membranes by tether formation from lecithin vesicles, *Biophys .J. 61*, 974.

31. Yeung, A. (1994) Mechanics of inter-monolayer coupling in fluid surfactant bilayers, in *Dept. of Physics*, University of British Columbia, Vancouver.

32. Stefan, J. (1891) Ueber die theorie der eisbildung, insbesonder uber die eisbildung im polarmeere, *Ann. Phys. 278*, 269.

33. De Groot, S. R., and Mazur, P. (2963) *Non-Equilibrium Thermodynamics*, North-Holland Publishing Company, Amsterdam.

34. Tian, A., and Baumgart, T. (2009) Sorting of Lipids and Proteins in Membrane Curvature Gradients, *Biophys .J. 96*, 2676.

35. Langer, J. S. (1980) Instabilities and pattern formation in crystal growth, *Rev. Mod. Phys. 52*, 1.

36. Sorre, B., Callan-Jones, A., Manneville, J. B., Nassoy, P., Joanny, J. F., Prost, J., Goud, B., and Bassereau, P. (2009) Curvature-driven lipid sorting needs proximity to a demixing point and is aided by proteins, *Proc. Natl. Acad. Sci. U.S.A. 106*, 5622.

37. Crank, J. (1984) *Free and moving boundary problems*, Oxford University Press, Oxford.

38. Taylor, R., and Krishna, R. (1993) *Multicomponent Mass Transfer*, John Wiley and Sons, Inc., New York.

39. Julicher, F., and Lipowsky, R. (1993) Domain-induced budding of vesicles, *Phys. Rev. Lett. 70*, 2964.

40. Julicher, F., and Lipowsky, R. (1996) Shape transformations of vesicles with intramembrane domains, *Phys. Rev. E 53*, 2670.

41. Seifert, U., Berndl, K., and Lipowsky, R. (1991) Shape transformation of vesicles: Phase diagram for spontaneous-curvature and bilayer-coupling models, *Phys. Rev. A 44*, 1182.

42. Jenkins, J. T. (1976) Static equilibrium configurations of a model red blood

cell, *J. Math. Bio. 4*, 149.

43. Bozic, B., Svetina, S., and Zeks, B. (1997) Theoretical analysis of the formation of membrane microtubes on axially strained vesicles, *Phys. Rev. E 55*, 5834.
44. Umeda, T., Nakajima, H., and Hotani, H. (1998) Theoretical analysis of shape transformations of liposomes caused by microtubule assembly, *J. Phys. Soc. Jpn. 67*, 682.
45. Allain, J. M., Storm, C., Roux, A., Amar, M. B., and Joanny, J. F. (2004) Fission of a multiphase membrane tube, *Phys. Rev. Lett. 93*, 158104.
46. Evans, E. A., and Yeung, A. (1994) Hidden dynamics in rapid changes of bilayer shape, *Chem. Phys. Lipids 73*, 39.
47. Baumgart, T., Das, S., Webb, W. W., and Jenkins, J. T. (2005) Membrane elasticity in giant vesicles with fluid phase coexistence, *Biophys. J. 89*, 1067.

Chapter 4: Lipid Monolayer Phase Behavior

Surface Pressure Dependence and Critical Phenomena Results[f]

Critical Exponents

Mixed monolayer membranes of DMPC and DChol at the critical composition (70% DMPC / 30% DChol), were imaged at a range of surface pressures decreasing from the critical pressure (10.1 mN/m) down to a pressure of 6.5 mN/m. This critical pressure is in good agreement with published values[1]. Image frames were analyzed to extract the bare line tension γ and dipole density difference μ as a function of surface pressure as described in the Capillary Wave Theory section of Chapter 3. Both γ and μ increased from 0.22 to 0.64 pN and 0.44 to 0.68 D/100 Å^2, respectively, as the surface pressure was decreased from 9 to 6.5 mN/m (Figure 4.1A). The pressure dependence of line tension and dipole density difference, near the critical point, can be expressed as a function of the critical exponents d and β, respectively[2-3]. These relations are $\gamma = m\pi_r^d$, and $\mu = n\pi_r^{2\beta}$, where m and n are adjustable parameters and the reduced surface pressure $\pi_r = \pi_c - \pi$, i.e. π_r is the deviation of the film pressure from the critical pressure π_c. For the critical composition, the exponents for the dependence of γ and μ^2 on reduced surface pressure were 0.9 ± 0.2 and 0.35 ± 0.09, respectively (see Figure 4.3C). These values compare favorably with those assumed by Benvegnu and McConnell (1.0 and 0.33, respectively). The largest contribution to the uncertainty in our critical exponents stems from the uncertainty of the measurement of π_c ($\pm$ 0.5 mN).

---

[f] Parts of this chapter are reproduced from previously published work: Heinrich, M. C., Levental, I., Gelman, H., Janmey, P. A., and Baumgart, T. (2008) Critical exponents for line tension and dipole density difference from lipid monolayer domain boundary fluctuations, *J. Phys. Chem. B 112*, 8063.
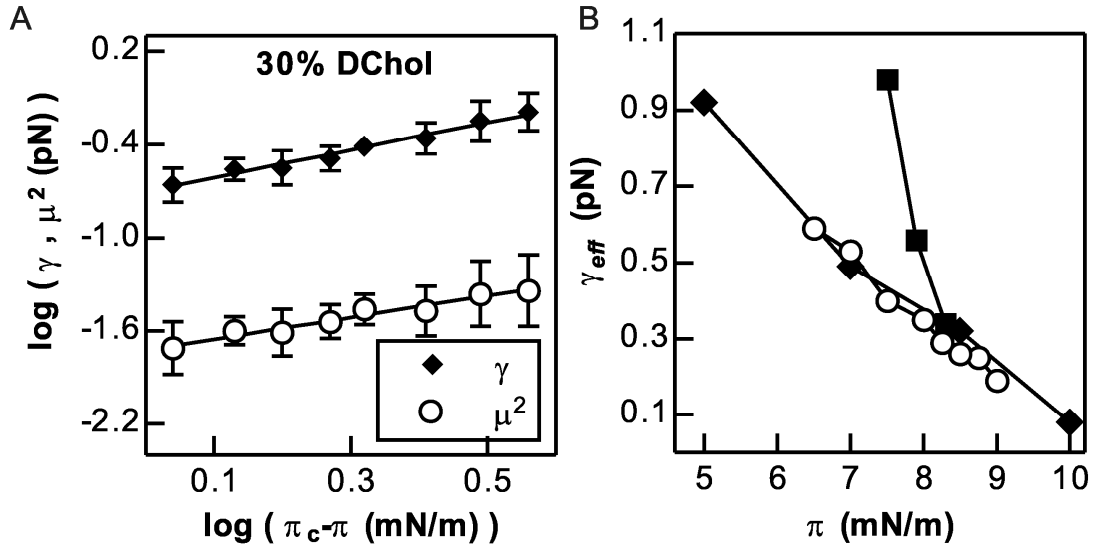
Figure 4.1: A) Line tension and dipole density differences measured for the critical composition (30% DChol and 70% DMPC) both depend logarithmically on the reduced surface pressure $\pi_c - \pi$, eg, the distance from the critical pressure π_c. B) Effective line tensions $\gamma_{eff} = \gamma - \mu^2$ are calculated from our data (open circles) as a function of surface pressure. Previous work was limited to measurements of effective line tension and is here reproduced for comparison: Benvegnu and McConnell(*2*) (filled diamonds) and Stottrup et al(*4*) (filled squares).

Comparison to Previous Estimates of Effective Line Tension

The effective line tensions obtained from the relation $\gamma_{eff} = \gamma - \mu^2$ measured here are in excellent agreement with those previously derived from the recovery of domain shape following external distortion (see Figure 4.1B and Ref. (*5*)). Note however, that the discussion in Ref. (*5*) indicates a small uncertainty in their measured values due to approximations inherent in their analysis approach. Hence the remarkable agreement of our findings with those of Ref. (*5*) could be somewhat fortuitous.

78

Additionally, γ and μ measured by Goldstein and Jackson from a preliminary data set near the critical pressure match the trends observed with our data (quantitative differences could be due to their data being taken closer to the critical point(6)). A recent capillary wave theory quantification of γ_{eff} (4) measured a very similar line tension at high surface pressure (8.3 mN/m), although a significantly different surface pressure dependence (see Figure 4.1B) of γ was observed.

Effects of Photobleaching and Domain Size

Measurement of 2000 consecutive frames for each domain allowed us to quantify the effect of photo-induced oxidation on the measured parameters of γ and μ. Both parameters were reduced by ~10%, which was not a statistically significant amount, when calculated from the third and fourth sets of 500 frames (<10 secs) of the sequences compared to the first or second (Figure 4.2A). This reduction was associated with significant photobleaching and might be suggestive of photo-induced generation of line active oxidation products. This observation is in accordance with the observed reduction of line tension by photo-induced production of cholestenone in a similar mixed monolayer(7). Note, however, that since both γ and μ are affected by photobleaching products, these appear to have an effect not only on phase boundary properties, but also on the bulk properties of the coexisting domains.
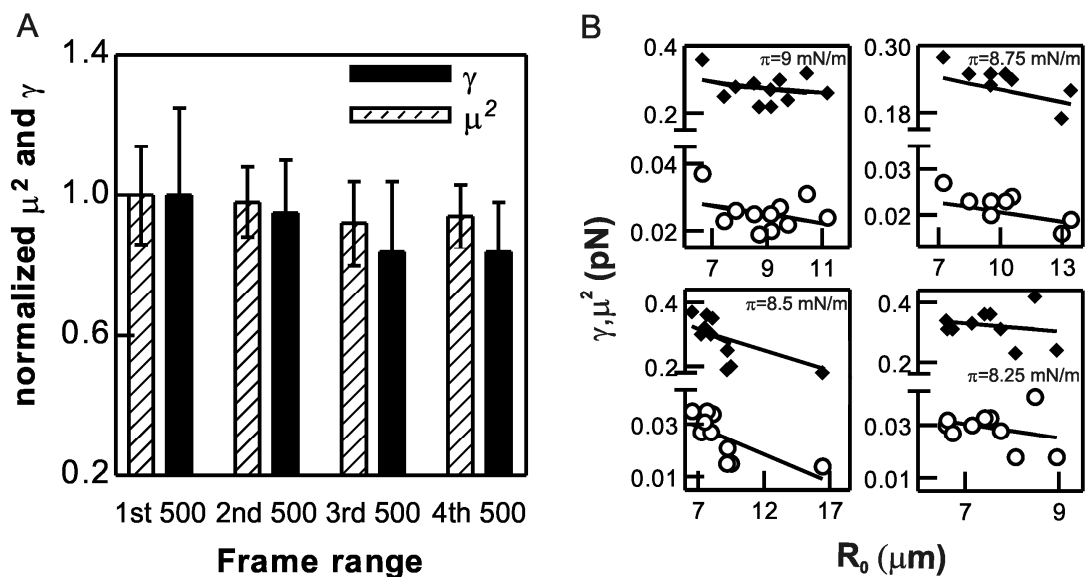
Figure 4.2: A) Line tension (black) and dipole density differences (lined) values with standard deviations as measured from 500 frame sequences of 10 domains at the critical composition and at $\pi = 9$ mN/m. Values for each domain were normalized to the average of all 10 domains as measured from the first 500 frames of each domain. Significant photobleaching was observed by the 3rd or 4th sets of 500 frames, corresponding to (constant) illumination times greater than 16 or 25 seconds, respectively.

The large number of domains analyzed in this report allowed quantification of the dependence of line tension on domain size. Surprisingly, a correlation was found between the radius and the γ and μ values obtained for each domain, with a slight reduction in both parameters with increasing domain size (see the examples of four different pressures in Figure 4.2B). Although the data from a single pressure were quite spread, normalizing all data sets to a single surface pressure using the critical exponents showed the dependence to be significant to a p-value of 0.05 for μ and 0.06 for γ.

Effect of Bulk Composition

In addition to quantification of critical exponents for line tension and dipole density difference at the critical composition (30% DChol), these parameters were measured at 35% and 40% DChol, compositions that lie in the same binary miscibility gap as the 30% sample, and domain edge fluctuations were observed for these additional mixtures as expected from the monolayer phase diagram(*7*). Although a trend of γ and μ increasing with decreasing surface pressure was observed for all compositions, and all data sets were fit well by power laws, the quantitative relationships between these parameters were not identical (Figure 4.3A and B). The critical exponents at 35% DChol were 1.2 for γ and 0.6 for μ^2, significantly higher than those for either 30% or 40% (Figure 4.3C). Since these critical exponents are strongly dependent on exact quantification of the transition pressure of the monolayer, it is difficult to confidently ascribe a trend to these observations.
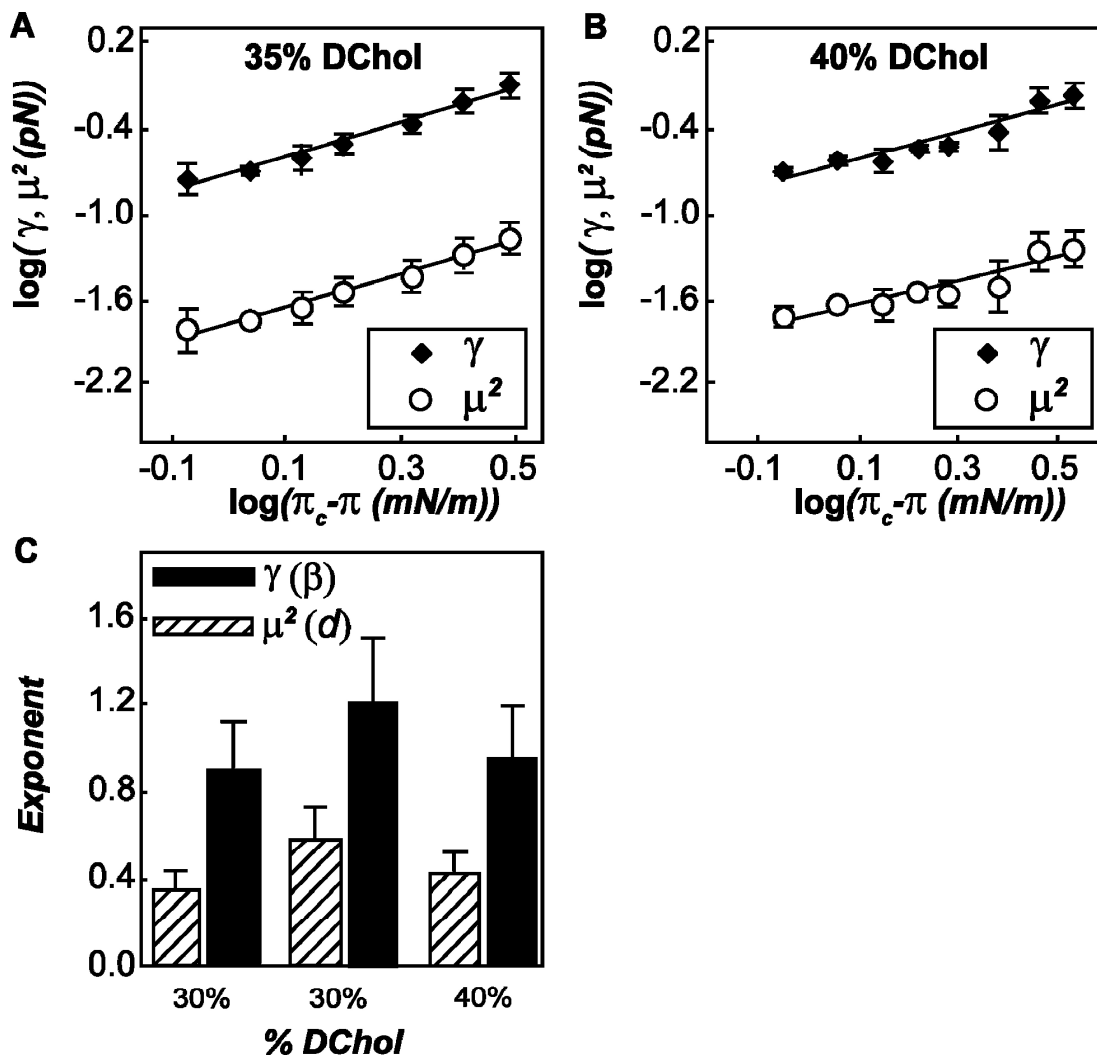
Figure 4.3: Measured values of line tension and dipole density difference depend on composition. Qualitatively similar logarithmic dependences on the reduced surface pressure were observed for 35% DChol / 65% DMPC (panel A) and 40% DChol / 60% DMPC (panel B) as for the critical composition (Figure 4.1A). C) Critical exponents determined from the slopes of the plots for the three compositions. Error bars reflect the 25% uncertainty in exponents resulting from a 0.5 mN/m uncertainty in the transition pressure.

Determination of Line Tension and Dipole Density Difference from Hydrodynamic Theory

As an alternative means of measuring line tension and dipole density differences, we employed the hydrodynamic mode-amplitude time decay theory outlined in Chapter 3. The Bond numbers (N_B) fit to the decay times via Equation 3.12 were observed to increase as the surface pressure approached the critical pressure (Figure 4.4A), qualitatively similar to those determined via the static capillary wave analysis (see Figure 3.2); the actual average values were, however, significantly smaller for domains at all tested surface pressures when using the dynamic analysis. Following determination of N_B, the line tension for a domain was calculated using Equation 3.11 (analogous to Equation 3.9 in the static analysis). These line tensions initially increased as the pressure was lowered from the critical pressure (in agreement with the qualitative trend shown previously), but the lowest two pressures resulted in average line tensions that reversed this trend (Figure 4.4B). In addition, the values at the 5 highest pressures are somewhat larger than those determined from the static analysis. With values in hand for both N_B and γ, the dipole density differences μ were calculated from the relation $N_B = 2\mu^2/\gamma$; these values also deviated from the qualitative trend observed for μ when determined via the static analysis, remaining approximately constant at the highest pressures and apparently decreasing at the lowest two (Figure 4.4C), contrary to expectation: as the critical pressure is approached, the compositional difference between the two phases disappears, along with the line tension(*7*).
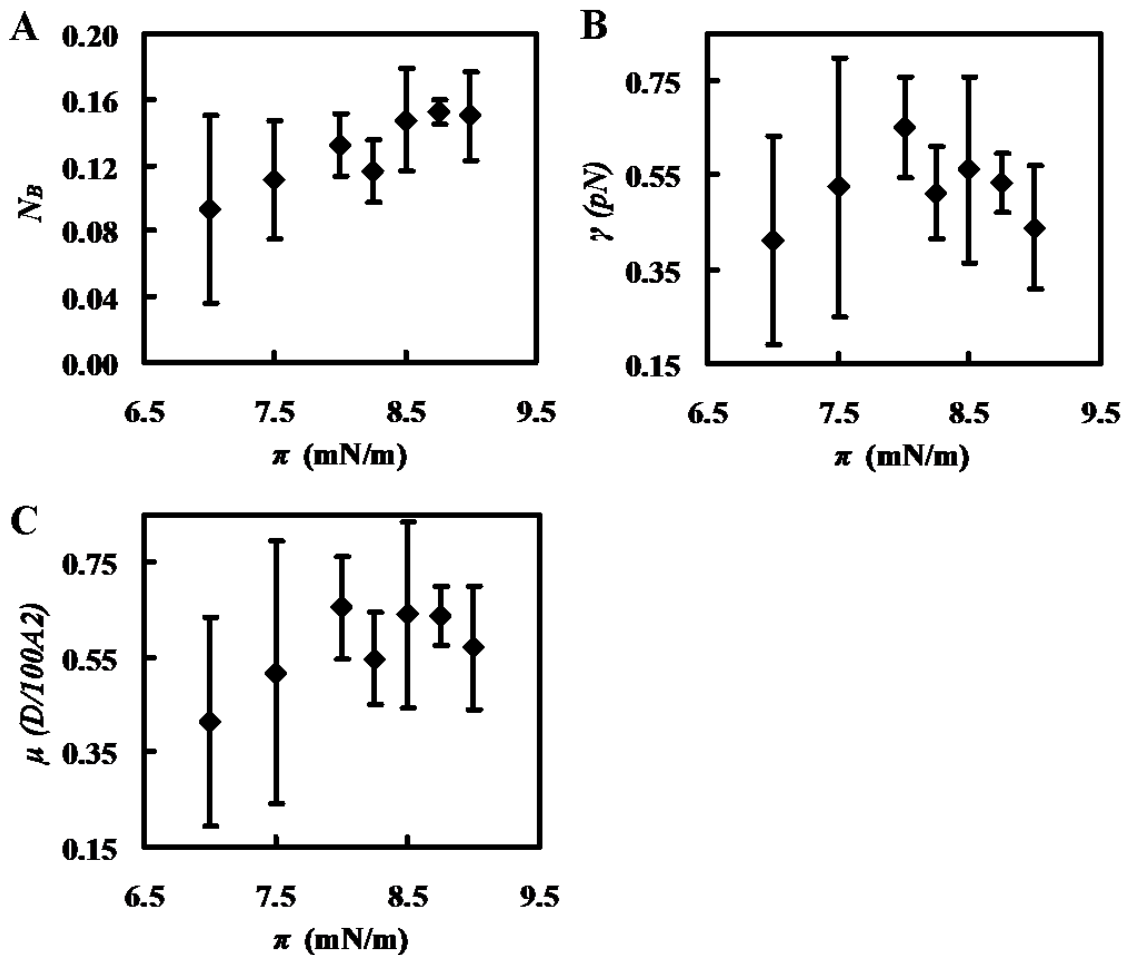
Figure 4.4: A) Fitted Bond number N_B decreased with increasing distance from the critical surface pressure (π_c = 10.1 mN/m) as determined using hydrodynamic theory, in qualitative agreement with the values obtained from static theory. The resulting line tensions (B) and dipole density differences (C), however, did not agree with the trends of the static theory results, though they are of the same order of magnitude.

Effect of Putative Linactant LysoPC

Finally, monolayers have also been prepared with a small amount of a suspected linactant: the 14 carbon chain lysoPC (1-myristoyl-2-hydroxy-*sn*-glycero-3-

phosphocholine), eg the single-chain variant of DMPC. The inclusion of just 0.5% (or more) lysolipid by mol fraction in the lipid monolayer led to noticeably different domain shapes (Figure 4.5) when compared to the lysolipid-free monolayers (Figure 3.4).
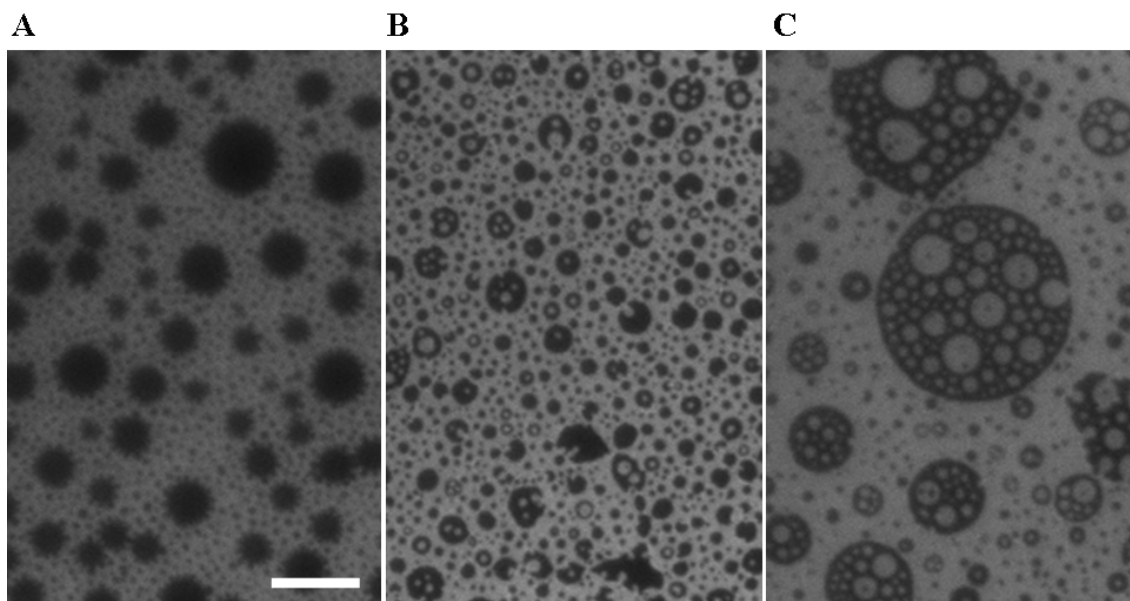
Figure 4.5: Fluorescent images of monolayers of 30% DChol / 69.5% DMPC / 0.5% Lysolipid immediately after spreading (A), following compression through the transition pressure and subsequent relaxation (B), and following repeated compression/relaxation through the transition pressure (C). Bar is 25 μm.

In order to utilize our boundary fluctuation analysis methods as before, we limited inclusion of lysolipid to 0.1% (mol fraction). Even this small (bulk) concentration significantly lowered the transition pressure from 10.1 to 7 mN/m. Domains were imaged as before and analyzed using the static capillary wave theory. Line tension and dipole density differences were measured to increase as the surface pressure was lowered

further from the transition pressure, as was previously observed for the lysolipid-free critical composition (Figure 4.6). Direct comparison between these values is enabled by plotting both sets relative to the reduced pressure, i.e. the difference between the transition and the measured pressure; note that a reduced pressure of 0 mN/m is a monolayer held at the transition pressure and for which line tension is expected to vanish. The majority of the average line tensions for the lysolipid-containing monolayer were statistically significantly higher than the critical composition, while only the highest two reduced pressures (corresponding to monolayers held at the lowest surface pressure) had significantly distinguishable dipole density differences.
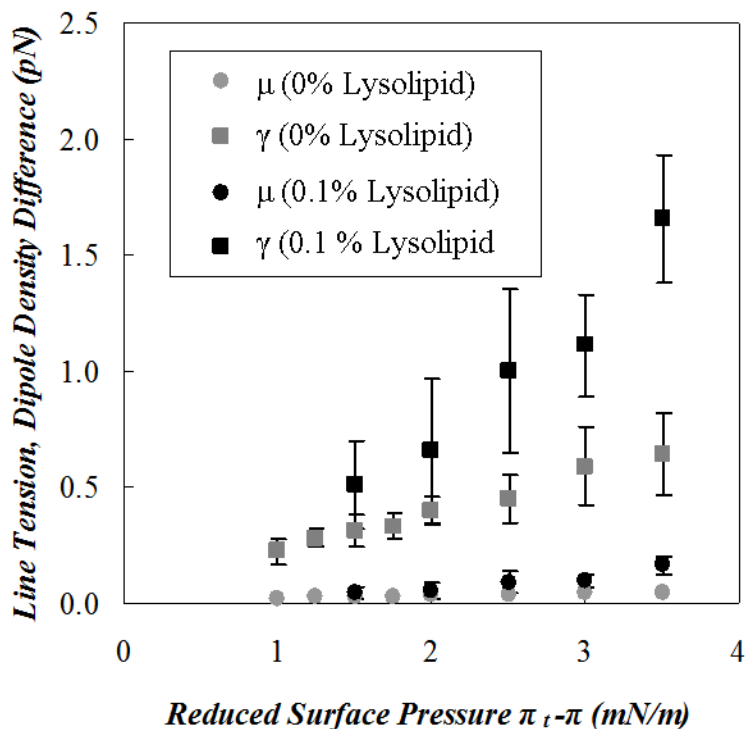

Figure 4.6: Measurements of line tension γ and dipole density difference μ at varying reduced surface pressures, eg, distances from the transition pressure. Line tensions

in the monolayer doped with lysolipid were measurably larger (at most pressures) than the lysolipid-free monolayer. Error bars represent standard deviations of averages from 3-4 domains (0.1% lysolipid) or 10 domains (0% lysolipid) at each pressure.

Discussion

Comparison to Predicted Critical Exponents

An advance of the present contribution is the analysis of a large data set in the framework of the Goldstein and Jackson theory(*6*) to independently measure dipole density difference and line tension in coexisting liquid phases to determine critical exponents for the variation of these parameters as a function of surface pressure. Our data included at least 1000 image frames per domain, 10 domains at each pressure, 6-7 surface pressures per composition, and three different compositions. This data volume allowed both confident determinations of average γ and μ values at each pressure, as well as quantification of the domain-to-domain variability in these measurements. The magnitudes of the measured parameters agree remarkably well with previously published values(*5*), especially considering the difference in the approaches used to derive them. It is interesting to note that the two-dimensional Ising model predicts a value of 1/8 for the exponent, β (*8*). Hirshfeld and Seul(*9*), however, found the shape of their mixed monolayer phase coexistence boundary to be in better agreement with an exponent of 1/3, the Ising model exponent for three dimensions(*8*), and Hagen and McConnell obtained β = 0.25 ± 0.7 from a set of different mixtures(*10*). As discussed in Ref. (*10*), despite the molecular thickness of monolayer films, intermolecular interactions in a lipid monolayer are only approximately two-dimensional, which may explain the deviation from the

87

2D Ising model expectation.

Comparison of Static and Hydrodynamic Analysis

The same data set has been analyzed via two related but distinct theories detailing the magnitude of boundary fluctuations of the imaged domains either stochastically (outlined in the Capillary Wave Theory section of Chapter 3) or sequentially (outlined in the Hydrodynamic Time-Decay Theory section of Chapter 3). Both methods have yielded Bond numbers (the first fit parameter used in both methods) which follow the expected trend, namely a monotonic decrease with lowered surface pressure away from the transition pressure. However, the dynamic approach was observed to be far more susceptible to noise, with no clear methodology to distinguish those fluctuation modes which were well-resolved as was possible in the static theory (see Figure 3.5). Furthermore, the heavy reliance on the first excited mode ($n = 2$) in Equation 3.12 caused the amplification of the uncertainty in that mode's time decay constant by affecting the resulting fits; this is less of an issue for the static theory in which the same mode has dramatically lower noise (compared to higher modes) due to the larger size range of the relevant fluctuations. Frequently, unrealistic values for N_B (and, subsequently, for γ and μ) would result. As a partial work-around, several different fits were obtained for each domain by using higher modes as well as $n = 2$ as the normalizing mode, with resulting equations similar to 3.12 but with τ_2 and β_2 replaced by those for a higher mode. Those which provided "reasonable" values were considered to have generated a successful fit; the resulting Bond numbers, line tensions, and dipole density differences were then averaged per domain and then again for a given pressure to generate the plots

shown in Figure 4.4. The quantitative disagreement in values between the static and dynamic theories is therefore less troubling given the difficulties in accurately resolving dynamic motion for a range of modes. It is nonetheless encouraging that the dynamic-derived values are of the same order of magnitude as shown by the more reliable static analysis, the results of which are further discussed below.

Significance of Reported Results and Method

An important distinction between our data and previously published results is the quantification of bare vs. effective line tension. Previous estimates of line tension in monolayers by physical perturbations(*2, 11*) have measured γ_{eff}, which includes both the bare line tension (γ) quantified here and the dipolar repulsive effects: $\gamma_{eff} = \gamma - \mu^2$. For our measurements, dipolar contributions to effective line tension were 7-9%, increasing slightly with film pressure for all compositions. It seems plausible that line active components could affect γ without modifying μ thereby changing the interdependence of these parameters(*12*). Preliminary results obtained with monolayers containing the presumed linactant lysoPC have indicated that it's inclusion as a minority component (here, at 0.1% mol fraction) will result in measurably distinct line tensions over a range of surface pressures (Figure 4.6). The significant reduction in the transition pressure serves as further evidence that lysoPC likely partitions preferentially at the boundary between domains in the phase-separated monolayer. Of some concern, however, is that the inclusion of lysoPC has a small but measurable affect on the dipole density difference, at least at pressures far enough from the transition pressure. Since the value of μ is dependent on the bulk composition of the two phases, it would be surprising for

it to be effectively modified by the inclusion of a minority component. This may indicate that the capillary wave theory used here may not enable the complete decoupling of the (competing) effects of line tension and dipole density difference under the experimental imaging constraints.

The photobleaching effect suggested by our experiments was not unexpected, since previous work cited a line tension reducing effect of cholestenone produced by the photo-induced oxidation of cholesterol(*13*). Although dihydrocholesterol was used in our studies to prevent oxidative effects(*13*), this cholesterol analog can be oxidized to cholestanone(*14*) with a similar structure to cholestenone, which could have similar line active properties. We included 5 mM DTT in the subphase to minimize photobleaching with the aim of maximizing the number of image frames that could be analyzed. Without DTT addition, the illuminated area of the monolayer was bleached within 15 s (referring to less than 1000 frames) to the point that boundary tracing by thresholding became inaccurate. It is interesting to note that photobleaching products appear to have the opposite effect (i.e. lead to an increase in line tension) in bilayer vesicles, as recently found by flicker spectroscopy in GUVs(*15*).

A further point of note is the composition dependence of the measured parameters γ and μ^2. The exponents for the relationship of these parameters to film pressure for all compositions were similar to the 1.0 for γ and 0.33 for μ^2 predicted by Benvegnu and McConnell(*5*), but there was an apparent increase in these exponents at non-critical concentrations. However, these exponents depend strongly on the experimental value for the transition pressure, which is observation-dependent, with ~25% variation in exponents expected with a 0.5 mN/m error in transition pressure. Thus, although we

observed composition-dependent variations in exponents, a systematic trend in the concentration dependence could not be deduced from our data set.

An unexpected finding enabled by the large data set used in these experiments was the domain size dependence of line tension and dipole density difference. Equation 3.8 predicts domain shape instability for domain radii that approach a critical value. It is possible that, as experimental domain radii get closer to the critical radius for the first instable mode, the capillary wave theory of GJ becomes increasingly inaccurate since fluctuations may transiently probe unstable regimes near the shape transition. This hypothesis awaits more systematic experimental investigation.

References

1. Keller, S. L., Radhakrishnan, A., and McConnell, H. M. (2000) Saturated phospholipids with high melting temperatures form complexes with cholesterol in monolayers, *J. Phys. Chem. B 104*, 7522.
2. Benvegnu, D. J., and McConnell, H. M. (1992) Line tension between liquid domains in lipid monolayers, *J. Phys. Chem. 96*, 6820.
3. Rowlinson, J. S., and Widom, B. (1982) *Molecular Theory of Capillarity*, Clarendon Press, Oxford.
4. Stottrup, B. L., Heussler, A. M., and Bibelnieks, T. A. (2007) Determination of line tension in lipid monolayers by Fourier analysis of capillary waves, *J. Phys. Chem. B 111*, 11091.
5. Benvegnu D.J., and McConnell H.M. (1992) Line Tension between Liquid Domains in Lipid Monolayers, *J Phys Chem-Us 96*, 6820
6. Goldstein, R. E., and Jackson, D. P. (1994) Domain shape relaxation and the spectrum of thermal fluctuations in Langmuir monolayers, *J. Phys. Chem. 98*, 9626.
7. Benvegnu, D. J., and McConnell, H. M. (1993) Surface dipole densities in lipid monolayers, *J. Phys. Chem. 97*, 6686.
8. Rowlinson JS., and Widom B. (1982) *Molecular Theory of Capillarity*, Clarendon Press, Oxford.
9. Hirshfeld, C. L., and Seul, M. J. (1990) Critical mixing in monomolecular films: pressure-composition phase-diagram of a 2-dimensional binary mixture, *J. Phys. 51*, 1537.
10. Hagen, J. P., and McConnell, H. M. (1997) Liquid-liquid immiscibility in lipid monolayers, *Biochim. Biophys. Acta - Biomem. 1329*, 7.

11. Wurlitzer, S., Steffen, P., and Fischer, T. M. (2000) Line tension of Langmuir monolayer phase boundaries determined with optical tweezers, *J. Chem. Phys. 112*, 5915.
12. Trabelsi, S., Zhang, S., Lee, T. R., and Schwartz, D. K. (2008) Linactants: Surfactant analogues in two dimensions, *Phys. Rev. Lett. 100*, 037802.
13. Benvegnu, D., and McConnell, H. (1993) Surface Dipole Densities in Lipid Monolayers, *J Phys Chem 97*, 6686.
14. Grimalt, J. O., Fernandez, P., Bayona, J. M., and Albaiges, J. (1990) Assessment of fecal steroids and ketones as indicators of urban sewage inputs to coastal waters, *Environ. Sci. Technol. 24*, 357.
15. Esposito, C., Tian, A., Melamed, S., Johnson, C., Tee, S. Y., and Baumgart, T. (2007) Flicker spectroscopy of thermal lipid bilayer domain boundary fluctuations, *Biophys. J. 93*, 3169.

Chapter 5: Lipid Bilayer Phase Behavior

Measurements described below concern the liquid-liquid phase separation of lipid membranes composed of a bilayer (two opposing monolayer leaflets) in the form of a giant unilamellar vesicle, thereby building upon the biological relevance of the results presented in Chapter 4 on lipid monolayer systems. In particular, the shape of the bilayer is mechanically manipulated to achieve equilibrated and connected regions of high and low curvature to investigate the coupling of membrane shape and composition in the strong segregation limit. In addition to the line tension present at the phase boundary of a domain (as examined in Chapter 4 for monolayers and by Esposito et al for bilayers(*1*)), curved membranes contain an additional energy term stemming from the characteristic resistance towards bending (see Chapter 3). The difference in bending stiffness between the liquid ordered (Lo) and liquid disordered (Ld) phases is here utilized to enable selective sorting of both lipids and membrane-associated protein.

Curvature Sorting by Bending Stiffness[g]

Curvature-Induced Phase Transition

To systematically probe the effects of curvature on nucleation and growth of membrane domains, we used a classical vesicle pipette aspiration approach(*2*). Membrane tubes were pulled by beads that were moved either by a second aspiration pipette (Figure 5.1A) or by a laser trap (see Figure 5.1B and Chapter 2). From a thermodynamic point of view, vesicles provided a particle reservoir that fixes lipid chemical exchange potentials(*3*). The lateral membrane tension was controlled by means

---

[g] Parts of this chapter are reproduced from previously published work: Heinrich, M. C., Tian, A., Esposito, C., and Baumgart, T. (2010) Dynamic sorting of lipids and proteins in membrane tubes with a moving phase boundary, *Proc. Natl. Acad. Sci. U.S.A. 107*, 7208.

of the pipette aspiration pressure. Figure 5.1C shows that our vesicle composition was within the Lo/Ld phase coexistence region, in the strong segregation limit of the phase diagram(*4*). This composition was chosen to yield vesicles with an Lo/Ld area fraction ratio typically larger than one (to facilitate tube pulling from the Lo phase) and with low domain boundary line tension [to avoid tube fission(*5*)].
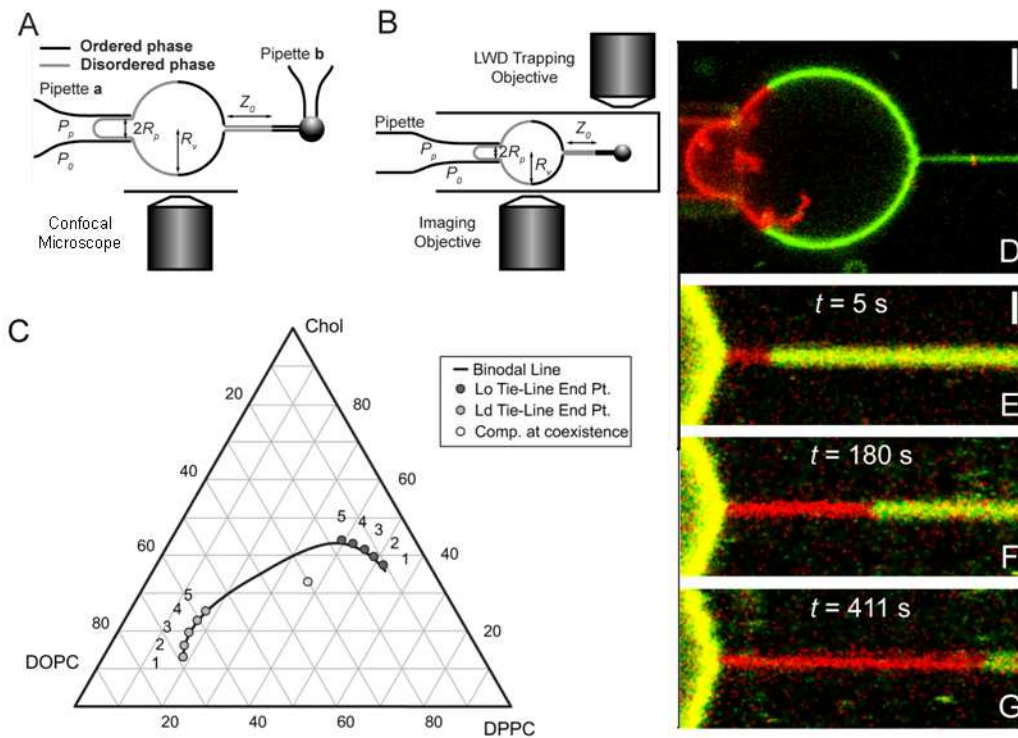
Figure 5.1: Curvature-induced first-order demixing transitions are observed in a tube pulled from lipid mixture membranes. A) Illustration of tube pulling by two-micropipette setup. The Ld phase (gray lines) of a vesicle with radius R_v is aspirated by micropipette **a**. A streptavidin-coated bead held by micropipette **b** is used to pull a tube from the Lo phase (black lines) of the vesicle. Z_0 represents the length of the Ld phase growing from the tube neck. B) Schematic of a specially designed fluorescence imaging/optical

trapping setup. C) Approximate location of Ld/Lo phase coexistence region is indicated by a curve. Lipid composition in which curvature-induced Ld domain formation was observed is indicated by an open circle, while Lo (Ld) compositions are indicated with dark (light) gray circles; see Table 5.1. D-G) Confocal microscopy images of domain growth (at constant tube length) using two-micropipette setup. D) A tube is pulled from the Lo phase (green) of a vesicle and imaged before observable Ld phase (red) growth occurred. Scale bar: 2 μm. E-G) Growing Ld domain nucleated at the tube neck at constant reservoir membrane tension $\sigma = 0.033$ mN/m. Growth time is denoted in each panel relative to time of first observation of domain. The Lo phases of vesicle and tube appear yellow due to enhanced red channel display, used to emphasize the Ld phase. Scale bar: 1 μm.

Vesicles with a single large Lo domain coexisting with a single large Ld domain (Figure 5.1D) were selected and aspirated from the Ld phase (shown in red in Figure 5.1D; aspiration pipette shown at the left edge of Figure 5.1D). Shortly (typically milliseconds to seconds but occasionally up to several minutes) after pulling a tube from the Lo phase of the vesicle (labeled in green by means of the peripherally binding protein cholera toxin (CTB, which binds to ganglioside, GM1) in Figure 5.1D–G), an Ld domain nucleated at the neck of the tube, while the total tube length was held constant. Nucleation times (defined as the time between the end of the process of tube extraction and the first observation of a domain) were variable, in accordance with thermally activated nucleation.

Exclusively, only a single Ld domain nucleated in the tube, and it was

always located at the tube neck. Both of these observations suggest that curvature/composition coupling(*6-7*) rather than photoeffects(*8-9*) caused phase separation. This conclusion was further supported by the qualitative observation that increasing curvature (by increasing the vesicle lateral tension) on average decreased the time needed for nucleation [from up to minutes for the lowest lateral tensions to short (milliseconds) times for the highest tensions considered].

Curvature-nucleated domains grow in time; i.e., the red Ld phase invades the tube membrane, progressively replacing the green Lo phase (Figure 5.1E-G; time was measured relative to the first observation of fluorescence heterogeneity at the tube neck). The comparison of the time needed for domain boundary movement between first and second (Figure 5.1E and F) vs. second and third (Figure 5.1F and G) frames reveals that the domain boundary velocity decreased with time.

Sorting of Protein into Unfavorable Curvatures

Previous research has shown that CTB bound to the outer leaflet of giant unilamellar vesicle (GUV) membranes preferentially partitions away from high curvature tubes pulled from vesicles with equilibration times less than 1 min(*6-7*). Furthermore, Ld phase lipid diffusion coefficients in our mixture are in the range of ~3-5 $\mu m^2\!/s$(*10*). Because green CTB fluorescence is observed for >400 s on the tube (Figure 5.1G), the red Ld domain shown in Figure 5.1E-G serves as a diffusion barrier to protein (and lipid) exchange between tube Lo and vesicle Lo domains. Such diffusion barriers have been postulated to modulate intracellular lipid and protein sorting(*11*).

The addition of the CTB/GM1 complex to our membranes so far has served

to illustrate the possibility of dynamic protein sorting in Figure 5.1. It has previously been shown, however, that CTB itself is an effective curvature sensor(*6-7*) and furthermore amplifies lipid curvature sorting(*7*). Therefore, in order to quantitatively characterize the dynamic lipid phase behavior depicted in Figure 5.1D-G, CTB/GM1 was omitted in the following results, relying solely on the Ld phase preference of the lipid dye to distinguish domains.

Time-Dependence of Nucleated Domain Growth and Tube Force Reduction

We found a systematic dependence of domain boundary positions (measured as the distance between the intratube phase boundary and the tube neck) on both observation time and lateral membrane tension (Figure 5.2A). The domain boundary length to a good approximation showed a square-root time dependence (Figure 5.2B).

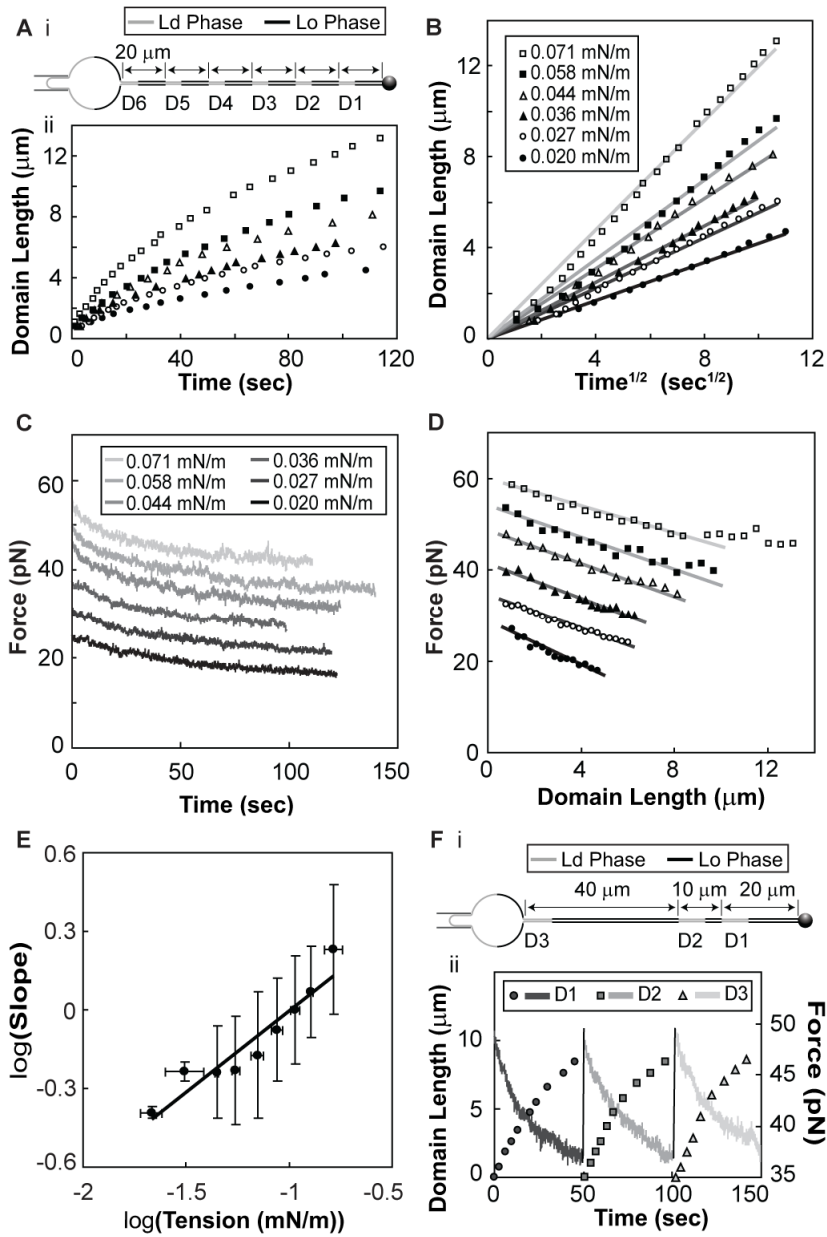Figure 5.2: Curvature-induced domains show parabolic growth and characteristic pulling

force decay. *A*) Six domains were sequentially nucleated at the tube neck of a single

vesicle through stepwise total tube length extension followed by domain growth at

constant total tube length (and reservoir tension) as shown in schematic (i). Domain

length as a function of time relative to the first moment of detectable fluorescence

heterogeneity at the tube neck (ii). Closed and open circles, closed and open triangles, closed and open squares: domains grown at pressures of 17 ± 0.5 Pa, 23 Pa, 31 Pa, 38 Pa, 50 Pa, and 61 Pa, respectively, corresponding to the lateral tensions in B. *B*) Same data as in A) plotted vs. $t^{1/2}$. Linear fits are shown as solid lines. *C*) Tube force is observed to decrease after domain nucleation and concomitant to growth. The black curve corresponds to the first domain generated (closed circles in A), B), and D)); lighter gray curves correspond to domains grown sequentially at increasing aspiration pressures as in A). *D*) Tube force as a function of domain length; symbols as in panel B). Solid lines are linear fits for domain lengths up to 10 μm. *E*) Double logarithmic plot (with standard deviations) of the slopes of the linear fits as in B) as a function of membrane tension for 6 different vesicles and 26 vesicle tensions. The slope of a linear fit to the binned data is 0.62 ± 0.08. F) Three sequentially nucleated domains grown at constant membrane tension but with different initial lengths of Lo phase tube [schematic in (i)] exhibited essentially identical growth behavior and force decay (ii) for various total tube lengths.

Ld phase domains that had been nucleated at the tube neck could be pulled into the tube interior by quickly (typically 30 μm⁄s) increasing the total tube length by moving the pulling bead. This led to nucleation (at the tube neck) of a new (here called primary) domain (with nucleation times similar to the previously nucleated, here called secondary, domain) in the Lo phase membrane region that was pulled onto the tube (see schematics in Figure 5.2A and F). Essentially identical growth dynamics were observed for multiple domains that resulted from successive pulls of the same tube (see Figure 5.2F and Figure 5.3A) when vesicle lateral tension was held constant. These observations allowed us

99

to perform multiple domain growth experiments using the same tube and vesicle, but varying the vesicle (below also called reservoir-) lateral tensions to change tube curvature.
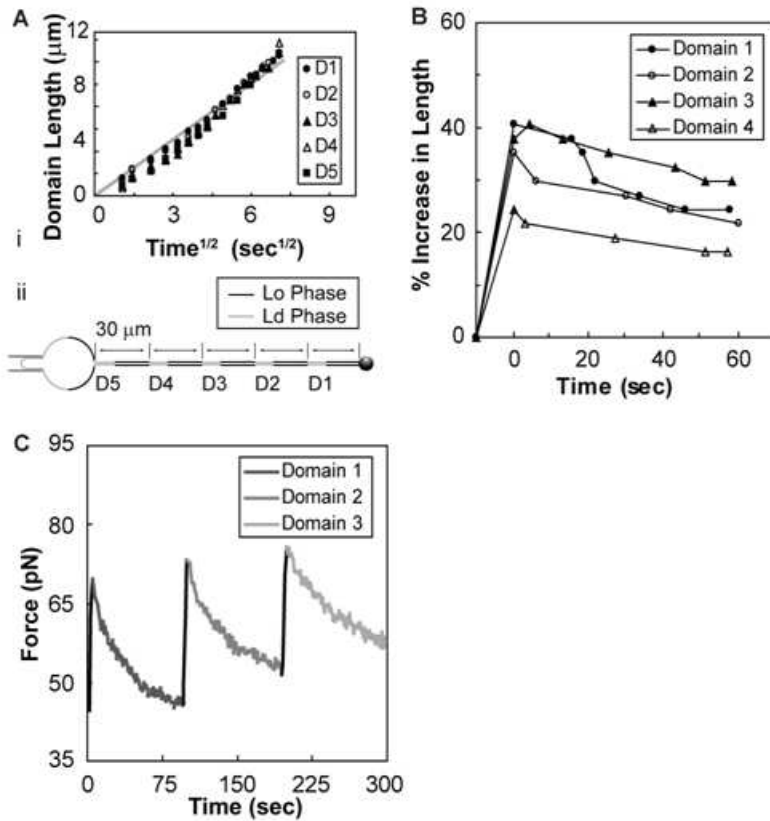
Figure 5.3: Domain growth dynamics are independent of total tube length and domain nucleation order. *A*) Domain length over time for five domains grown consecutively on the same vesicle, similar to method used to obtain data in Figure 5.2B but without changing aspiration pressure (membrane tension) between domains: pressure was held constant at 35 Pa (membrane tension of 0.04 mN/m). All five domains are observed to grow at the same rate regardless of nucleation order and total tube length. Solid line is a linear fit to the aggregate of all five domains. The initial length of Lo phase

available for each new Ld domain to invade was kept constant at 30 μm. *B*) Change in (secondary) domain lengths of the first four domains shown in panel A) immediately after being pulled entirely into the tube and far from the vesicle neck. The domain lengths increase sharply as a result of a decrease in domain radius immediately after tube elongation; they slowly decrease over time with increases in domain radius as the tube membrane tension drops due to the nucleation and growth of a new primary domain (see Figure 5.5). Times $t = 0$ for each consecutive secondary domain are defined as the times of nucleation of each following primary domain. *C*) Force decays observed for three sequential domains generated at the same aspiration pressure of 22 Pa ($\sigma_{res} = 0.06$ mN/m). Decays are nearly identical in shape.

Concomitant to the domain length characterization analyzed in Figure 5.2A and B, we measured the pulling force exerted by the tube membrane on a bead held in an optical trap. Following curvature-induced phase separation, tubes displayed pulling forces that decayed on time scales longer than 100 s. The pulling force decay for the six domains analyzed in Figure 5.2A and B is shown in Figure 5.2C. Intriguingly, pulling forces decreased essentially linearly with domain boundary displacement (Figure 5.2D). We characterized the time scales required for initial mechanical equilibration after membrane tube elongation or aspiration pressure change using homogeneous vesicles (without phase separation). These time scales were less than 2 s to reach a constant pulling force after tube elongation (see Figure 3.7A, consistent with ref. (*12*) and less than 1 s to reach a constant pulling force after changing the aspiration pressure (Figure 3.7B). Accordingly, the force decay during domain growth (Figure 5.2C) occurs on

a time scale significantly longer than needed to reach mechanical equilibrium after initial tube formation.

Figure 5.2E suggests a power-law dependence between the slopes of Figure 5.2B and vesicle lateral tension, with an exponent of 0.62 ± 0.08. This systematic dependence further emphasizes that curvature, rather than photoeffects, is the driving force for phase separation and mass transport. For high vesicle tensions, we confirmed that after long (>10 min) waiting times, tether membranes consisted of one single Ld domain, consistent with ref. (*13*).

Discussion

Application of a Mass-Transport Theory

The slowing down of domain boundary velocities observed in Figures 5.1 and 5.2 suggests that the growing Ld phase presents a mass transport resistance that grows with its length. The parabolic moving boundary ("Stefan problem") behavior that we observe here is displayed by many physicochemical phenomena involving both heat and mass transfer(*14-15*). We derived a simple thermodynamic transport model (see Chapter 3 for details) that enables us to explain dynamic aspects of the findings shown in Figures 5.1 and 5.2. The key features of the model are depicted in Figure 3.8. The model predicts the Ld domain length Z_0 to grow in time t according to (see Equation 3.19):

$$Z_0^2 = tAC^2 \tag{4.1}$$

where A is the product of several time- and curvature-independent parameters (including the composition-dependent bending stiffness of the Ld domain) and C is the curvature of the Ld domain in the tube.

We note that Equation 4.1 is based on numerous simplifications required to obtain an analytically tractable model. These include (i) neglect of area density (ρ) difference between Lo and Ld phases, (ii) assumed absence of friction effects contributed by water (and membrane area) transport among tube and vesicle (discussed below in the context of simulated tube shapes), (iii) spatially fixed vesicle/tether phase boundary, (iv) assumption of time-independent tube radii of Lo and Ld phases, and (v) absence of concentration gradient in tube Lo phase. Assumptions (iii) and (iv) were investigated through numerical shape simulations (see Chapter 3 for details), the results of which will be discussed below. However, assumptions (iv) and (v) would predict a time-independent tube force:

$f = 2\pi\sqrt{2\sigma_{Lo}\kappa_{Lo}} = 2\pi\kappa_{Lo}C_{Lo}$, where mechanical quantities are those near the bead; this is clearly not in agreement with the experimental results shown in Figures 5.2 and 5.3.

In order to explain the pulling force decay, we consider the following two alternative hypotheses. The first is that the pulling force decreases due to a change in lateral tension of the tube at fixed (vesicle) reservoir tension, while the composition of the tube domain in the Lo phase remains approximately constant (in accordance with the assumption of an Lo phase reservoir; see Figure 3). The second hypothesis is that the bending stiffness of the Lo phase of the tube decreases with time because the imposed curvature field could lead to a change in the composition of the Lo phase near the bead to lower the tube free energy(6-7). In this case, the bending stiffness at the end of the tube decreases through diffusive composition change, and the time scales of the lipid exchange between the end of the tube and the vesicle would be affected by the total tube length.

In support of the first, rather than the second hypothesis, we found

negligible influence of the total tube length on domain growth (Figure 5.2F and Figure 5.3A). We furthermore verified that pulling force decays were similar (Figure 5.2F and Figure 5.3C) in serially nucleated domains in the same tube at constant reservoir lateral tension, confirming that the composition at the tube end did not measurably change over the time course of our experiments. Furthermore, secondary (i.e., intra-tube) Lo phase domains were observed to reduce their length during the growth process of the primary domain (Figure 5.3B). This is consistent with increasing radius of the secondary domain at constant domain area, due to decreasing lateral tension during the primary domain growth process. As Figure 5.3B shows, multiple intra-tube domains displayed similar shortening during the primary domain growth.

We thus concluded that the coupling of lateral tension between the vesicle reservoir and the tube changed with time. In additional support of this conclusion, we observed a rapid (<1 s) force drop associated with the following phenomenon: Occasionally, small (radius on the order of 1 μm) Ld phase domains diffused from the vesicle into the neck region and became irreversibly trapped at the tube neck. This is shown for three examples in Figure 5.4, where Lo phase tubes were pulled from the vesicle, and no curvature-induced Ld phase nucleation was observed before the small domain was trapped in the neck region. The pulling force was constant before the Ld domain approached the neck region (consistent with the expectation of an approximately time-independent tube composition) and dropped rapidly as the Ld phase was trapped in the neck. This force drop indicated that the detailed geometry of the tube neck was pivotal in determining the pulling force exerted by a tube with phase coexistence. After the fast force drop, no additional force decay occurred while the Ld phase invaded
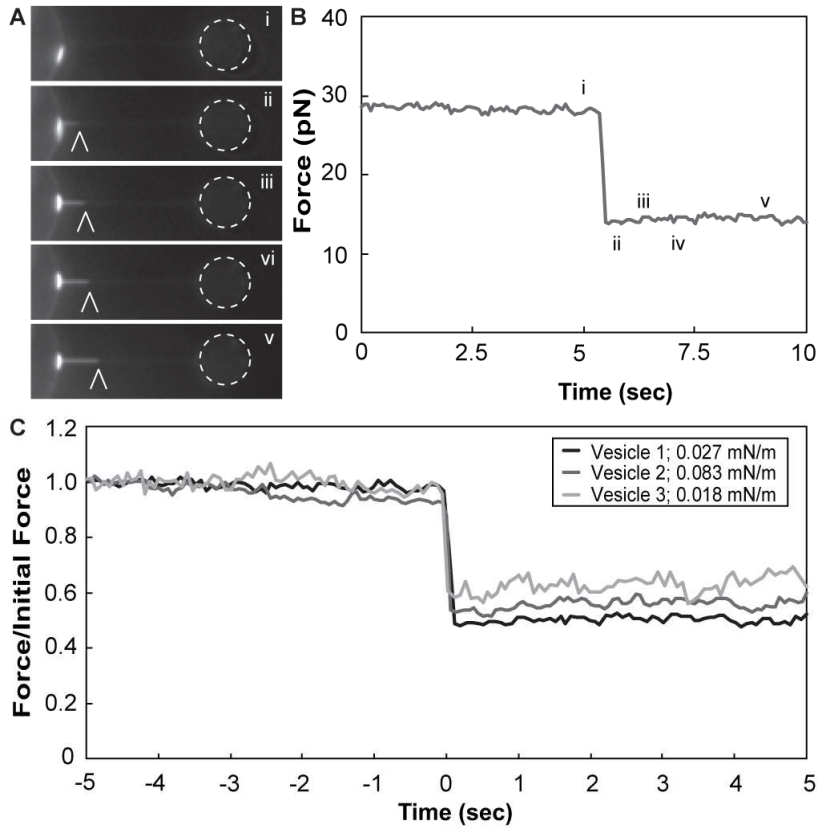
the Lo phase tube.

Figure 5.4: Curvature-induced domain nucleation and growth is distinct from diffusion of preexisting microdomains. *A*) Fluorescence image *i* shows a dimly fluorescent tube that is entirely in the Lo phase. The aspiration pressure was 16 Pa (σ_{res} = 0.027 mN/m). The portion of the vesicle shown on the left shows a small micron-sized Ld phase domain (bright line) amid a majority Lo phase. The pulling bead is illustrated with a white dashed circle on the right. The microdomain showed diffusive mobility on the vesicle, but on approaching the neck region was irreversibly attracted by the neck, as seen in image *ii*. The Ld phase boundary position in the tube is indicated by white arrows. In *iii-v*, the microdomain continued to invade the tube, likely by curvature-induced domain area

growth, reaching a length of 5 μm by image *v*. *B*) Pulling force immediately before and after a microdomain was locked at the tube neck. The constant force leading up to image *i* is evidence of a constant tube composition. At the moment of contact of the Ld microdomain with the tube neck, the force drops within < 1 s. Further invasion of the Lo phase by means of the growing domain locked at the neck did not measurably alter the tube force, in contrast to domain growth following nucleation at the tube neck (see Figure 5.2). *C)* Similar force drops are observed for two additional vesicles in which a small Ld domain became trapped at the tube neck. Tube force here is normalized relative to the initial tube force for each vesicle, with force drops ranging between 37% and 49%. Force drops are observed to occur on similar (fast) time scales compared to slow (several minutes) force decay during domain nucleation and growth.

Simulation of Vesicle/Tube Neck Geometries

To gain further mechanical insight, the geometry of tube necks was obtained from numerical solutions to the differential shape equations of lipid bilayer membranes with phase separation(*16*), including an axial pulling force(*17-18*); details are provided in Chapter 3. Thus, our vesicle/tube system is modeled by a catenoid attached to a cylindrical tube. For all calculated shapes shown below, the total membrane area was held fixed(*19*), but the catenoid edge radius was variable to allow for changes in the tube geometry. In this manner, the catenoid serves as a membrane area-reservoir, reflecting our experimental system where the pipette-aspirated membrane fraction of the GUV provided an area reservoir. Shapes such as those in Figure 5.5 were calculated at constant lateral tension in the Lo phase of the catenoid, again reflecting our experimental

system. Figure 5.5A shows the profile of a membrane tube without phase separation in order to illustrate a well-known feature: At the tube neck, the radius shows an invagination and a locally increased free energy density(*17*). This fact explained why the curvature induced Ld phase always nucleated at the neck. We next aimed to calculate shapes of phase-separated tubes. Knowledge of the elasticities of the Lo and Ld phases was thus required(*19*). We derived bending stiffness values from pulling force measurements(*8*) in homogeneous vesicles with several different compositions corresponding to Ld and Lo phases. We found values of roughly $0.8 \cdot 10^{-19}$ J for the Ld phase and $3.6 \cdot 10^{-19}$ J for the Lo phase (see Figure 3.7C and Table 5.1). This yielded a ratio $\varepsilon \approx 4.5$ of elasticities in the Lo vs. Ld phase, in agreement with previous estimates(*19-20*).With this value for ε, we calculated series of tube shapes (Figure 5.5) mimicking the experimental phase-separation process of Figures 5.1 and 5.2, ignoring, for the moment, contributions from a line tension T and Gaussian bending stiffness differences ζ.
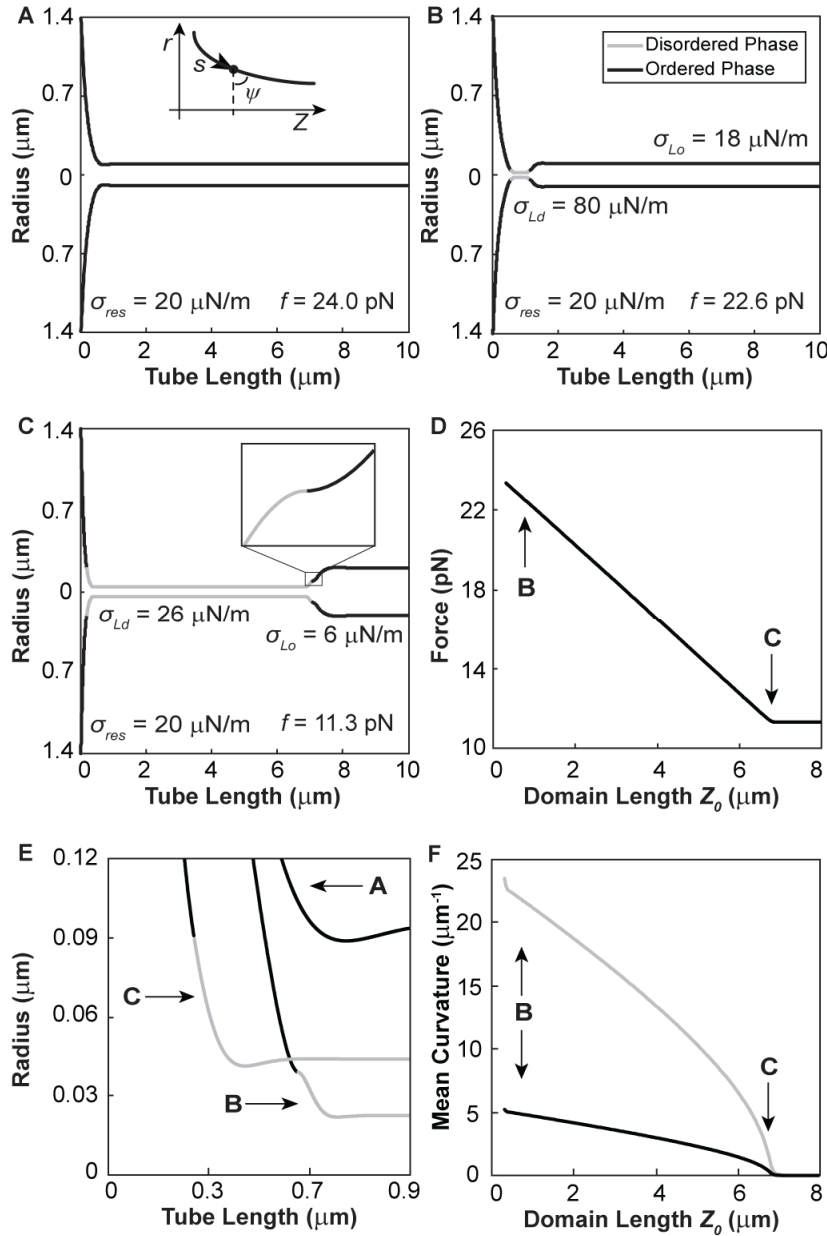
Figure 5.5: Computational shape series from membrane elasticity theory shows pulling force decay. *A*) Single phase tube with an Lo phase bending stiffness of 364 pN·nm. Tube radius reaches a minimum in the neck region. Tube force for this shape is 24.0 pN with a lateral tension of 0.020 mN∕m (equivalent reservoir tension for all following shapes). The inset illustrates parameterization of shape coordinates (see Chapter 3). *B*) Three-phase tube with Ld phase domain (gray) with a bending stiffness of 81

108

pN·nm (4.5 times less than the Lo phase). The resulting Ld domain tension is higher than both the reservoir and Lo phase tube tensions. *C*) Tube shape with a large Ld phase domain area. The Ld tension is now close to the reservoir tension. The inset shows the leading-edge phase boundary. *D*) Tube force decreases linearly with domain length until reaching a plateau. Arrows correspond to shapes in B and C. Note that the lateral tensions of both the Lo and Ld phase regions of the tube decrease during domain growth. *E*) Close-up of neck region for shapes shown in A-C. Vesicle/tube phase boundary moves onto the catenoid during domain growth. *F*) Mean curvature of Lo (black) and Ld (gray) phases at the catenoid/tube phase boundary as a function of domain length. Both mean curvatures decrease to zero upon reaching the force plateau shown in D. The curvature on the Ld and Lo phase sides of the phase boundary differ, in accordance with the mechanical jump conditions (see Chapter 3).

Nucleation of an Ld domain led to further constriction of the neck (Figure 5.5B). To calculate series of shapes for phase-separated tubes at constant total membrane area, we varied the area fraction of the tube Lo phase and the tube Ld phase, keeping the area of the catenoid Lo phase constant (Figure 5.5 B and C). Note that such shape series do not preserve the total Lo/Ld area fraction. Mass conservation of Ld phase and Lo phase lipids can, in principle, be achieved by adding an additional Ld phase to the nearly flat catenoid (as in the experimental vesicles; see Figure 5.1). The area fraction of this additional Ld phase could then be varied to fix the total area fraction of the Ld phase while varying the tube area fractions. Since this amendment in the quasi-flat reservoir would have negligible mechanical consequences, we varied the area fraction of the

tube domains only and regarded the catenoid as a thermodynamic particle- and area-reservoir, fixing chemical potentials (instead of particle numbers).

Figure 5.5A-C indicate that during invasion of the tube by the growing Ld phase domain, the left-hand side phase boundary moves into the catenoid (note that both phase boundaries thus were not fixed in space but allowed to move to minimize the shape's total mechanical energy; see Chapter 3). We note for completeness that the intra-tube phase boundary shows a tangent angle of $\pi/2$ (inset of Figure 5.5C)(5). During the tube invasion, the calculated pulling force decays (see Figure 5.5D). Remarkably, the relation between Ld domain length and pulling force is linear in the numerically obtained shape series (Figure 5.5D), as in the experiment (Figure 5.2D). Note that a force plateau is reached before the Ld phase has completely replaced the tube Lo phase (Figure 5.5C and D).

The reason for the force decay is embedded in the complicated mechanical jump conditions at the vesicle/tube phase boundary (see Chapter 3). However, there is a conceptually straightforward explanation. Before phase separation, the lateral tension within the membrane tube is equivalent to the reservoir tension (Figure 5.5A). Near the end of the invasion process, the left-hand phase boundary is located in a membrane region with negligible curvature (Figure 5.5C). Figure 5.5E shows a magnification of the catenoid/tube phase boundaries. The mechanical jump conditions therefore dictate the lateral tension in the Ld phase domain to be the same as the reservoir lateral tension (in the absence of line tension). At the right-hand (intratube) phase boundary, however, the axial force balance requires $\sigma_{Ld}/\sigma_{Lo} = \kappa_{Lo}/\kappa_{Ld} = \varepsilon$ (5). If both phase boundaries were localized within the tube (as is approximately the case immediately after nucleation

of an Ld domain, Figure 5.5B), then the lateral tension within the tube Lo phase would be identical to the reservoir tension. This is because at both phase boundaries the lateral tension would jump, but in opposite directions, according to the axial force balance relation. If only one phase boundary is localized within the tube region, as in Figure 4C near the end of the invasion process, the lateral tension within the tube Lo phase must be smaller by an amount that is given by the bending stiffness ratio. During the invasion process, the lateral tension of the Lo phase tube domain therefore monotonically decreased from the reservoir tension σ_{res} to $\sigma_{Lo} = \sigma_{res}/\varepsilon$. In accordance with this interpretation, Figure 5.5F shows that the mean curvature at the vesicle/tube phase boundary decreases during domain growth, vanishing at the pulling force plateau of Figure 5.5D. Note that the magnitude of the vesicle/tube phase boundary displacement from the tube neck suggested by Figure 5.5E is not microscopically resolvable, consistent with Figure 5.1E-G.

In line with the interpretation of a tension-related force decay, the apparent bending stiffness κ_{app} calculated from the experimentally determined pulling force and σ_{res} (i.e., $\kappa_{app} = f^2/\left(8\pi^2\sigma_{res}\right)$) continuously decreased (Figure 5.6) from Lo phase values before invasion to values approaching those for an Ld phase at the force plateau; here $f_{plateau}^2 = 8\pi^2\sigma_{Lo}\kappa_{Lo} = 8\pi^2\sigma_{res}\kappa_{Ld}$ (5), since at the plateau $\sigma_{res} = \sigma_{Ld}$ (see Figure 5.5).
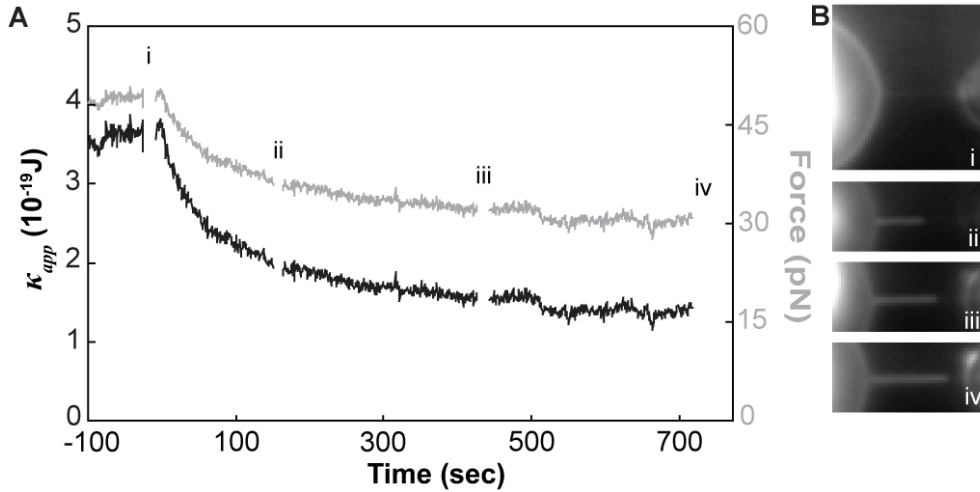
Figure 5.6: Apparent bending stiffness decays during domain growth. *A*) An aspirated phase-separated vesicle with tube maintains a constant force (gray line) prior to domain nucleation for times between -100 and zero seconds; see image *i* in panel *B*). Force begins to decrease when a domain nucleates (defining time zero) and grows in length, as evidenced in images *ii-iv*. The apparent bending stiffness (black line) over time is calculated from the pulling force and the (fixed) reservoir tension. After 700 seconds of domain growth at a constant reservoir lateral tension (σ_{res} = 0.08 mN/m), the apparent bending stiffness had decreased by a factor of 2.7. *B*) Fluorescence images showing the Lo phase of the aspirated vesicle on the left attached to the bead on the right with a tube. The 8 µm tube was initially entirely in the Lo phase (image *i*) and was dimly fluorescent. By image *ii*, a 4.2 µm domain was visible. This domain continued to grow in length towards the end of the tube as shown in images *iii* and *iv*.

We observed that several minutes after primary domain growth was initiated, the lengths of secondary domains remained approximately constant, consistent with the observation of a pulling force plateau at long observation times (Figure 5.6 and

112

Figure 5.5D). Under such conditions, the domain length of a secondary domain was observed to be linearly related to the square root of systematically varied reservoir tension (Figure 5.7). Since the domain radius is inversely proportional to $\sqrt{\sigma_{res}}$ (*17*), this finding shows that the secondary domain area $A_{sec} \approx 2\pi R_{sec} L_{sec}$ (excluding the phase boundary geometry; see Figure 5.5) was independent of domain curvature. This suggests that the phase diagram is unaffected by curvature (Figure 3.8C).
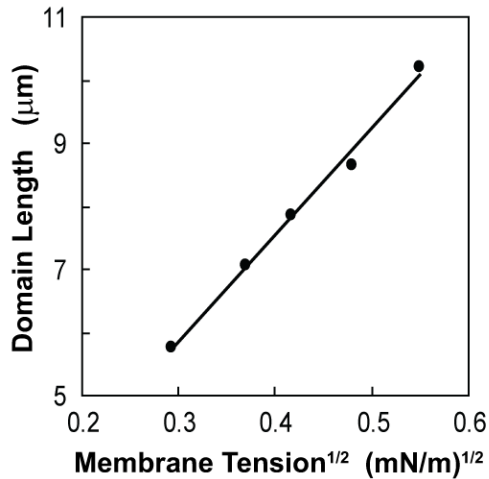

Figure 5.7: Areas of intra-tube (secondary) domains are not affected by curvature. A domain which was pulled entirely into the tube was modulated in radius and, therefore, length by changing the reservoir tension. Slope of linear fit (thick line) is proportional to domain area, and the fit extrapolates to near-zero for vanishing lateral tension, i.e. zero curvature and infinite radius. The constant slope and zero intercept agree with the prediction of constant domain area (and bending stiffness) under changing curvature for secondary domains.

Note that the tube shape series shown in Figure 5.5A-C leads to a surprising result: Despite the narrower radius of the invading Ld phase relative to the Lo phase, the total tube volume actually increases with domain growth. This occurs because of the accompanying decrease in membrane tension of both phases within the tube, which leads to larger radii within each phase. The increase in volume comparing the shapes in Figures 5.5A and C was greater than 50%. Therefore, any frictional effects of water on the domain growth would presumably serve to increase the rate rather than decrease it. Furthermore, such an effect would depend on the total tube length, though no such dependence was observed for domain growth rates in experiments (see Figures 5.2F and 5.3A). Hydrodynamic frictional effects were therefore not considered to measurably contribute to the domain growth/tube force decay dynamics.

In addition to the bending stiffness ratio ε, we measured the line tension T (0.16 ± 0.06 pN; see Chapter 3). We then calculated numerical shape series for lateral tensions varying over a range matching the experimentally considered reservoir tensions (see Figure 5.2) and the measured values for ε and T. We implemented our transport model (Equation 4.1) in differential form $dZ_0 = \left(AC^2/2Z_0\right)dt$, to calculate a time axis for the change of geometric and mechanical quantities, taking into account the changing curvature at the intra-tube phase boundary during domain growth and choosing a value of A common to all shapes considered. Figure 5.8 shows domain length vs. time (Figure 5.8A), domain length vs. $\sqrt{t}$ (Figure 5.8B), pulling force vs. time (Figure 5.8C), and pulling force vs. domain length (Figure 5.8D), confirming several aspects of the experimental measurements shown in Figure 5.2. For the (small) influence of line tension, see Figure 5.9.
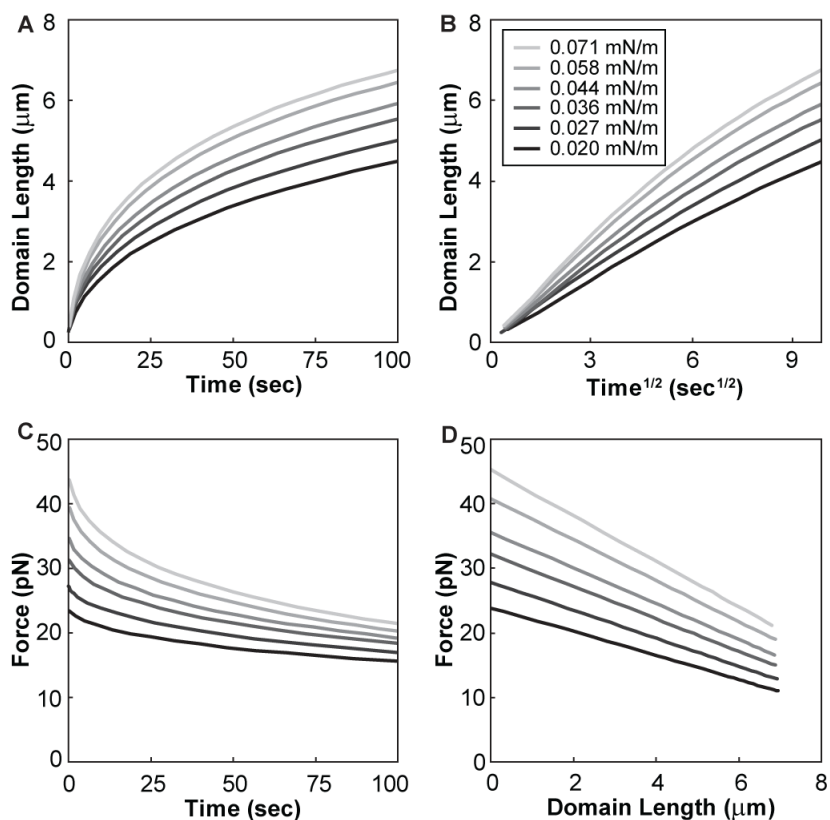
114

Figure 5.8: Geometric and mechanical domain growth data obtained from computational shape series are similar to experimental data. Total tube length was fixed at 10 μm for all calculated shapes. *A*) Domain length as a function of time for six different membrane tensions; legend in panel *B*) applies to panels *A-D*). Time axes were obtained in an iterative fashion from analytical irreversible thermodynamics model, considering leading-edge domain boundary curvature and the total domain length obtained from shapes such as displayed in Fig. 4. The parameter *A* was chosen to be $6.67 \cdot 10^{-4}$ $\mu m^4/s$, in order to approximate experimental time axes (Fig 2). Calculations assume bending stiffnesses for Lo and Ld phases of 364 pN·nm and 81 pN·nm, respectively, corresponding to experimentally measured values. Line tension assumed here is 0.16 pN, as measured in phase-separated vesicles with the same composition as used for domain growth

experiments. Gaussian bending stiffness difference is assumed to be zero. *B*) Domain

length as a function of the square-root of time; roughly linear relationships are observed

(at small observation times). *C*) Time dependence of tube force. *D*) Calculated tube force

shows a linear dependence on domain length, regardless of applied membrane tension, in

agreement with experiments (compare to Figure 5.2D).
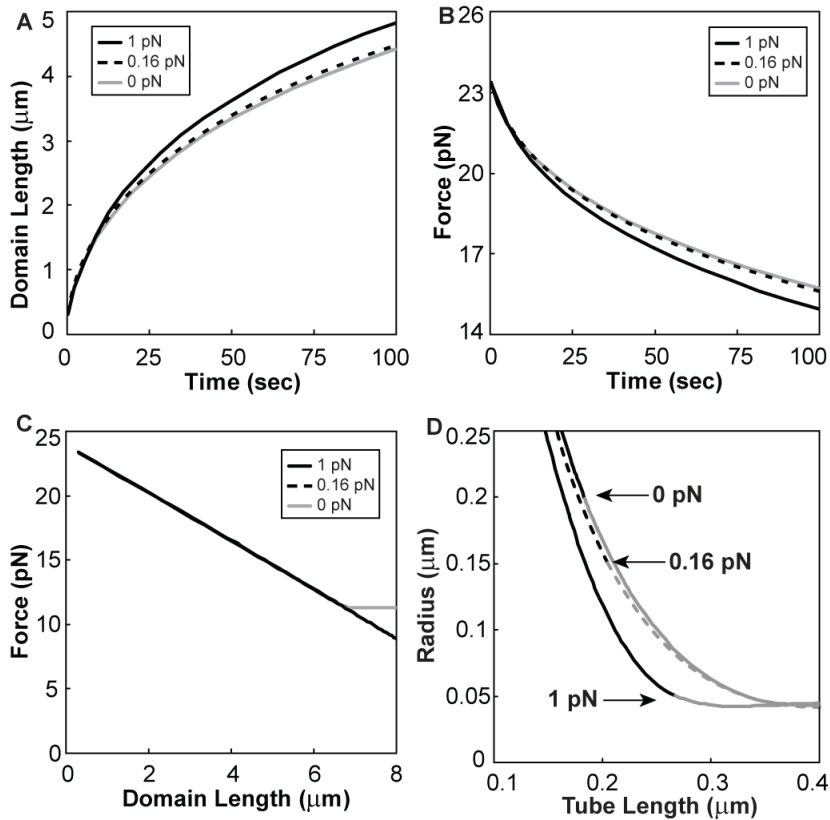
Figure 5.9: Exact values of line tensions have small effects on calculated shapes. All tube

shapes were calculated assuming a total tube length of 10 μm, lateral tension was 0.020

mN/m, and the parameter *A* was chosen to be $6.67 \cdot 10^{-4}$ μm^4/s. *A)* Domain length versus

time for three different line tensions: vanishing (0 pN), experimentally measured (0.16

pN), and large (1pN). *B)* Tube force versus time, conditions identical to *A)*. *C)* Tube force

versus domain length. Remarkably, force/domain length relation is essentially identical before the force plateau, but differs for longer domain lengths. The force decay is larger in the presence of line tension, because line tension contributes an additional lateral tension jump(*16, 19*). D) Effect of line tension on location of vesicle/tether phase boundary. Magnified view of tube neck is taken from shapes with equivalent domain lengths of 6.8 μm, close to the force plateau region. Ld phase: gray lines, Lo phase: black. Large line tension is observed to pin the vesicle/tube phase boundary at the tether neck.

Note that details of computed shape series differ from the experimental data. Among these are the lateral tension dependence of the slopes of the plots in Figure 5.8D (compare Figure 5.2D), and the linearity of rescaled domain growth time axes (compare Figure 5.2B and Figure 5.8B) for high lateral tensions. These differences likely result from the simplifications of our mechanical and transport models. Improvements may involve phase-field modeling(*21*) or dissipative particle dynamics simulations(*22*), which are beyond the scope of the present work. We note that further support for our mechanical model may be obtained in future experiments where pulling force is clamped due to continuous tether elongation and feedback.

Significance of Reported Results

The squared slopes in Figure 5.2B can be interpreted as curvature-dependent interdiffusion coefficients. Table 5.2 shows that their magnitude (0.1-10 μm2⁄s) is in the range of typical lipid diffusion coefficients [from fluorescence correlation spectroscopy (*10*)]. Interestingly, comparing the lateral tension dependence of the slopes of plots

117

such as in Figure 5.2B to our transport model (see Chapter 3 and Equation 4.1) suggests that the transport coefficient *A* increases systematically with increasing curvature. This follows from the exponent of 0.62 ± 0.08 obtained from Fig. 2E, compared to the value of 0.5 expected from Equation 4.1. Membrane curvature-dependent diffusion coefficients have been considered in single component membranes before (*23*) and here are likely influenced by the curvature dependence of the concentration profiles in the tube Ld phase (see Figure 3.8).

Our findings suggest a mechanism for intracellular sorting that uses the speed of membrane extraction from a donor reservoir (organelle) as a means for sorting. If high curvature tubes form slowly (speeds slower than 0.04 μm⁄s for this lipid composition) from a reservoir of essentially flat membranes, then equilibration of chemical potentials between the extracted sheet and the donor organelle is facilitated; in this case, the extracted membranes may show enrichment in Ld lipids and Ld proteins. If, however, membrane patches are extracted quickly (speeds faster than 1.5 μm⁄s for this lipid composition), then equilibration may be prevented and Lo rather than Ld membranes may be extracted from the reservoir. Both pulling speeds are well within a range of trafficking speeds of intracellular cargo membranes (*24*).

References

1.   Esposito, C., Tian, A., Melamed, S., Johnson, C., Tee, S. Y., and Baumgart, T. (2007) Flicker spectroscopy of thermal lipid bilayer domain boundary fluctuations, *Biophys. J. 93*, 3169.
2.   Hochmuth, R. M., Wiles, H. C., Evans, E. A., and McCown, J. T. (1982) Extensional flow of erythrocyte membrane from cell body to elastic tether. II. Experiment, *Biophys. J. 39*, 83.
3.   Tian, A., Capraro, B. R., Esposito, C., and Baumgart, T. (2009) Bending Stiffness Depends on Curvature of Ternary Lipid Mixture Tubular Membranes,

Biophys .J. 97, 1636.

4. Veatch, S. L., and Keller, S. L. (2003) Separation of liquid phases in giant vesicles of ternary mixtures of phospholipids and cholesterol, *Biophys. J. 85*, 3074.

5. Allain, J. M., Storm, C., Roux, A., Amar, M. B., and Joanny, J. F. (2004) Fission of a multiphase membrane tube, *Phys. Rev. Lett. 93*, 158104.

6. Tian, A., and Baumgart, T. (2009) Sorting of Lipids and Proteins in Membrane Curvature Gradients, *Biophys .J. 96*, 2676.

7. Sorre, B., Callan-Jones, A., Manneville, J. B., Nassoy, P., Joanny, J. F., Prost, J., Goud, B., and Bassereau, P. (2009) Curvature-driven lipid sorting needs proximity to a demixing point and is aided by proteins, *Proc. Natl. Acad. Sci. U.S.A. 106*, 5622.

8. Roux, A., Cuvelier, D., Nassoy, P., Prost, J., Bassereau, P., and Goud, B. (2005) Role of curvature and phase transition in lipid sorting and fission of membrane tubules, *EMBO J. 24*, 1537.

9. Yuan, J., Hira, S. M., Strouse, G. F., and Hirst, L. S. (2008) Lipid bilayer discs and banded tubules: Photoinduced lipid sorting in ternary mixtures, *J. Am. Chem. Soc. 130*, 2067.

10. Scherfeld, D., Kahya, N., and Schwille, P. (2003) Lipid dynamics and domain formation in model membranes composed of ternary mixtures of unsaturated and saturated phosphatidylcholines and cholesterol, *Biophys .J. 85*, 3758.

11. Mukherjee, S., and Maxfield, F. R. (2000) Role of membrane organization and membrane domains in endocytic lipid trafficking, *Traffic 1*, 203.

12. Evans, E. A., and Yeung, A. (1994) Hidden dynamics in rapid changes of bilayer shape, *Chem. Phys. Lipids 73*, 39.

13. Rozycki, B., Weikl, T. R., and Lipowsky, R. (2008) Stable patterns of membrane domains at corrugated substrates, *Phys. Rev. Lett. 100*, 098103.

14. Stefan, J. (1891) Ueber die theorie der eisbildung, insbesonder uber die eisbildung im polarmeere, *Ann. Phys. 278*, 269.

15. De Groot, S. R., and Mazur, P. (2963) *Non-Equilibrium Thermodynamics*, North-Holland Publishing Company, Amsterdam.

16. Julicher, F., and Lipowsky, R. (1996) Shape transformations of vesicles with intramembrane domains, *Phys. Rev. E 53*, 2670.

17. Derenyi, I., Julicher, F., and Prost, J. (2002) Formation and Interaction of Membrane Tubes, *Phys. Rev. Lett. 23*, 238101.

18. Bozic, B., Svetina, S., and Zeks, B. (1997) Theoretical analysis of the formation of membrane microtubes on axially strained vesicles, *Phys. Rev. E 55*, 5834.

19. Baumgart, T., Das, S., Webb, W. W., and Jenkins, J. T. (2005) Membrane elasticity in giant vesicles with fluid phase coexistence, *Biophys. J. 89*, 1067.

20. Semrau, S., Idema, T., Holtzer, L., Schmidt, T., and Storm, C. (2008) Accurate determination of elastic parameters for multicomponent membranes, *Phys. Rev. Lett. 100*, 088101.

21. Lowengrub, J. S., Ratz, A., and Voigt, A. (2009) Phase-field modeling of the dynamics of multicomponent vesicles: Spinodal decomposition, coarsening, budding, and fission, *Phys. Rev. E 79*, 031926.

22. Illya, G., Lipowsky, R., and Shillcock, J. C. (2006) Two-component

membrane material properties and domain formation from dissipative particle dynamics, *J. Chem. Phys. 125*, 114710.

23. Daniels, D. R., and Turner, M. S. (2007) Diffusion on membrane tubes: A highly discriminatory test of the Saffman-Delbruck theory, *Langmuir 23*, 6667.

24. Kural, C., Kim, H., Syed, S., Goshima, G., Gelfrand, V. I., and Selvin, P. R. (2005) Kinesin and dynein move a peroxisome in vivo: A tug-of-war or coordinated movement?, *Science 308*, 1469.

Table 5.1 – Tie-line compositions yielding homogenous vesicles from which bending

stiffnesses (κ) of the Lo and Ld phases were determined

Composition	DPPC	DOPC	Chol	κ (10^{-19} J)
Lo1	52%	11	37	4.2±0.9 (N=17)
Lo2	48%	13	39	3.2±0.7 (N=17)
Lo3	46%	12	42	4.2±0.6 (N=24)
Lo4	42%	15	43	4.0±0.7 (N=18)
Lo5	39%	17	44	2.7±0.2 (N=19)
Ld1	18	68	14	0.82±0.06 (N=16)
Ld2	17	66	17	0.87±0.08 (N=18)
Ld3	16	64	20	0.73±0.09 (N=15)
Ld4	17	60	23	0.71±0.06 (N=16)
Ld5	17	57	26	0.94±0.12 (N=17)

Table 5.2 – Experimentally measured diffusion coefficients depend on membrane tension

Vesicle	Membrane Tension (mN/m)	Diffusion Coefficient (μm^2/s)
A	0.020±0.003	0.18±0.01
A	0.027±0.005	0.30±0.01
A	0.036±0.006	0.38±0.02
A	0.044±0.008	0.59±0.02
A	0.058±0.010	0.76±0.02
A	0.071±0.011	1.42±0.03
B	0.063±0.011	0.16±0.01
B	0.083±0.014	0.41±0.02
B	0.11±0.02	0.71±0.02
B	0.13±0.02	1.10±0.02
C	0.023±0.004	0.15±0.01
C	0.053±0.009	0.71±0.02
C	0.09±0.02	1.32±0.03
D	0.054±0.009	0.10±0.01
D	0.072±0.012	0.19±0.01
D	0.09±0.02	0.26±0.01
D	0.10±0.02	0.48±0.02
D	0.12±0.02	0.71±0.02
D	0.15±0.03	1.30±0.03
E	0.056±0.009	0.26±0.01
E	0.075±0.013	0.95±0.02

Chapter 6: Curvature Sorting and Generation by Protein

Measurements described below concern the curvature sensing and generation of the protein domain DA-N-BAR. The resulting preferential sorting of the protein into high curvature membranes in the tube-pulling assay stands in contrast to the behavior of CTB, which is known(*1-2*) to actively sort into flat membranes. In Chapter 5, the CTB/GM1 complex could be induced to persist in pulled tubes through the combination of the Lo phase preference, rapid pulling speeds, and a nucleated Ld phase domain which served as a diffusion barrier. In Chapter 6, however, it is the curvature preference of DA-N-BAR itself that drives the resulting increase in concentration on pulled tubes. Furthermore, the ability of DA-N-BAR to generate curvature is quantitatively assessed over a range of concentrations.

Curvature Sorting of *Drosophila* Amphiphysin N-BAR Domain

Hypothesized Protein Interaction with Curved Membrane

In order to quantify the ability of the N-BAR domain to stabilize curved membrane tubules, we have incubated giant unilamellar vesicles (GUVs) with *Drosophila* amphiphysin and, using classical pipette-aspiration(*3*) with an optical trap(*4-5*), measured the force necessary to pull and then maintain a tube at equilibrium (Figure 6.1). For single-component lipid vesicles, it is well-established that the tube force arises from the bending energy at the curvature of the tube as regulated by the vesicle membrane tension (*6*). Molecules which act as curvature generators are hypothesized to effectively lower the bending energy(*2, 7*) by, in the case of the scaffolding amphiphysin, forming a lattice(*8*) surrounding the tubulated membrane. Note that tube bending

122

energy can also be lowered in the case of lipid sorting both near(*2, 9*) and inside of(*4*) a critical demixing boundary; however, the lipid compositions used here do not reflect such conditions. Instead, reduced tube forces were observed when tubes were pulled from GUVs in the presence of the N-BAR domain of *Drosophila* amphiphysin (DA-N-BAR). An effective spontaneous curvature could then be determined through measurements of the static (equilibrium) tube force needed to maintain the protein-bound tube at fixed length; see Chapter 3.
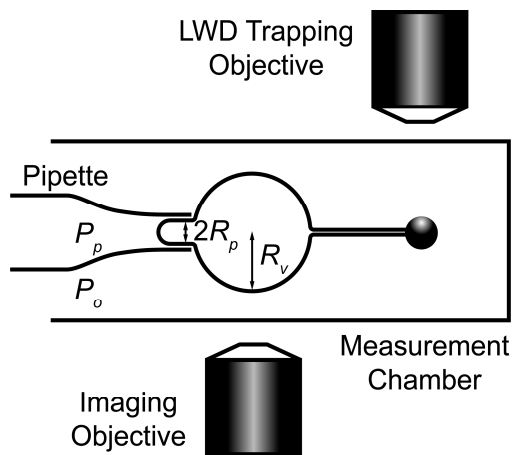

Figure 6.1: Schematic of experimental setup for membrane tube pulling force measurements showing: micropipette (with inner radius R_p) used to fix vesicle (radius R_v) membrane tension via aspiration pressure difference P_o-P_p; streptavidin-conjugated microsphere held by optical trap formed via a long-working distance (LWD) objective; and, tube resulting from retraction of bead after contact with vesicle.

Fluorescently-Labeled Protein Indicates Reversible Curvature Sorting

Curvature sorting of the N-BAR domain from *Drosophila* amphiphysin was first investigated with a fluorescently-labeled variant that was incubated with GUVs formed from the ternary lipid mixture DOPC/Chol/DOPS with the molar mixing fractions 77/3/20. Vesicles were symmetrically labeled with the curvature-insensitive lipid fluorophore Texas Red-DHPE(*1, 4*). In order to generate connected and equilibrated regions of high and low curvature lipid membrane, cylindrical tubes were pulled from pipette-aspirated vesicles(*3*). Pipette aspiration achieves control of vesicle membrane tension, which along with the bending stiffness adjusts the radius of a pulled tube (see Chapter 3). Figure 6.2A shows the collected fluorescence from lipid and protein channels along the tube as well as part of the attached vesicle. Because the xyz-dimensions of the optical microscope's focal volume are larger than the diameter of the tube (on the order of 10-100 nm), it is to be expected that the lipid signal on the tube is smaller than on the vesicle, assuming a constant fluorophore density(*1*). However, it is apparent that this is not the case in the protein channel, where the relatively equal intensities of the tube and vesicle regions indicate a higher density of protein on the tube, compared to the attached vesicle.
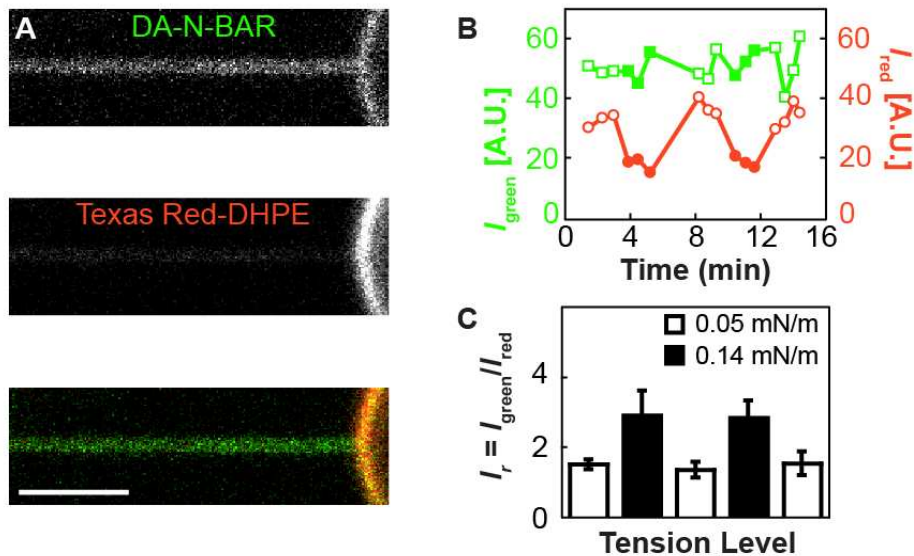
Figure 6.2: DA-N-BAR localization between connected membranes of different curvature. A). Top, green confocal channel detecting fluorescence from Alexa Fluor 488-labeled DA-N-BAR. Middle, red channel detecting Texas Red-DHPE fluorescence. Bottom, merged. Lateral tension σ = 0.05 mN/m. Vesicle composition is DOPC with 20% DOPS and 3% Chol, and protein solution concentration is 0.23 μM, with 15 mM NaCl. B) Tube fluorescence from components indicated in (A) (red and green points), for a vesicle with composition 86% DOPC, 11% DOPS and 3% Chol, is monitored as variations in the membrane tension [filled points indicate increased tension level; values in (C)] modulate the curvature of the tube (see Chapter 3 for details). Whereas the lipid fluorescence decreases as tube curvature is increased(*1, 10*), the DA-N-BAR fluorescence remains roughly constant over the tension levels considered. C) The ratio of fluorescence intensities from (B), $I_r = I_{green}/I_{red}$, is averaged over 3-4 *xz* scans for each tension level. Error bars indicate SD. The *p*-value from Student's *t*-test comparing all low (open bars) to all high (filled bars) tension I_r values is 1.1x10^{-3}. The *p*-values corresponding to comparisons of I_r between consecutive segments of the cyclic tension change

125

protocol are 0.077, 0.057, 0.022, and 0.025. Thus, I_r values respond with statistical significance to changes in membrane tension.

This high-curvature preference of DA-N-BAR is quantified in Figure 6.2C, where the intensities from each fluorophore on the tube were measured for a cycle of vesicle membrane tensions. The lipid signal responds as expected: increasing the membrane tension leads to a smaller tube radius, thereby reducing the number of imaged fluorophores. The curvature preference of the protein is demonstrated by the absence of a drop in intensity, which can be interpreted as a further increase in density concurrent to the decrease in tube area. This is quantified through the ratio of protein to lipid fluorescence intensities I_r, which follows the changes in applied vesicle tension.

Curvature Generation by Drosophila Amphiphysin N-BAR Domain

Tube Force is Lowered in Presence of Protein

In addition to its curvature preference, the N-BAR domain can also act as a curvature generator(*11*). The efficacy of membrane curvature generation and its dependence on protein solution concentration were investigated by measuring the force necessary to mechanically equilibrate tubes pulled from giant vesicles. Tubes pulled from single-phase vesicles with compositions far from a demixing boundary require a constant pulling force that is determined by the vesicle membrane tension (as set by the pipette aspiration) and the vesicle bending stiffness(*9*). The vesicles here used, in absence of protein, followed this trend (data not shown). However, tubes pulled from vesicles that were incubated with DA-N-BAR were observed to require a maintenance force

(tube force) that decreased over time immediately after pulling the tube. Figure 6.3A highlights three example force curves for vesicles incubated with three different solution concentrations of DA-N-BAR. Each equilibrium tube force, reached after tens of seconds, was measured to be lower than the initial tube force. This behavior deviates significantly from pulling forces measured with tubes incubated with the protein dynamin(*12*). Dynamin has been observed to polymerize on tubular membranes in a curvature-dependent manner(*12*). Polymerization has been shown to generate a polymerization force that is revealed as an abrupt decrease in tube pulling force once the tubular membrane becomes completely covered by dynamin(*12*). Accordingly, the slow changes in pulling force after tube extension revealed in Figure 6.3A suggest a different mechanism for pulling force reduction by DA-N-BAR compared to dynamin. We interpret the time-dependent pulling force decay as a concomitant increase in the protein density on the tube compared to the initial lower density of the vesicle it was pulled from, as evidenced by the tubular enrichment in Figure 6.2A.
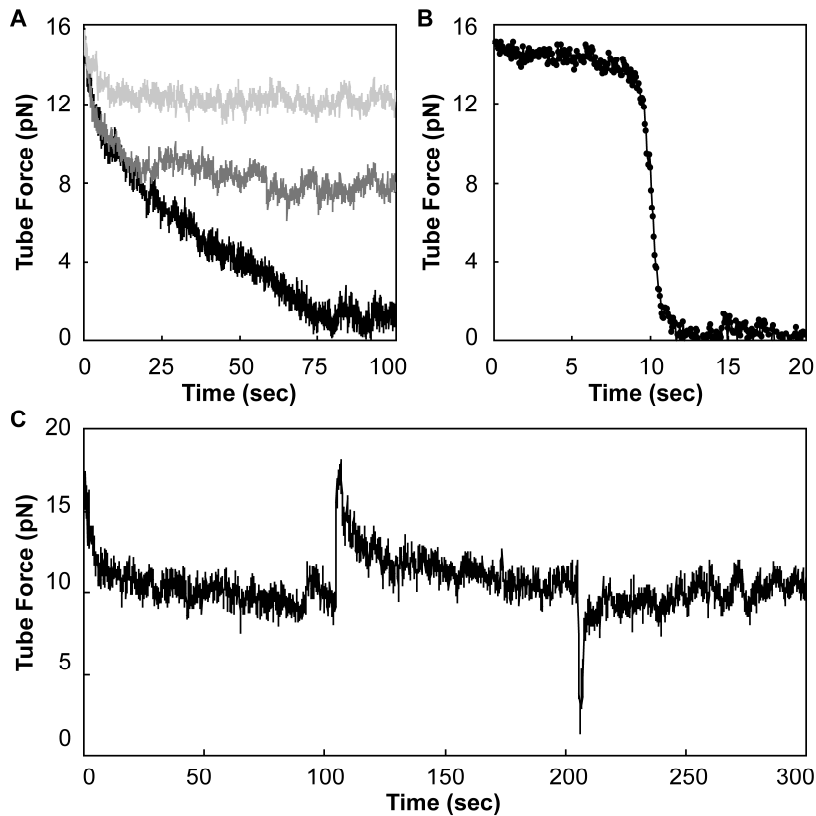
Figure 6.3: Tube pulling force is lowered by DA-N-BAR. For all results shown, vesicle membrane tension was fixed at 0.03±0.005 mN/m. A) Tube forces decreased over time for three vesicles incubated with DA-N-BAR at concentrations of 0.11 (light gray), 0.33 (gray), and 0.39 μM (black). Zero time is immediately after pulling a tube with a length of 20 μm from each vesicle. B) A tube is pulled from a vesicle in the absence of DA-N-BAR after which protein is injected into the measurement chamber. An initially constant force is observed before protein injection. After protein injection, tube force drops to near-zero. C) Equilibrium tube forces were observed following reversible tube length changes from the initial length of 20 μm at $t = 0$ s to 40 μm with a speed of 10 μm/s at $t = 105$ s and a subsequent return to 20 μm at $t = 205$ s. Vesicle was incubated with 0.33 μM DA-N-BAR.

Tube Length Can Be Reversibly Changed at Low Protein Concentration

In Figure 6.3B, a tube pulled from a vesicle in the absence of DA-N-BAR required constant force until the protein was injected into the chamber at a nominal solution concentration of 1.4 µM. Following injection, tube force was observed to markedly decrease to a near-zero equilibrium value; this is in qualitative agreement with the spontaneous tubulation of liposomes(*13*).

At lower protein concentrations, tube length could be changed reversibly. In Figure 6.3C, the tube force of a vesicle incubated with DA-N-BAR was measured to decrease following initial formation, as in Figure 6.3A. After ~100 s of equilibration, the tube was extended from 20 to 40 µm in length in 2 s. The tube force correspondingly increased sharply to near the initial value, then decreased again in similar manner to the first decay but at a somewhat higher equilibrium force(*14*). A subsequent decrease in tube length (from 40 to 20 µm) led to a rapid drop in the tube force; the ensuing reestablishment of the minimum force value first measured demonstrates mechanical and compositional equilibrium.

Tube Force Dependence on Protein and Salt Concentration

As was indicated by Figure 6.3A, the equilibrium tube force was observed to depend on the protein solution concentration that vesicles were incubated in. Systematic measurements of resulting, protein-equilibrated tube forces are shown in Figure 6.4A. Equilibrium tube forces consistently decreased with increases in DA-N-BAR solution concentration. Sufficiently high concentrations of protein led to near complete loss of tube force, as expected for a protein with tubulation activity.
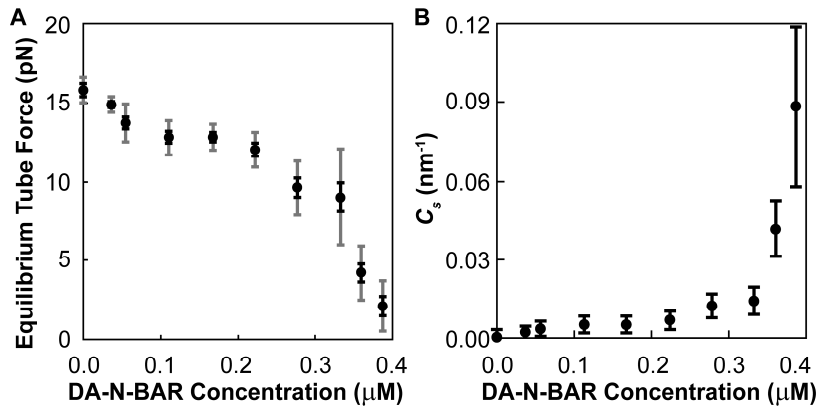
Figure 6.4: Reductions in tube force depend on DA-N-BAR concentration. A) Average equilibrium tube force decreases non-linearly with DA-N-BAR incubation concentration. Averages are taken of 8-10 vesicle/tube pairs at each concentration; SEMs are shown in black, SDs are shown in gray. Each vesicle membrane tension was kept constant at 0.03±0.005 mN/m. Tubes were pulled to 20 μm at 10 μm/s and equilibrium forces were measured after 200 s. B) Effective spontaneous curvatures calculated using equilibrium tube forces in A) and Eq 3. Error bars represent propagated SEMs from force measurements in A) and uncertainties in bending stiffness and lateral tension.

For the measurements shown in Figure 6.4, salt concentrations were kept low in order to promote binding of DA-N-BAR to the negatively-charged vesicles, ranging between 21 and 27 mM. Over this range and a fixed DA-N-BAR solution concentration, no trend in the resulting equilibrium tube forces could be found. However, even higher salt levels led to higher equilibrium tube forces, likely indicating reduced binding of protein to the tubular membrane due to electrostatic screening. Increasing the salt concentration to 150 mM in the 0.28 μM DA-N-BAR chamber increased the equilibrium tube force to 11.4±0.7 pN, while an even larger increase to 432 mM salt nearly

130

abolished the force reduction, with equilibrium tube forces approaching the bare tube force. More systematic investigations of salt effects are not here considered, but could be studied using such tube force measurements.

Calculation of Effective Spontaneous Curvature of Protein

As a starting point in understanding the lowered equilibrium tube force dependence on solution concentration of DA-N-BAR, we model our membrane as a homogenous tube partially covered with protein such that the tube adopts an effective spontaneous curvature C_s, the value of which depends on the curvature and membrane binding density of the protein; see Chapter 3. Minimizations of the free energy of such a tube with respect to the radius and length led to a C_s-dependent tube force f:

$$f = 2\pi\sqrt{2\sigma\kappa + \kappa^2 C_s^2} - 2\pi\kappa C_s \qquad\qquad (6.1)$$

where κ is the membrane bending stiffness and σ is the lateral tension. Equivalently, Equation 6.1 can be expressed as force-dependent spontaneous curvature as:

$$C_s = \frac{8\pi^2\sigma\kappa - f^2}{4\pi\kappa f} \qquad\qquad (6.2)$$

With the aid of Equation 6.2, we calculated an effective spontaneous curvature from measurements of equilibrium tube force as a function of protein solution concentrations (Figure 6.4B). Membrane tension and bare tube bending stiffness were measured as described previously(*4-5*) and were assumed to remain constant at 0.03±0.005 mN/m and 108±7 pN·nm (measured on 5 vesicles in absence of DA-N-BAR), respectively, for all DA-N-BAR solution concentrations. The assumption of tube bending stiffness being unaffected by protein binding has previously been made(*12*). In light of theoretical

predictions for membrane inserting peptides(*15*), and experimental measurements involving the peripheral protein Sar1(*16*), this assumption needs to be carefully tested in future measurements. From Figure 6.4B we conclude that, for the highest solution concentrations, spontaneous curvatures on the order of 10 nm are found, consistent with the molecular curvature of the DA-N-BAR domain(*11*).

We note that the curvature sorting of DA-N-BAR observed in Figure 6.2 leads to a transition region between high protein density on the tube and low density on the vesicle. In the presence of a sharp phase boundary, we have recently shown that its exact position within the high curvature neck region influences the measured pulling forces(*4*). Future research will assess the possible contribution of this effect on the measurements shown here.

To summarize, we have found systematic solution concentration dependence of the spontaneous curvature conferred by DA-N-BAR. We note that evidence for intramolecular inhibition of N-BAR domain membrane binding by the SH3 domain of full length amphiphysin exists(*17-18*). Future experiments therefore will have to address the role of the SH3 domain on membrane curvature sensing and generation by amphiphysin and related BAR domain proteins.

We also note that discrepancies have arisen in recent theoretical work pertaining to the role of the N-terminal amphipathic helix H0 found in N-BAR domains (but not in all BAR domains) in achieving the membrane bending observed for proteins such as amphiphysin(*19-20*). We expect that quantitative measurements of membrane curvature generation, such as shown here, comparing different types of BAR domains and their mutants, will help elucidate mechanisms underlying BAR domain function.

References

1. Tian, A., and Baumgart, T. (2009) Sorting of Lipids and Proteins in Membrane Curvature Gradients, *Biophys .J. 96*, 2676.
2. Sorre, B., Callan-Jones, A., Manneville, J. B., Nassoy, P., Joanny, J. F., Prost, J., Goud, B., and Bassereau, P. (2009) Curvature-driven lipid sorting needs proximity to a demixing point and is aided by proteins, *Proc. Natl. Acad. Sci. U.S.A. 106*, 5622.
3. Hochmuth, R. M., Wiles, H. C., Evans, E. A., and McCown, J. T. (1982) Extensional flow of erythrocyte membrane from cell body to elastic tether. II. Experiment, *Biophys. J. 39*, 83.
4. Heinrich, M. C., Tian, A., Esposito, C., and Baumgart, T. (2010) Dynamic sorting of lipids and proteins in membrane tubes with a moving phase boundary, *Proc. Natl. Acad. Sci. U.S.A. 107*, 7208.
5. Cuvelier, D., Derenyi, I., Bassereau, P., and Nassoy, P. (2005) Coalescence of membrane tethers: Experiments, theory, and applications, *Biophys. J. 88*, 2714.
6. Derenyi, I., Julicher, F., and Prost, J. (2002) Formation and Interaction of Membrane Tubes, *Phys. Rev. Lett. 23*, 238101.
7. Leibler, S. (1986) Curvature instability in membranes, *J. Phys. 47*, 507.
8. Frost, A., Perera, R., Roux, A., Spasov, K., Destaing, O., Egelman, E. H., De Camilli, P., and Unger, V. M. (2008) Structural basis of membrane invagination by F-BAR domains, *Cell 132*, 807.
9. Tian, A., Capraro, B. R., Esposito, C., and Baumgart, T. (2009) Bending Stiffness Depends on Curvature of Ternary Lipid Mixture Tubular Membranes, *Biophys .J. 97*, 1636.
10. Capraro, B. R., Yoon, Y., Cho, W., and Baumgart, T. (2010) Curvature sensing by the epsin N-terminal homology domain measured on cylindrical lipid membrane tethers, *J. Am. Chem. Soc. 132*, 1200.
11. Peter, B. J., Kent, H. M., Mills, I. G., Vallis, Y., Butler, P. J. G., Evans, P. R., and McMahon, H. T. (2004) BAR domains as sensors of membrane curvature: The amphiphysin BAR structure, *Science 303*, 495.
12. Roux, A., Koster, G., Lenz, M., Sorre, B., Manneville, J. B., Nassoy, P., and Bassereau, P. (2010) Membrane curvature controls dynamin polymerization, *Proc. Natl. Acad. Sci. U.S.A. 107*, 4141.
13. Takei, K., Slepnev, V. I., Haucke, V., and De Camilli, P. (1999) Functional partnership between amphiphysin and dynamin in clathrin-mediated endocytosis, *Nat. Cell Biol. 1*, 33.
14. Waugh, R. E., Song, J., Svetina, S., and Zeks, B. (1992) Local and nonlocal curvature elasticity in bilayer membranes by tether formation from lecithin vesicles, *Biophys .J. 61*, 974.
15. Zemel, A., Ben-Shaul, A., and May, S. (2008) Modulation of the spontaneous curvature and bending rigidity of lipid membranes by interfacially adsorbed amphipathic peptides, *J. Phys. Chem. B 112*, 6988.
16. Settles, E. I., Loftus, A. F., McKeown, A. N., and Parthasarathy, R. (2010) The vesicle trafficking protein Sar1 lowers lipid membrane rigidity, *Biophys .J. 99*, 1539.

17. Rao, Y. J., Ma, Q. J., Vahedi-Faridi, A., Sundborger, A., Pechstein, A., Puchkov, D., Luo, L., Shupliakov, O., Saenger, W., and Hauke, V. (2010) Molecular basis for SH3 domain regulation of F-BAR-mediated membrane deformation, *Proc. Natl. Acad. Sci. U.S.A. 107*, 8213.

18. Farsad, K., Slepnev, V. I., Ochoa, G., Daniell, L., Haucke, V., and De Camilli, P. (2003) A Putative Role for Intramolecular Regulatory Mechanisms in the Adaptor Function of Amphiphysin in Endocytosis, *Neuropharmacology 45*, 787.

19. Arkhipov, A., Yin, Y., and Schulten, K. (2009) Membrane-Bending Mechanism of Amphiphysin N-BAR Domains, *Biophys. J. 97*, 2727.

20. Campelo, F., McMahon, H. T., and Kozlov, M. M. (2008) The hydrophobic insertion mechanism of membrane curvature generation by proteins, *Biophys. J. 95*, 2325.

Chapter 7: Conclusions and Outlook

Line Tension and Dipole Density Difference in Lipid Monolayers

Monolayers exhibiting phase separation into the biologically-relevant Lo and Ld phases were prepared at the critical composition 30% DChol / 70% DMPC as well as two other compositions: 35% DChol / 65% DMPC and 40% DChol / 60% DMPC. The thermally-induced domain boundary fluctuations were imaged and analyzed via two distinct theoretical descriptions. First, capillary wave theory developed by Goldstein and Jackson(*1*) was applied to determine line tension and dipole density concurrently from time-averaged mode powers. The critical exponents describing their surface pressure dependence was determined and found in good agreement with previous estimates. Also, the (dipole density difference-reduced) effective line tension was calculated for comparison with previous studies. These values were similar to those determined by McConnell(*2*), but not to the more recently published values by Stottrup(*3*). Second, a hydrodynamic time-decay theory was used to analyze the critical composition data set, but difficulties in determining the (and limiting inclusion to) well-resolved fluctuation modes resulted in less reliable estimates of line tension and dipole density difference. Finally, preliminary results on the inclusion of the suspected linactant lysoPC were presented. The addition of lysoPC at amounts of 0.5% (lipid mol fraction) led to visibly altered domain boundaries, while a smaller addition of 0.1% resulted in domains which were still circular. These domains exhibited boundary fluctuations that indicated significantly reduced line tensions as measured using the capillary wave theory. However, some reduction in dipole density difference was also obtained, despite the expectation of minimal change to the bulk properties of the composition by the

dopant. Despite these concerns, the method of flicker spectroscopy combined with capillary wave theory shows promise in future work where accurate measurements of line tension-modulating species are required.

Lipid Curvature Sorting by Bending Stiffness in Lipid Bilayers

Giant unilamellar vesicles exhibiting phase separation into the biologically relevant Lo and Ld phases were used to pull thin cylindrical tubes from the Lo phase, distinguishable from the Ld phase by its higher bending stiffness. Ld phase domains were observed to nucleate exclusively at the vesicle/tube neck, and then to grow in length with a square-root time dependence. Concurrently, the tube force as measured with an optical trap was found to decrease in linear proportion to the length of the nucleated domain. Furthermore, the domain growth and tube force decays were found to depend on the tube curvature as adjusted through the vesicle membrane tension, but they were independent of the total tube length. Domain nucleation and growth was distinguished from the separate occurrence of pre-existing domain diffusion into the tube. To understand the time-dependence observed, a mass transport theory was developed on the basis of a chemical potential difference gradient motivated by the higher bending stiffness in the Lo phase region of the tube. This theory predicted domain length to depend on both curvature and the square-root of time. In order to understand the simultaneous force decay, however, we turned to numerical solutions of tube shapes to model the neck region of the vesicle/tube system. These calculations agreed with the experimental observation of a linear reduction in tube force with increase in tube length, where the tube domain boundary near the neck was predicted to gradually move into the low-

curvature region of the vesicle in order to reduce the membrane tension in the Ld phase (and, subsequently, the membrane tension in the Lo phase of the tube), thereby reducing the force. Combining the mass transport theory and the numerical shape solutions led to reasonably good predictions of the time-dependence of domain length and tube force in qualitative agreement with our experimental results. Finally, experimental evidence was shown that tube composition could be selected between Lo and Ld phase through fast or slow tube formation at rates of 0.04 μm/s or 1.5 μm/s, respectively, both of which are within range of trafficking speeds of intracellular cargo membranes.

Protein Curvature Sorting and Generation in Lipid Bilayers

The curvature sorting and generation of the *Drosophila* amphiphysin N-BAR domain was investigated by incubating it with homogenous giant unilamellar vesicles from which were pulled tubes of fixed length. Following formation, tube forces were consistently observed to decrease over time to lower equilibrium values. These values depended systematically on the nominal solution concentration of the protein, and decreased towards zero as concentrations were increased to near 0.4 μM. Furthermore, tubes formed first in the absence of protein were observed to maintain a constant (time-independent) tube force until protein was injected into the chamber. Due to relatively higher local concentrations, the resulting tube force dropped to approximately zero (within measurement error), in agreement with previously published qualitative observations of the tubulation of liposomes(*4*). In these cases, the tube length could no longer be decreased, but at lower concentrations of protein, tube lengths could be reversibly changed. The lowered equilibrium tube forces were analyzed with a

137

simple model utilizing an effective spontaneous curvature, the magnitude of which was presumed to depend on the local density of DA-N-BAR domains on the tube and, therefore, on the nominal bulk solution concentration. The effective spontaneous curvature then determined from equilibrium tube forces at the highest concentrations was on the order of 10 nm, which is consistent with the molecular curvature of the DA-N-BAR domain(*5*). The tube force assay enabled quantitative measurements of curvature generation by DA-N-BAR domain, building upon the qualitative evidence available previously. Future work will be able to quantitatively assess the roles of the amphipathic helix as well as the SH3 domains found in full-length amphiphysin. This will lead to greater understanding of the mechanisms underlying the functions of the numerous proteins in the BAR domain family.

References

1. Goldstein, R. E., and Jackson, D. P. (1994) Domain shape relaxation and the spectrum of thermal fluctuations in Langmuir monolayers, *J. Phys. Chem. 98*, 9626.
2. Benvegnu, D. J., and McConnell, H. M. (1992) Line tension between liquid domains in lipid monolayers, *J. Phys. Chem. 96*, 6820.
3. Stottrup, B. L., Heussler, A. M., and Bibelnieks, T. A. (2007) Determination of line tension in lipid monolayers by Fourier analysis of capillary waves, *J. Phys. Chem. B 111*, 11091.
4. Takei, K., Slepnev, V. I., Haucke, V., and De Camilli, P. (1999) Functional partnership between amphiphysin and dynamin in clathrin-mediated endocytosis, *Nat. Cell Biol. 1*, 33.
5. Peter, B. J., Kent, H. M., Mills, I. G., Vallis, Y., Butler, P. J. G., Evans, P. R., and McMahon, H. T. (2004) BAR domains as sensors of membrane curvature: The amphiphysin BAR structure, *Science 303*, 495.

Appendix A: Annotated Matlab Code

A note on formatting: The left hand entries are reserved for the actual Matlab code, which can be compiled into simple text documents and saved as a file with the file extension ".m" for use in the Matlab command line. Individual commands are distinguished by a line break (and frequently end with a semicolon to suppress output in Matlab). Lengthy single commands run onto two or more lines, but are recognizable by an indentation and an ellipsis (…) at the start of the subsequent line to indicate the continuation of the previous line. The right hand entries, meanwhile, are intended to provide useful description of the commands they accompany. Names of scripts, functions, variables, etc., within the annotations are displayed in Arial font to distinguish from comments.

Appendix A-1: Setting up the Video Input Object, Serial Port Object for Motorized Stage Control, and Analog Input Object for Pressure Measurements

```
setupvid
global vid
vid = videoinput('dt',1,'RS170');
vid.ReturnedColorSpace='grayscale';
preview(vid)
```
The script setupvid is used to create a video input object which connects to a camera wired to a Data Translation frame grabber card, making use of the 'dt' drivers. The object is assigned to a global variable for use in other functions.

```
setupstage
global s
s=serial('COM1');
fopen(s);
set(s,'Terminator','CR','BaudRate',19200);
```
The script setupstage is used to create a serial port object which connects to the motorized stage controller MS-2000 (ASI). The object is assigned to a global variable for use in other functions.

```
setuppress
global ai
ai = analoginput('mcc',0);
addchannel(ai,0:0);
ai.SampleRate=1002;
```
The script setuppress is used to create an analog input object which connects to the miniLAB 1008 (MCC). The object is assigned to a global variable for use in other functions.

Appendix A-2: Calibrating the Optical Trap Stiffness

function
stiffness=dragforce(direction,sucrose)

This function is used to calibrate the trap stiffness via the drag force method. The input direction is either the string 'x' or 'y' which specifies the motion the stage moves (typically 'x'). The input **sucrose** is a scalar to specify the sucrose concentration (molar) of the solution, which affects the value of the solution viscosity **eta** below.

global centers vid stiffness

The global variable **centers** is used for the square-wave fit below. The variable **vid** is the video input device. The variable **stiffness** is used in other functions, and needs to be consistently defined, hence it is here claimed as a global variable.
global centers vid stiffness

```
setupstage
vid.ROIPosition=[0,0,640,480];
pause(0.5)
vid.FramesPerTrigger=1;
start(vid)
frame=getdata(vid);
width=80;
height=60;
[spotx,spoty,P]=impixel(frame);
left=round(spotx-width/2);
top=round(spoty-height/2);
vid.ROIPosition=[left,top,width,height];
```

The script **setupstage** is used to initialize the serial connection to the motorized stage controller. The region-of-interest of the camera is reset, and a single image is collected. The user selects a point on that image corresponding to the center of the bead, and the ROI is cropped around that point.

```
if sucrose>0.5
   d1=900;
   d2=1800;
   d3=3600;
   v1=100;
   v2=200;
   v3=400;
else
   d1=1800;
   d2=3600;
   d3=5400;
   v1=200;
   v2=400;
   v3=600;
end
```

The sucrose concentration is used to select between two sets of velocities. Velocities need to be large enough to yield a measurable displacement, but small enough that the drag force does not exceed the characteristic escape force.

```
movie1=stagevideo(d1,v1,direction,4);
movie2=stagevideo(d2,v2,direction,4);
movie3=stagevideo(d3,v3,direction,4);
vid.ROIPosition=[0,0,640,480];
fclose(s)
```

The subfunction stagevideo is used to collect images from the video input while simultaneously moving the stage in periodic fashion. It accepts as inputs the distance, velocity, direction, and frame interval, and it outputs the recorded frames as a 4D array.

```
centers1=imagefitter(movie1);
centers2=imagefitter(movie2);
centers3=imagefitter(movie3);
r1=mean(centers1(:,3));
r2=mean(centers2(:,3));
r3=mean(centers3(:,3));
```

The subfunction imagefitter is used to determine the bead position in each frame for each movie. This function also fits for the bead radius, which is used later to determine the Stokes drag force for a sphere.

```
pixsize=227;
eta=(1.84*sucrose^2+0.32*sucrose+1.03)*10
    …^9;
radius=(r1+r2+r3)/3*pixsize*10^-9;
```

The pixel size of the image is 227 nm, but will change depending on the optics and camera used. The dynamic viscosity is determined from a polynomial fit to published experimental data over the range [0,..,1] M (Chenlo et al., 2002 Journal of Food Engineering, 54, 347), with units of pN*sec/m^2. The bead radius is determined from the average fit radii in units of m.

```
centers=centers1;
dydx=abs(centers(3:size(centers),1)-
centers(1:(size(centers,1)-2),1));
space=0;
dydx=cat(1,space,dydx,space);
left=max(centers(:,1));
middle=mean(centers(:,1));
right=min(centers(:,1));
[c,a1]=max(dydx(1:10));
[c,a2]=max(dydx(11:20)); a2=a2+10;
[c,a3]=max(dydx(21:30)); a3=a3+20;
[c,a4]=max(dydx(31:40)); a4=a4+30;
[c,a5]=max(dydx(41:50)); a5=a5+40;
[c,a6]=max(dydx(51:60)); a6=a6+50;
[c,a7]=max(dydx(61:70)); a7=a7+60;
[c,a8]=max(dydx(71:size(centers,1)));
a8=a8+70;
lmr=[left;middle;right;a1;a2;a3;a4;a5;a6;a7;a
    …8];
[lmr,fval,exitflag]=fminsearch(@dragsquarew
    …ave, lmr, optimset('TolX',1e-
    …2,'TolFun',1e-2));
drag(1,1)=(lmr(1)-lmr(2))*pixsize;
drag(2,1)=(lmr(3)-lmr(2))*pixsize;
drag(1,2)=6*pi*eta*radius*200*0.63*10^-6;
drag(2,2)=-drag(1,2);
```

The center positions from the first movie are fit to a square wave using the subfunction **dragsquarewave**, below. The positive and negative displacments in nm (from positive and negative drag velocities) are determined from the square wave fit. The corresponding drag forces (in pN) are calculated for a sphere.

```
centers=centers2;
dydx=abs(centers(3:size(centers),1)-
centers(1:(size(centers,1)-2),1));
space=0;
dydx=cat(1,space,dydx,space);
left=max(centers(:,1));
middle=mean(centers(:,1));
right=min(centers(:,1));
[c,a1]=max(dydx(1:10));
[c,a2]=max(dydx(11:20)); a2=a2+10;
[c,a3]=max(dydx(21:30)); a3=a3+20;
[c,a4]=max(dydx(31:40)); a4=a4+30;
[c,a5]=max(dydx(41:50)); a5=a5+40;
[c,a6]=max(dydx(51:60)); a6=a6+50;
[c,a7]=max(dydx(61:70)); a7=a7+60;
[c,a8]=max(dydx(71:size(centers,1)));
a8=a8+70;
lmr=[left;middle;right;a1;a2;a3;a4;a5;a6;a7;a
    ...8];
[lmr,fval,exitflag]=fminsearch(@dragsquarew
    ...ave, lmr, optimset('TolX',1e-
    ...2,'TolFun',1e-2));
drag(3,1)=(lmr(1)-lmr(2))*pixsize;
drag(4,1)=(lmr(3)-lmr(2))*pixsize;
drag(3,2)=6*pi*eta*radius*200*0.63*10^-6;
drag(4,2)=-drag(3,2);
```

The center positions from the second movie are fit to a square wave using the subfunction **dragsquarewave**, below. The positive and negative displacments in nm (from positive and negative drag velocities) are determined from the square wave fit. The corresponding drag forces (in pN) are calculated for a sphere.

```
centers=centers3;
dydx=abs(centers(3:size(centers),1)-
centers(1:(size(centers,1)-2),1));
space=0;
dydx=cat(1,space,dydx,space);
left=max(centers(:,1));
middle=mean(centers(:,1));
right=min(centers(:,1));
[c,a1]=max(dydx(1:10));
[c,a2]=max(dydx(11:20)); a2=a2+10;
[c,a3]=max(dydx(21:30)); a3=a3+20;
[c,a4]=max(dydx(31:40)); a4=a4+30;
[c,a5]=max(dydx(41:50)); a5=a5+40;
[c,a6]=max(dydx(51:60)); a6=a6+50;
[c,a7]=max(dydx(61:70)); a7=a7+60;
[c,a8]=max(dydx(71:size(centers,1)));
a8=a8+70;
lmr=[left;middle;right;a1;a2;a3;a4;a5;a6;a7;a
    ...8];
[lmr,fval,exitflag]=fminsearch(@dragsquarew
    ...ave, lmr, optimset('TolX',1e-
    ...2,'TolFun',1e-2));
drag(5,1)=(lmr(1)-lmr(2))*pixsize;
drag(6,1)=(lmr(3)-lmr(2))*pixsize;
drag(5,2)=6*pi*eta*radius*400*0.63*10^-6;
drag(6,2)=-drag(5,2);


stiffness=drag(:,2)./drag(:,1);
stiffness(1:6)
disp('mean (pN/nm):')
mean(stiffness(1:6))
```

The center positions from the third movie are fit to a square wave using the subfunction **dragsquarewave**, below. The positive and negative displacments in nm (from positive and negative drag velocities) are determined from the square wave fit. The corresponding drag forces (in pN) are calculated for a sphere.

The trap stiffness is determined from the fitted bead displacments and the drag force at each velocity. Successful calibrations will yield an average stiffness which is close to the individual measurements.

```matlab
function sse=dragsquarewave(lmr)
global centers sqrwave
left=lmr(1);
middle=lmr(2);
right=lmr(3);
a1=lmr(4);
a2=lmr(5);
a3=lmr(6);
a4=lmr(7);
a5=lmr(8);
a6=lmr(9);
a7=lmr(10);
a8=lmr(11);
for i=1:size(centers,1)
   if i>a8
      sqrwave(i,1)=middle;
   elseif i>a7
      sqrwave(i,1)=left;
   elseif i>a6
      sqrwave(i,1)=middle;
   elseif i>a5
      sqrwave(i,1)=right;
   elseif i>a4
      sqrwave(i,1)=middle;
   elseif i>a3
      sqrwave(i,1)=left;
   elseif i>a2
      sqrwave(i,1)=middle;
   elseif i>a1
      sqrwave(i,1)=right;
   else sqrwave(i,1)=middle;
   end
end
sse=sum((centers(:,1)-sqrwave).^2);
edges=lmr(4:11);
if right>middle
   sse=sse^2;
elseif middle>left
   sse=sse^2;
end
if edges==sort(edges,'ascend');
else
   sse=sse^2;
end
```

This subfunction is used to fit a square wave to bead positional data collected during periodic, constant-velocity stage movement.

Appendix A-3: Fitting a Backscatter Image of an Optically Trapped Bead

function centers=imagefitter(frames)

This function is used to fit a Gaussian ring to an image of a bright ring against a dark background. Frames is a 4D array: the first two are the x and y intensity values, the third is the RGB index (all assumed to be equivalent for grayscale, so only the R channel is used), and the fourth is the frame number index.

global frameadjusted circlefit a b xmat ymat num

The global variables are used to pass data between this function and the subfunction used as the fit model (circlefitter, below).

startx0=size(frames,1)/2;
starty0=size(frames,2)/2;
startr0=startx0*0.6;

The Matlab fminsearch function below needs an initial guess for the center and radius of the ring, here assumed to be near the center of the cropped image and with a ring diameter 60% the crop size.

num=0;

The variable num keeps track of how many fit iterations are performed on the most recent image. This can be useful in determining improvements to fitting efficiency.

width=size(frames,2);
height=size(frames,1);
xvec=[1:width];
xmat=xvec;
yvec=[1:height]';
ymat=yvec;
for a=1:width-1
   ymat=cat(2,ymat,yvec);
end
for a=1:height-1
   xmat=cat(1,xmat,xvec);
end

The following section generates two "counting" matrices with dimensions equivalent to the image: one (xmat) counts in the x-direction only (all y-values are the same), while the other (ymat) counts in the y-direction only (all x-values are the same). These are useful in the math used to generate the Gaussian ring in the subfunction fit model below.

```
for k=1:size(frames,4)
   k
   xy=[startx0; starty0; startr0];
   frame=frames(:,:,1,k);
   frameadjusted=double(frame);
   b=mean(min(frameadjusted));
   highest=sort(max(frameadjusted),
      …'descend');
   a=mean(highest(1:20))-b;
   [xy,fval,exitflag]=fminsearch(
      …@circlefitter,xy, optimset('TolX',1e-
      …8,'TolFun',1e-0));
   if exitflag==1
      centers(k,:)=xy;
   else
      centers(k,:)=zeros(1,4);
   end
   clear frame background
end
end


function [sse]=circlefitter(xy)
global frameadjusted circlefit a b xmat ymat
      …num
x0=xy(1);
y0=xy(2);
r0=xy(3);
rmat=((xmat-x0).^2+(ymat-y0).^2).^0.5;
circlefit=a*exp(-(r-r0).^2/4)+b;
% gauss=(a*.75)*exp(-(xmat-x0).^2/(32)-
      …(ymat-y0).^2/(32));
% circlefit=gauss+circlefit;
sse=sum(sum((circlefit-frameadjusted).^2));
num=num+1;
end
```

A loop is used to fit each individual frame from the whole movie in turn. The fit parameters are collected into the single vector xy which needs to be reinitialized to the guess values after each frame. The model also requires values for a and b which are fixed to estimates of the brightest and background values, respectively, for each image. Following a successful fit, the center and radius fitted are stored in the variable centers; unsuccessfully fitted parameters are replaced with zeros to enable user distinction upon examination.

This subfunction calculates a model Gaussian ring and compares it to the data image. It first generates the radius matrix rmat (describing the distance of each pixel from the model center (x0,y0). It then uses a simple Gaussian function to determine intensity of a pixel from the proximity of the pixel radius to the model radius. Matrix math is used to speed the calculations (as opposed to nested for loops). Additional code is left commented-out, but would allow the Gaussian ring to be combined with a 2D Gaussian peak for images which include substantially brighter center regions compared to the surrounding background. This often is unnecessary, and will require additional computation time.

Appendix A-4: Periodic Stage Movement and Video Recording

```
function movie=stagevideo(distance, speed,
    …direction, frameinterval)
```

This function is used by the **dragforce** function to record a movie of the optically-trapped bead while simultaneously moving the motorized stage at constant-velocity over a fixed distance, as specified by the variable **speed** (in units of 0.63 um/sec) and **distance** (in units of 0.1 um). The direction of stage motion is specified by the string varible **direction**, while the interval that frames are collected is specified by the scalar variable **frameinterval**.

```
if nargin<4
    frameinterval=1;
end
framenum=round(0.1*distance/(speed*0.63)*
(30/frameinterval)*4+160/frameinterval);
```

The number of frames that needs to be collected is determined from the stage velocity and distance, with an extra buffer to account for the zero-velocity segments.

```
global vid
vid.FrameGrabInterval=frameinterval;
vid.ReturnedColorSpace='grayscale';
vid.LoggingMode='memory';
vid.FramesPerTrigger=framenum;
```

The video input object settings are adjusted.

```
preview(vid)
start(vid)
movestage(-distance, speed, direction);
movestage(distance, speed, direction);
movestage(-distance, speed, direction);
movestage(distance, speed, direction);
wait(vid);
movie=getdata(vid);
close
end
```

The video input device is started, and then the subfunction **movestage** is used to move the stage at the specified **distance**, **speed**, and **direction**. After all the frames are recorded, they are transferred into the 4D variable movie: the first two dimensions describe the (x,y) pixel intensities; the third dimension can distinguish the RGB channels, though here are all equivalent (grayscale); and, the fourth dimension is the frame index.

148

Appendix A-5: Stage Control

```
function f = movestage(dist,speed,xy)

speed=speed*0.00063;
disp('speed (um/sec):')
disp(speed*1000)
```

This function is used by the **stagevideo** function to move the motorized stage at a fixed distance and velocity, as specified by the variables **dist** (in units of 0.1 um) and **speed** (in units of 0.63 um/sec). The direction the stage moves is specified by the string variable **xy** input as either 'x' or 'y'.

```
global s
speedstring=num2str(speed);
setspeedstring=['S x=',speedstring,'
y=',speedstring];
fprintf(s,setspeedstring);fscanf(s);
fprintf(s,'B x=0 y=0'); fscanf(s);
pause(0.5);
```

The global variable **s** is the serial port object generated by the **setupstage** script which communicates with the stage controller. The string variable **setspeedstring** is used to set the stage velocity of an upcoming move. The command is sent via the serial connection with the Matlab function **fprintf**; the acknowledged response is returned (and cleared from memory) with the Matlab function **fscanf**.

```
if xy=='x'
    xystring='R x=';
elseif xy=='y'
    xystring='R y=';
end
diststring=num2str(dist);
movestring=[xystring,diststring];
fprintf(s,movestring);fscanf(s);
fprintf(s,'status');
status=fscanf(s);
while strfind(status, 'B')==2
    fprintf(s,'status')
    status=fscanf(s);
    pause(0.1);
end
```

The string variable **xystring** is used below as part of a command sent over the serial port to the stage, where **R** indicates a movement relative to the stage's current position. The string variable **diststring** is used in combination with **xystring** to generate the string variable **movestring**, which is then sent via the serial port. A **while** loop is used to prevent further code from being run until the stage motion is completed.

Appendix A-6: Real-Time Force and Pressure Measurement

function force=forceimagerpress()

This function is used to continuously collect the backscatter images of an optically trapped bead, fit those images to determine the bead position and, therefore, the force. It also acquires the pressure readings from the analog input device, pairing them with the force measurements as a function of time. The function runs indefinitely; it must be exited manually by the user at the end of an experiment by pressing <ctrl> and <break> simultaneously on the keyboard.

global vid xmat ymat r0 ai zerovoltage Rp Rv
   …force forcebackup

The global variables vid and ai contain the video input and analog input objects generated by the scripts setupvid and setuppress. The global variables xmat, ymat, and r0 are used in fitting the images with the subfunction circlefitter, below. The global variables Rp and Rv are the pipette radius and vesicle radius, respectively, in μm, and are used to calculate the membrane tension from the aspiration pressure. The global variable force is used to store the results of this function, but will overwrite previous measurements which are then lost if not saved by the user. As a minor safeguard, the preceding measurement is saved in forcebackup.

```
vid.ROIPosition=[0,0,640,480];
pixsize=227;
pressvoltconstant=630;
if exist('Rp')==0
    Rp=0;
    Rv=1;
end
if exist('force')
    forcebackup=force;
end
tensionconstant=Rp/(2*(1-Rp/Rv))/1000;
```

The video ROI is reset, and several constants are defined. The pixel size is 227 nm, but will depend on the optics used. The calibration factor for the pressure (as measured as a voltage from the analog input) is given in Pa/V. If the user does not previously define nonzero values for Rp and Rv, they are set to 0 and 1, respectively, to generate a zero membrane tension which will be readily recognized by the user as incorrect.

```
width=60;
height=40;
xvec=[1:width];
xmat=xvec;
yvec=[1:height]';
ymat=yvec;
for a=1:width-1
    ymat=cat(2,ymat,yvec);
end
for a=1:height-1
    xmat=cat(1,xmat,xvec);
end
pause(0.5);
frame=getsnapshot(vid);
[x,y,P]=impixel(frame); close
vid.ROIPosition=[x-width/2,y-
height/2,width,height];
vid.ReturnedColorSpace='grayscale';
vid.LoggingMode='memory';
```

The video ROI is cropped around the bead as enabled by the user selecting the bead center in a single acquired and displayed image. Additional video input properties are set, including the vid.LoggingMode property which, by specifying 'memory', enables faster frame acquisition.

```
vid.FramesPerTrigger=100;
vid.FrameGrabInterval=1;
answer=0;
while answer==0
    disp('Hit any key to start logging')
    pause
    disp('Logging...')
    start(vid);
    pause(vid.FramesPerTrigger/30+1)
    answer=input('Movie ok? 1 if yes, 0 if no.
        …\n');
    frames=getdata(vid);
    framesbackup=frames(:,:,1,1);
end
centerstransfer=imagefitter(frames);
centers=centerstransfer(:,1:2);
centers=centers*pixsize;
trapcenter=mean(centers);
r0=mean(centerstransfer(:,3))
clear centers

global stiffness
xstiffness=mean(stiffness);
ystiffness=xstiffness;
```

The zero-external-force position is determined by acquiring 100 frames of the bead under zero external force (i.e. prior to contact with a vesicle). User interaction begins recording the movie, and is also required to verify the movie quality prior to fitting the movie frames with the subfunction imagefitter, which uses three fit parameters: bead center and radius. The bead positions are averaged to find the zero-external-force position trapcenter, while the radii are averaged for the scalar r0, which is used as a constant in the subfunction circlefitter, below.

The trap stiffness is presumed to have been previously calibrated with the function dragforce and the resulting vector of velocity-specific stiffnesses is here averaged.

```
vid.FramesPerTrigger=1;
global frameadjusted frames
force=zeros(1000,5);
start(vid)
wait(vid)
frames=getdata(vid);
startx0=size(frames,1)/2;
starty0=size(frames,2)/2;
ai.SampleRate=300;
ai.SamplesPerTrigger=round(540000);
vid.FramesPerTrigger=90000;
pause
```

The pressure and video inputs are prepared to run for an inordinately long time, as the data will be collected in an infinite for loop below. The code pauses to wait for user input to begin acquiring and recording data.

```
start(vid)
start(ai)
pause(0.5)
force(1,1)=xstiffness;
force(1,2)=ystiffness;
force(3,1)=stiffness(1);
force(4,1)=stiffness(2);
force(5,1)=stiffness(3);
force(6,1)=stiffness(4);
force(7,1)=stiffness(5);
force(8,1)=stiffness(6);
force(1:6,3)=clock';
tic
for i=100:inf
   pause(.017)
   frames=peekdata(vid,1);
   while size(frames)==[0 0];
      frames=peekdata(vid,1);
   end
   flushdata(vid)
   pvoltage=peekdata(ai,20);
   force(i,3)=round((mean(pvoltage)-
      …zerovoltage)*pressvoltconstant);
   force(i,4)=toc;
   force(i,5)=force(i,3)*tensionconstant;
   xy=[startx0; starty0];
   frameadjusted=double(frames);
   b=mean(min(frameadjusted));
   a=mean(max(frameadjusted))-b;
   [xy,fval,exitflag]=fminsearch(@circlefitter,
      …xy,optimset('TolX',1e-0,'TolFun', 1));
   beadposition=xy(1:2)'*pixsize-trapcenter;
   force(i,1:2)=(-beadposition).*
      …[xstiffness,ystiffness];
   plot(force(i-99:i,4),force(i-99:i,1))
   title([num2str(force(i,3)),' Pa
      …',num2str(roundn(force(i,5))),'mN/m
      …',num2str(round(force(i,1))),'pN'])
   axis([force(i-99,4) force(i,4) -30 100])
end
end
```

The variable force is created with five columns. In general, the first and second columns will contain x-axis and y-axis force measurements (in pN), respectively, the third column will contain pressure measurements (in Pa), the fourth column will contain the relative time each measurement was collected (in seconds), and the fifth column will contain the calculated membrane tension (in mN/m). This is true, however, only for data contained in rows 100 and lower, for reasons of displaying a live plot of recent measurements to the user. In addition, the average stiffness is recorded in force(1,1) and force(1,2), and the time stamp is recorded in force(1:6, 3).

```
function [sse]=circlefitter(xy)
global frameadjusted circlefit a b xmat ymat
    r0
x0=xy(1);
y0=xy(2);
r=((xmat-x0).^2+(ymat-y0).^2).^0.5;
circlefit=a*exp(-(r-r0).^2/4)+b;
% gauss=(a*.75)*exp(-(xmat-x0).^2/(32)-
    ...(ymat-y0).^2/(32));
% circlefit=gauss+circlefit;
sse=sum(sum((circlefit-frameadjusted).^2));
end
```

This subfunction calculates a model Gaussian ring and compares it to the data image. It first generates the radius matrix rmat (describing the distance of each pixel from the model center (x0,y0). It then uses a simple Gaussian function to determine intensity of a pixel from the proximity of the pixel radius to the model radius. Matrix math is used to speed the calculations (as opposed to nested for loops). Additional code is left commented-out, but would allow the Gaussian ring to be combined with a 2D Gaussian peak for images which include substantially brighter center regions compared to the surrounding background. This often is unnecessary, and will require additional computation time.

Appendix B: Annotated Labview Code

Appendix B-1: Pressure Measurements from Analog Acquisition Device MiniLab 1008 (Measurement Computing Company)
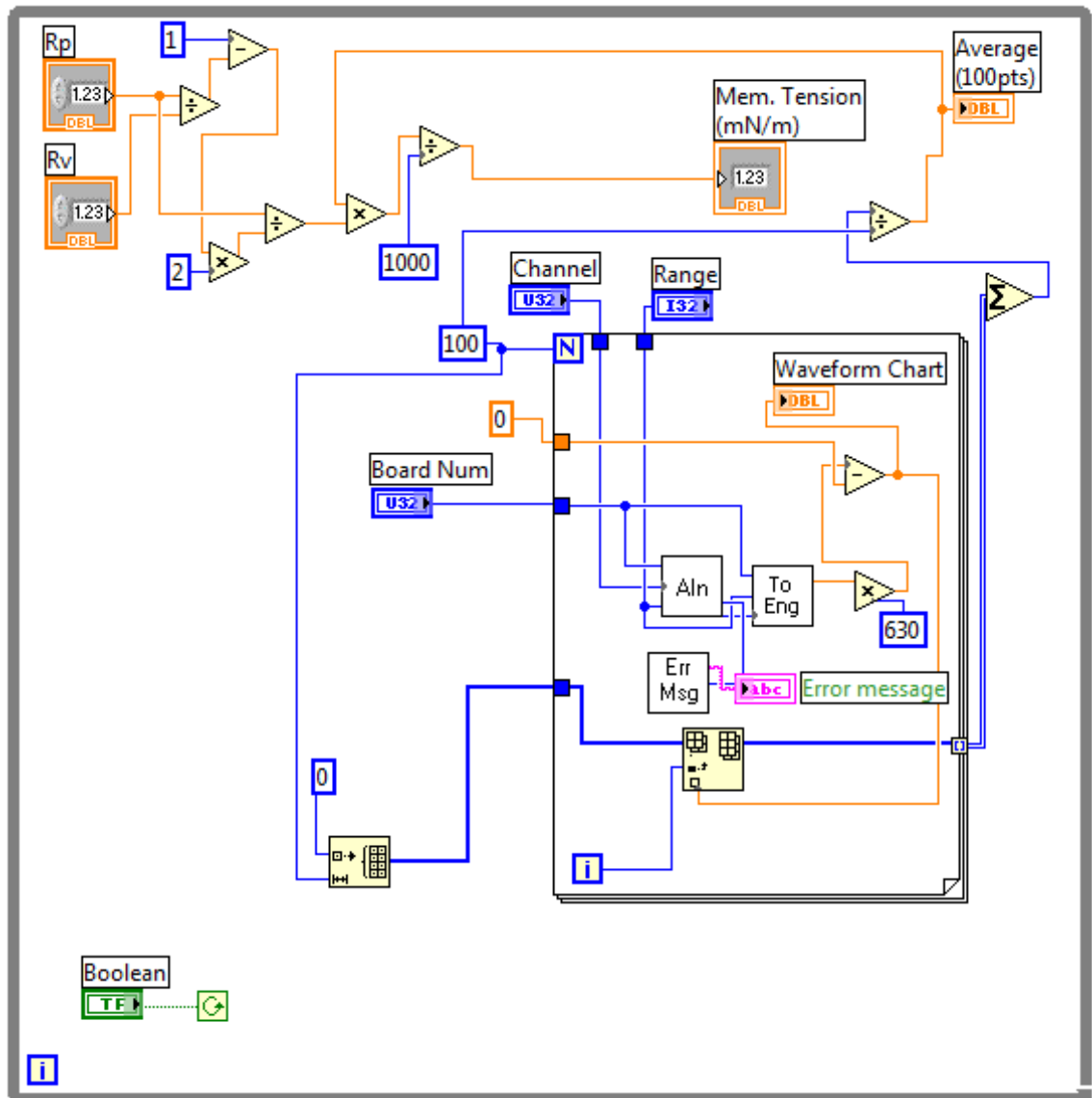
The Labview program "ReadPress.vi" takes measurements of the analog voltage input device from the block AIn, multiplying each by the (previously calibrated) conversion factor 630 Pa/V to convert to pressure units. An offset can also be subtracted from the values to adjust for zero pressure, though this is more typically

accomplished with hardware control. Pressures are displayed in real time to the user in graphical form. In addition, after each cycle of 100 measurements is completed, the pressures are averaged and a corresponding membrane tension is calculated for numerical display to the user. Membrane tension requires user input of the aspirating pipette radius and the vesicle radius in μm; see Equation 3.13.

Appendix B.2: Motorized Stage Control via Serial Connection

The Labview program Stage5.vi communicates via the serial port with the MS2000 XY stage (Applied Scientific Instrumentation). Due to the length of the program, the code is split among several images. Hanging "wires" at the right-hand side of the image connect to those on the left-hand side of the following image.
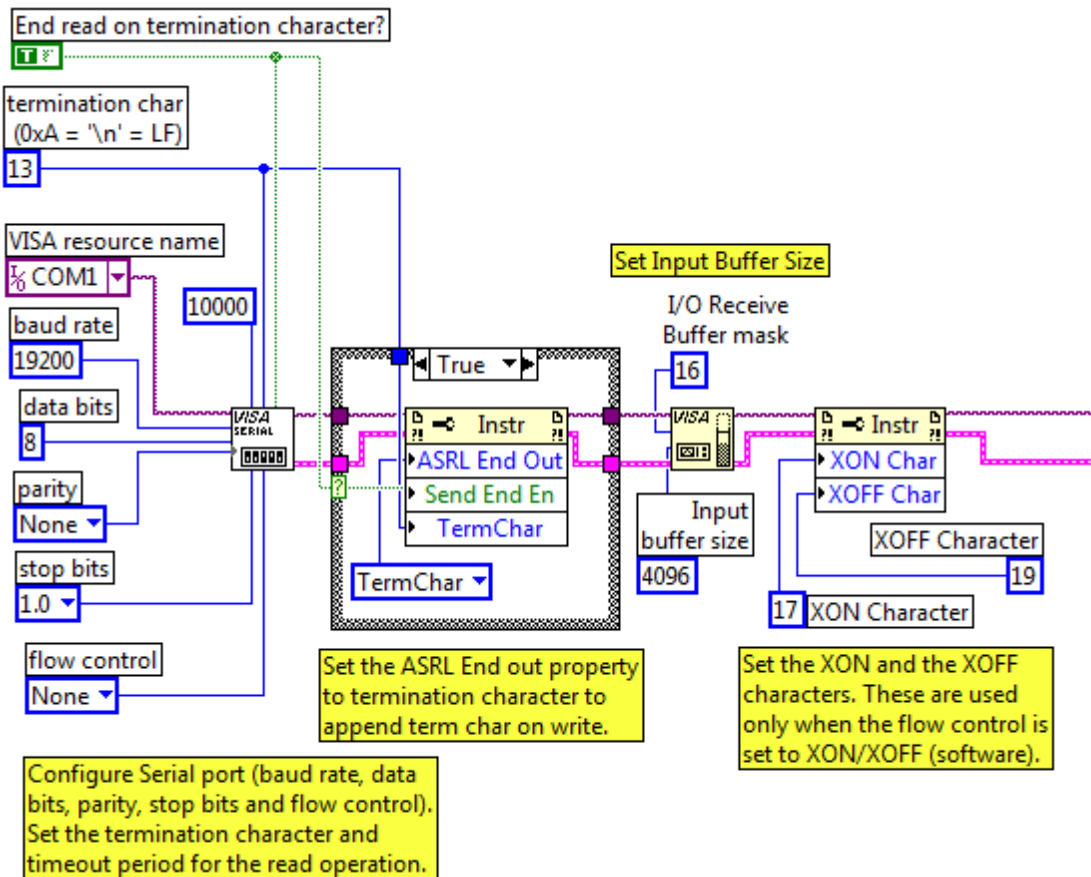
The serial connection is opened with specified settings to enable communication with the stage.
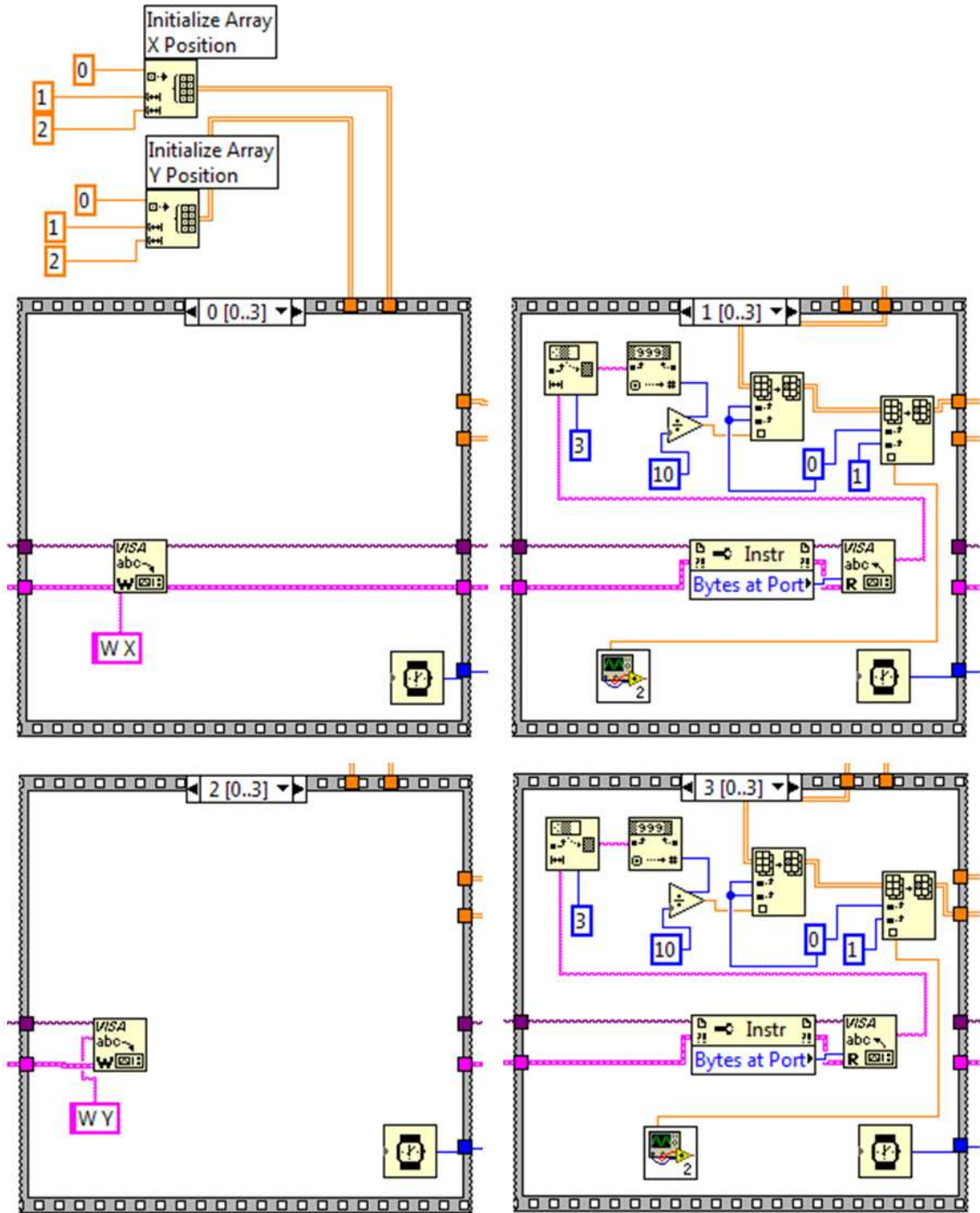
Arrays to contain x and y positional data are created and will be carried

throughout the following code. A stacked sequence structure is used to issue four sets of

commands in order. First, in sequence 0, the command "W X" is sent to the stage to

query the stage's x position. Next, in sequence 1, the reply from the stage is read from the serial port buffer and converted to units of μm. Sequences 2 and 3 perform the same functions for the stage's y position.

The main functionality of the program is contained within the following while loop. On the first iteration (i=0), the x and y positional arrays are carried into the while loop with their initial values (created in the preceding code). During the iteration, these arrays will be expanded to contain the latest positional data (unless the newest value is identical to the preceding one). The resulting arrays are fed back into the beginning of the while loop with each consecutive iteration through the use of shift registers (active for all iterations i>0). Contained with the while loop is a case structure which is only "true" when the user requests a movement by the stage. The "false" case is shown first. Within the case structure is a stacked sequence structure. Sequence 0 issues the command "W X" and sequence 1 receives the reply (the stage's x position). The data is compared to the last value in the x positional array; if it is distinct, the value is appended to the array along with the absolute time (measured in seconds from 12:00:00 am). Otherwise, the array is left unchanged. Sequences 2 and 3 (not shown) perform the same functions for the stage's y position.

160

161
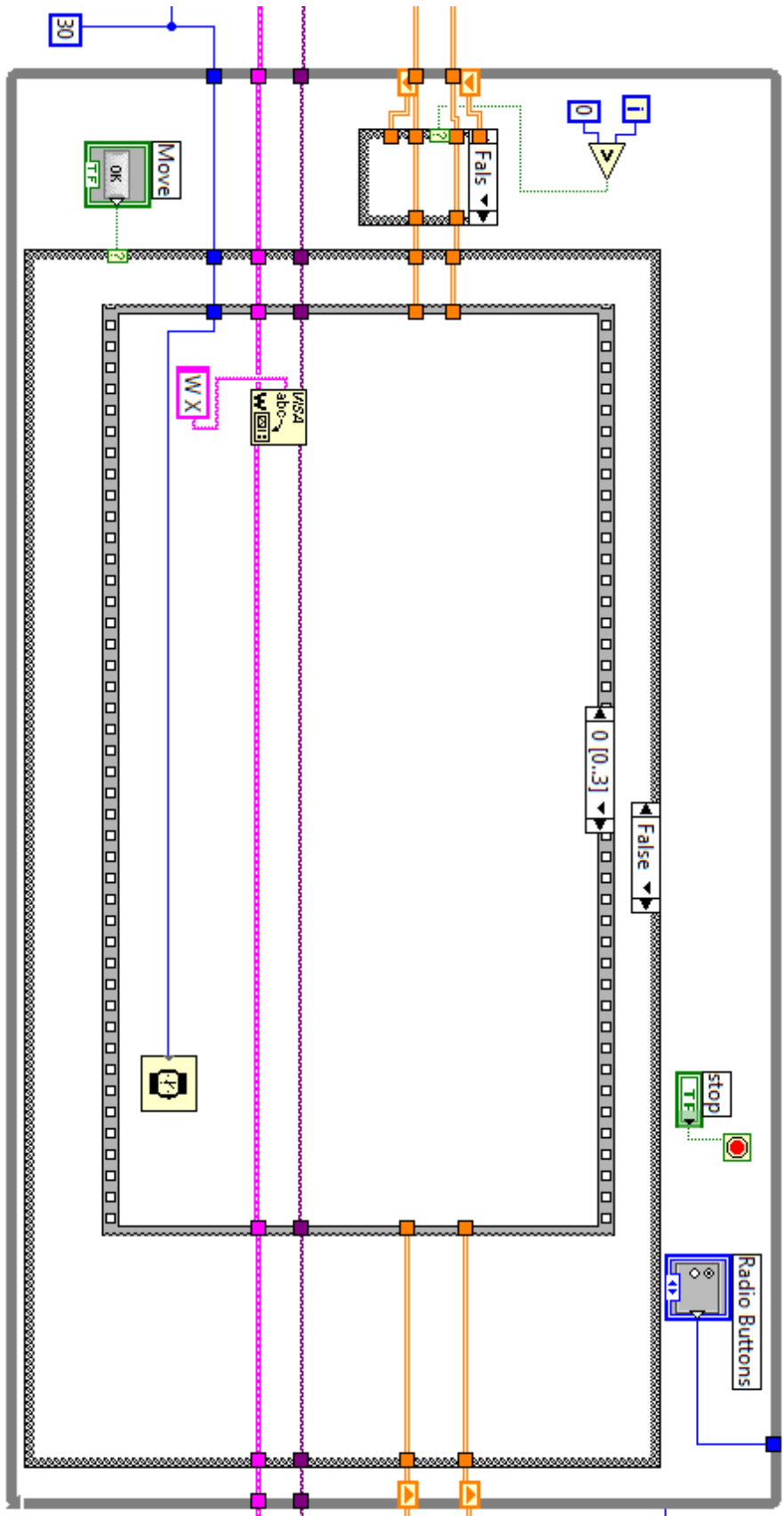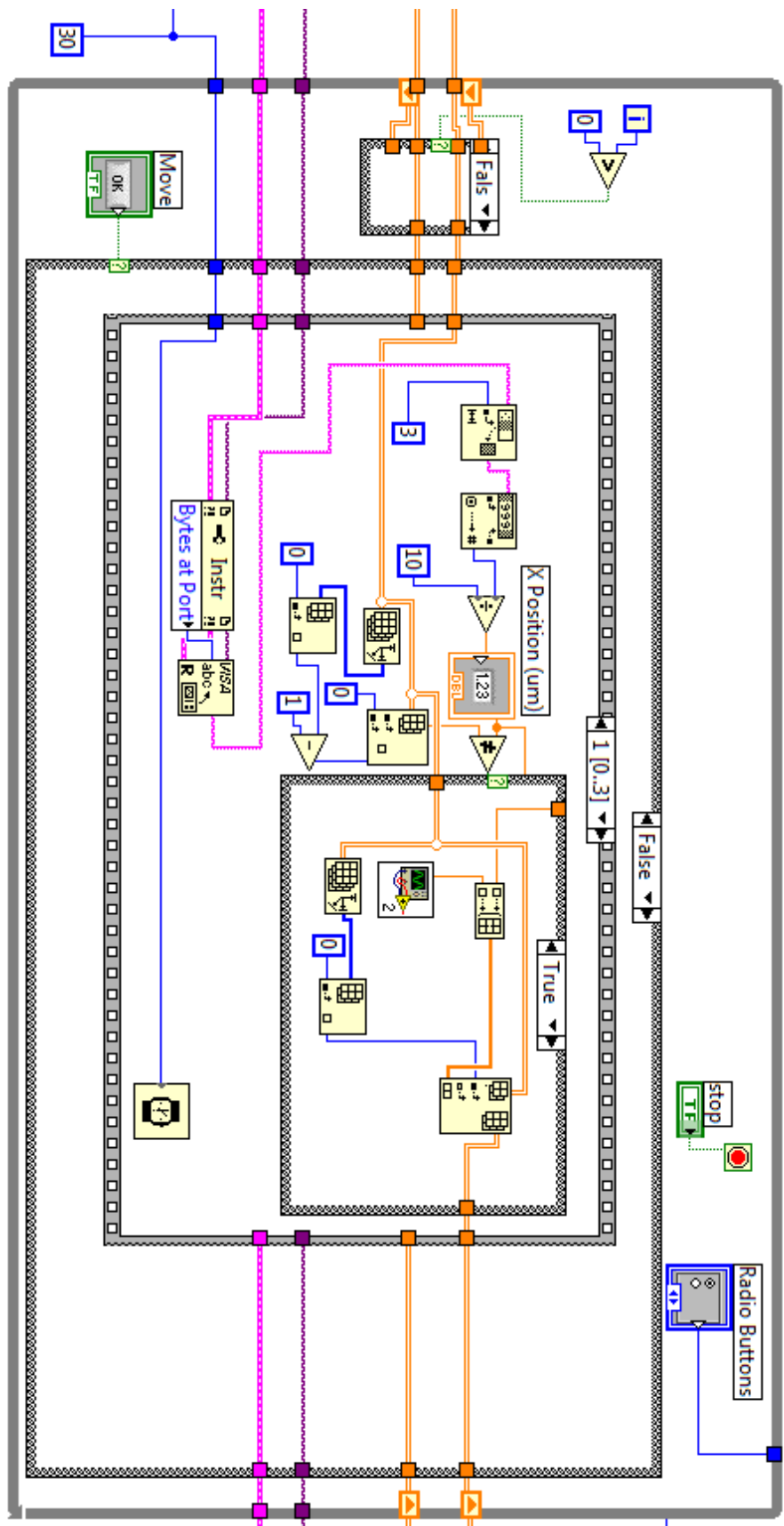
When the user presses a button on the virtual instrument panel to generate a stage movement at a specified velocity and distance, the code contained within the "true" segment of the case structure is executed. Contained within is a stacked sequence structure. Sequence 0 modifies the stage velocity for both x and y movements to match the user-directed velocity, and sequence 1 checks that the setting was changed successfully. Sequence 2 changes the stage backlash setting to zero to achieve a more constant velocity over the length of the movement, and sequence 3 checks the setting was changed successfully. Sequence 4 sends the move command to the stage with the user-specified distance and direction, and sequence 5 checks that the command was received. Sequence 6 is used to block access to the stage while it is busy by utilizing a stacked sequence structure within a while loop. The first sequence queries the status of the stage, and the second compares the response to the anticipated busy signal; the while loop ends when the stage is no longer busy.

163
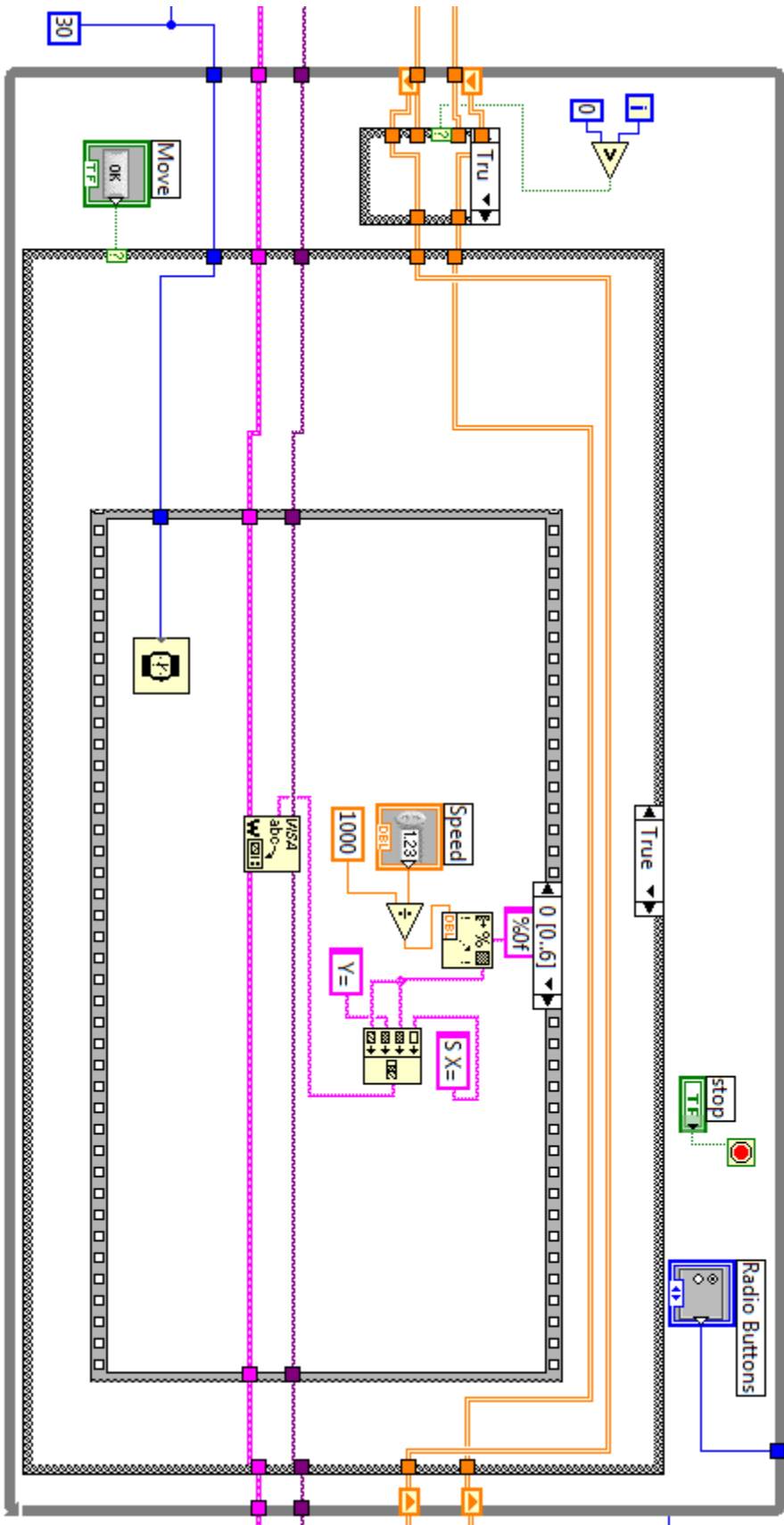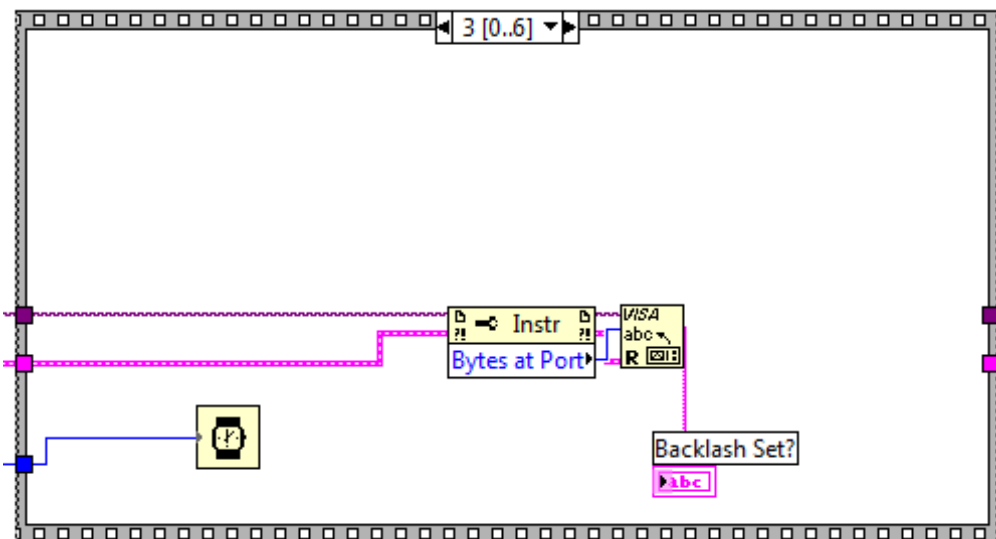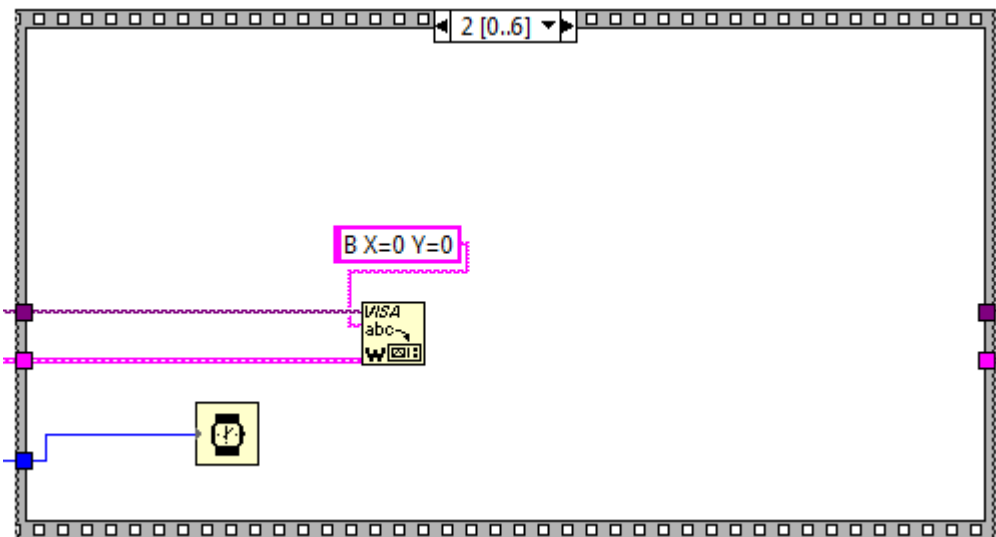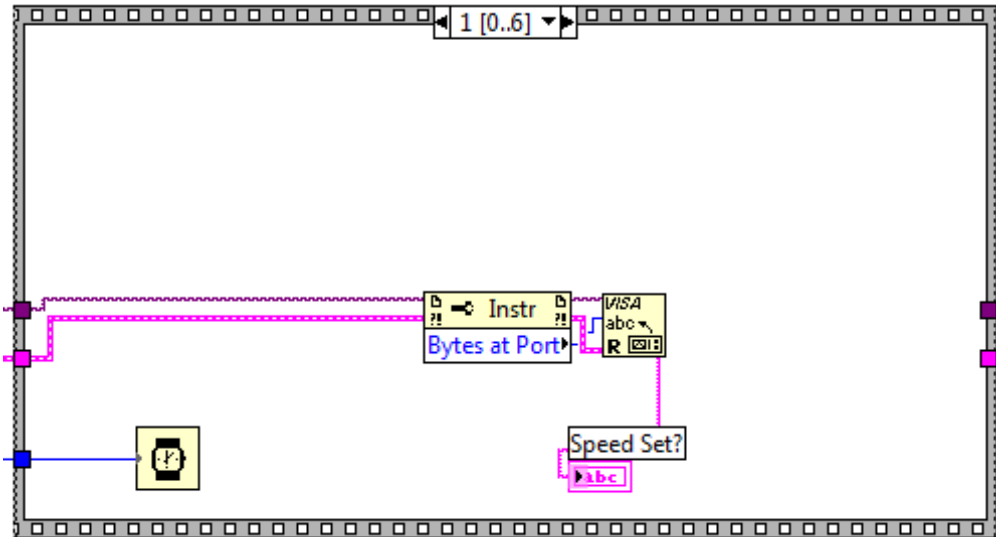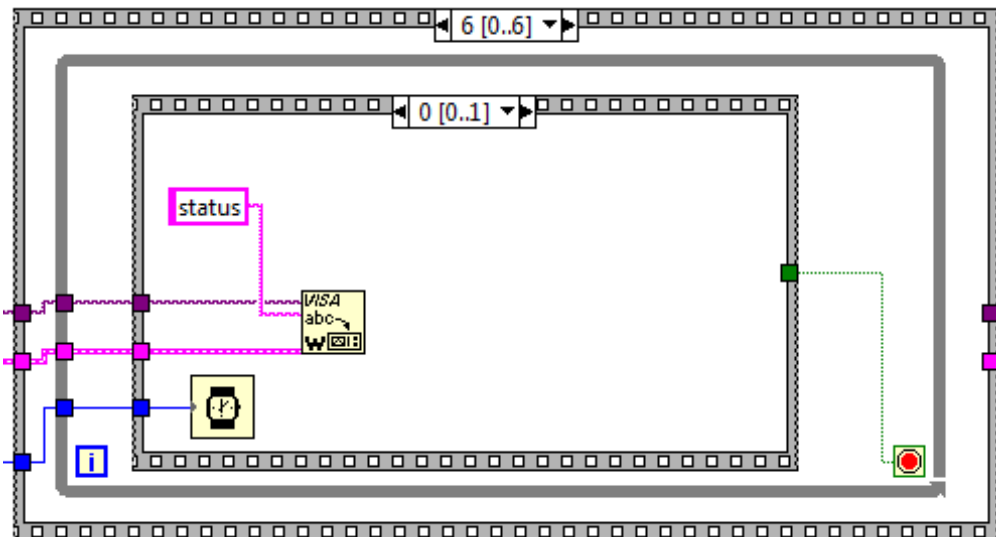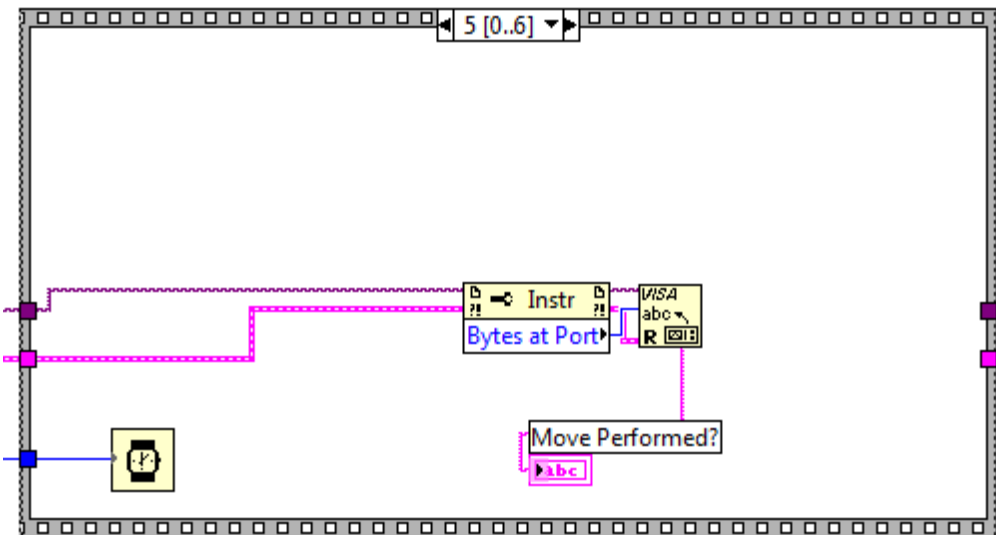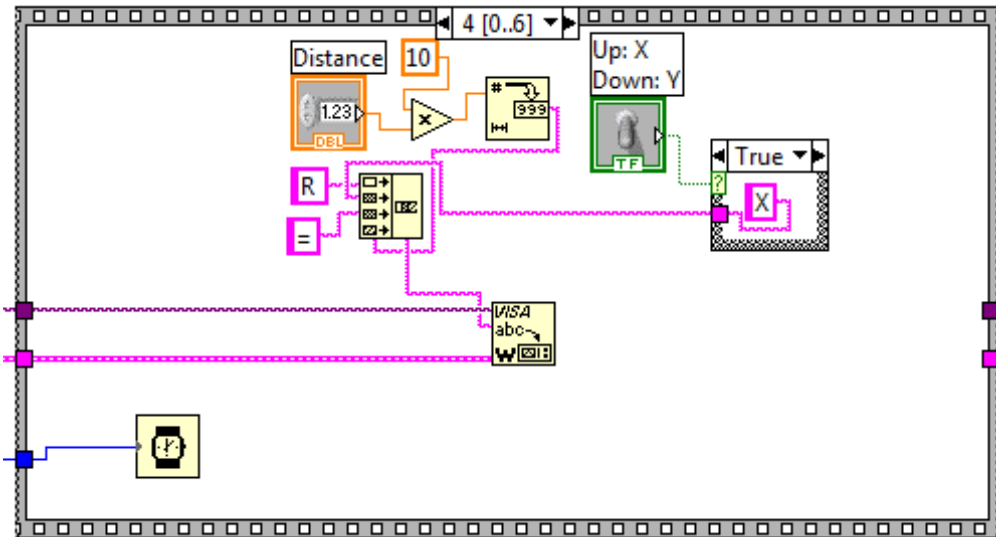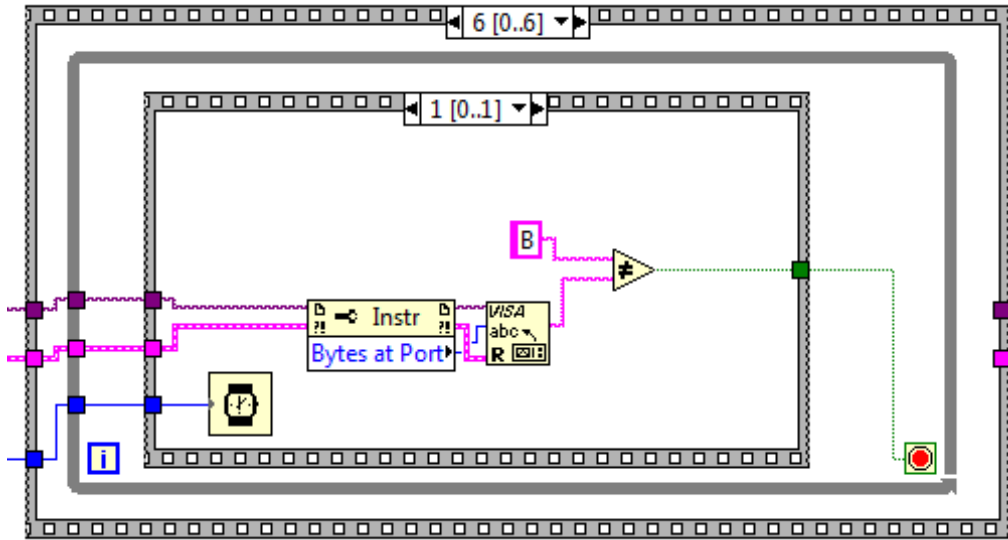
The program runs indefinitely until the user hits a stop button to exit the while loop. After exiting the while loop, the x and y position arrays are displayed and, if the user elects, saved to comma separated value (.csv) files.